The Dissertation Committee for Hariswaran Sitaraman certifies that this is the approved version of the following dissertation:

Magneto-hydrodynamics simulation study of high density thermal plasmas in plasma acceleration devices

Committee:

Laxminarayan L Raja, Supervisor

Philip Varghese

Venkat Raman

David Goldstein

Roger Bengtson

Magneto-hydrodynamics simulation study of high density thermal plasmas in plasma acceleration devices

by

Hariswaran Sitaraman, B.Tech ; M.S.E

Dissertation

Presented to the Faculty of the Graduate School of

The University of Texas at Austin

in Partial Fulfillment

of the Requirements

for the Degree of

Doctor Of Philosophy

The University Of Texas At Austin

August 2013

Dedicated to my parents and my brother...

Acknowledgments

I would like to thank my advisor Dr. Raja who has been a monumental figure in the past five years of my life. I am deeply honoured to be his student and hope that some of his sharpness, intelligence and composure have rubbed off on me. I would also like to thank my committee members Dr. Varghese, Dr. Raman, Dr. Goldstein and Dr. Bengtson for their guidance and suggestions that significantly improved this dissertation.

The past five years of my life at UT would not have been a hobbit's tale without my "academic twin brother", Doug Breden, who pushed me to run faster and bench higher at every moment. I would also like to thank my academic brother Shankar, diligent and hard working, who practically walked me through the initial stages of my PhD. He has always inspired me to become a good coder like him one day. I would like to thank my own brother, Jay Sitaraman, who is a brilliant CFDer, to have made crucial suggestions to make my codes work and run faster and help finish this dissertation. I would also like to thank Dr. Francis Stefani for the numerous discussions we had in the basement lab and also sharpening my resume that determined my future. My sincere gratitude to Prof. Graeme Henkelman for letting me run jobs on the supercomputer "Halifax". I would also like to thank the Air Force Office of Scientific Research (AFOSR) and Dr. Mitat Birkan to have funded my research. I am also grateful to the Texas Advance Computing Center (TACC)

for letting me run my simulations on state of the art supercomputers.

It would have been impossible to have achieved anything without the people who relaxed my mind and supported me at difficult times (such as written and oral qualifiers) . I would like to thank my friends Thomas, Tim, Yeoh, Panda, Sundeep, Utsav, Marshall, Michael, Chris, Frans, Prem and most of all my closest and dearest friend, Archana, for giving me a life outside of academics. I would also like to thank the members of the music band "Dhwani" (Bofi, Anand, Ashwin, Bakri, Shastri, Shruti and Srikanth) for the amazing shows and jamming sessions we had which I will cherish for life. My sincere gratitude to all my friends from IIT Madras who kept visiting me at Austin to bring back the old times.

Last but not the least, I would like to thank my father (who sounds exactly like Prof. Raja) and mother who have been the strength and inspiration to me over the years. I still remember the day after my fluid mechanics qualifiers when I called amma to say that I might have failed it. It was her words and her mental strength that kept me going.

Magneto-hydrodynamics simulation study of high density thermal plasmas in plasma acceleration devices

Hariswaran Sitaraman, Ph.D.
The University of Texas at Austin, 2013

Supervisor: Laxminarayan L Raja

The development of a Magneto-hydrodynamics (MHD) numerical tool to study high density thermal plasmas in plasma acceleration devices is presented. The MHD governing equations represent eight conservation equations for the evolution of density, momentum, energy and induced magnetic fields in a plasma. A matrix-free implicit method is developed to solve these conservation equations within the framework of an unstructured grid finite volume formulation. The analytic form of the convective flux Jacobian is derived for general unstructured grids. A Lower Upper Symmetric Gauss Seidel (LU-SGS) technique is developed as part of the implicit scheme. A coloring based algorithm for parallelization of this technique is also presented and its computational efficiency is compared with a global matrix solve technique that uses the GMRES (Generalized Minimum Residual) algorithm available in the PETSc (Portable Extensible Toolkit for Scientific computation) libraries. The verification cases used for this study are the MHD shock tube problem in one, two and three dimensions, the oblique shock and the Hartmann flow problem. It is seen that the matrix free method is comparatively faster and shows excellent scaling on multiple cores compared to the global matrix solve technique.

The numerical model was thus verified against the above mentioned standard test cases and two application problems were studied. These include the simulation of plasma deflagration phenomenon in a coaxial plasma accelerator and a novel high speed flow control device called the Rail Plasma Actuator (RailPAc).

Experimental studies on coaxial plasma accelerators have revealed two different modes of operation based on the delay between gas loading and discharge ignition. Longer delays lead to the detonation or the snowplow mode while shorter delays lead to the relatively efficient stationary or deflagration mode. One of the theories that explain the two different modes is based on plasma resistivity. A numerical modeling study is presented here in the context of a coaxial plasma accelerator and the effect of plasma resistivity is dealt with in detail. The simulated results pertaining to axial distribution of radial currents are compared with experimental measurements which show good agreement with each other. The simulations show that magnetic field diffusion is dominant at lower conductivities which tend to form a stationary region of high current density close to the inlet end of the device. Higher conductivities led to the formation of propagating current sheet like features due to greater convection of magnetic field. This study also validates the theory behind the two modes of operation based on plasma resistivity.

The RailPAc (Rail Plasma Actuator) is a novel flow control device that uses the magnetic Lorentz forces for fluid flow actuation at atmospheric pressures. Experimental studies reveal actuation $\sim$ 10-100 m/s can be achieved with this device which is much larger than conventional electro-hydrodynamic

(EHD) force based plasma actuators. A magneto-hydrodynamics simulation study of this device is presented. The model is further developed to incorporate applied electric and magnetic fields seen in this device. The snowplow model which is typically used for studying pulsed plasma thrusters is used to predict the arc velocities which agrees well with experimental measurements. Two dimensional simulations were performed to study the effect of Lorentz forcing and heating effects on fluid flow actuation. Actuation on the order of 100 m/s is attained at the head of the current sheet due to the effect of Lorentz forcing alone. The inclusion of heating effects led to isotropic blast wave like actuation which is detrimental to the performance of RailPAc. This study also revealed the deficiencies of a single fluid model and a more accurate multi-fluid approach is proposed for future work.

Table of Contents

List of Tables

List of Figures

Chapter 1

Introduction

Plasma state is often referred to as the fourth state of matter and constitutes more than 99% of the visible universe. They can be classified into two different types - thermal and non-thermal plasmas. Thermal plasmas are characterized by a single temperature for all the species present including electrons, and are generally in a state of Local Thermodynamic Equilibrium (LTE). On the other hand, non-thermal or "cold" plasmas exhibit a large disparity in species temperatures. Typically the electrons are at temperatures $\sim$ 1-10 eV while the heavy species (ions, neutrals and excited species) are close to room temperature $\sim$ 0.025 eV. Discharges at lower pressures (0.1-100 Pa) tend to be non-thermal in nature, whereas at pressures $\sim$ 1 kPa the plasma becomes highly collisional. The much lower energy transfer mean free paths at higher pressures, lead to equalization of temperature among the heavy species and electrons and subsequent thermalization of the plasma. This phenomenon can be easily seen from figure 1.1 which plots electron and heavy species temperatures for varying pressures. Non-thermal plasmas are typically used in low power applications such as lamps [5], ozone generators [6] and semiconductor fabrication devices [7] while thermal plasmas are employed in high power applications such as nuclear fusion [8, 9] and electric propulsion

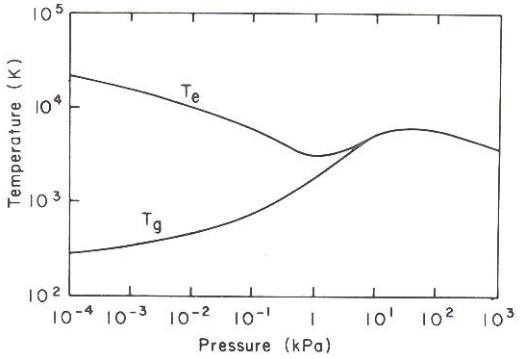

Figure 1.1: Variation of electron and heavy species temperature in a plasma with varying thermodynamic pressures [1]

[10–12] devices.

The physics of thermal plasmas can be aptly described by the resistive magneto-hydrodynamics (MHD) equations. These equations can be derived assuming the plasma is a single quasi-neutral electrically conducting fluid characterized by a single temperature based on the LTE assumption. It is also assumed that the bulk fluid motion time scales are much larger compared to collisional and plasma oscillation time scales (inverse of plasma frequency). This assumption leads to an important result in MHD - the magnitude of displacement currents are much smaller than conduction currents. In essence, these equations reduce to the compressible Navier-Stokes equations for the evolution of the flow field coupled to the Maxwell's equations for electromagnetics. The two different sets of equations are tightly coupled. The fluid momentum equation involves the $\vec{J} \times \vec{B}$ momentum forcing term ($\vec{J}$ is the current density and $\vec{B}$ is the magnetic field) while the energy equation contains volumetric source terms resulting from electric fields (Ohmic heating). The

terms involving current density in the Maxwell's equations also depend on the fluid parameters through a modified Ohm's law. Further details regarding the derivation of these equations are described in chapter 2. The numerical solution to the MHD equations have been used to understand fusion plasmas [13], astrophysical plasmas [14] and high temperature thermal plasmas in electric propulsion devices [15].

1.1 Literature review

A brief review of thermal plasma analysis using magnetohydrodynamics equations and the numerical techniques used to solve them are presented in this section.

1.1.1 MHD models of thermal plasmas

The use of magneto-hydrodynamic effects has been proposed for several flow control applications in the realm of hypersonic aerodynamics, shock boundary layer interaction and boundary layer separation control. The application of electromagnetic effects in hypersonic aerodynamics was first proposed by Resler and Sears [16] in the late 1950s. The motivation for this effort was to control shock stand off distance and heat transfer rates in hypersonic flows typically observed in atmospheric re-entry flows. The strong bow shock at high Mach number regimes in these situations results in the excitation of internal energy modes, dissociation and subsequent ionization of the gas. The conductivity of the ionized gas is observed to be on the order of 100 S/m which can be controlled by the application of external magnetic fields. An

in-depth understanding of the underlying physics in this problem requires the treatment of the strong coupling between the high speed fluid dynamics, electromagnetics and chemistry which becomes extremely complicated. Shang et al. [17, 18] performed numerical studies on hypersonic blunt body flow control using applied magnetic fields. An ideal MHD model was used in these simulations where the electrical conductivity of the plasma is assumed to be infinite resulting in the simplification of the MHD governing equations. For this idealization, the induced magnetic field is only convected by the fluid flow and the diffusive effects due to finite conductivity are assumed to be zero. The simulations revealed an increase in the shock stand off distance for a Mach 16 flow over a hemispherical body, which has been confirmed by experiments [19].

Recently, magneto-hydrodynamic flow actuators have been shown to be effective in the control of shock boundary layer interaction and boundary layer separation control [20–25]. These discharges, also referred to as "snowplow" surface discharges or gliding arcs, are characterized by a plasma column ignited between parallel rail electrodes that propagates in the stream-wise direction by virtue of magnetic Lorentz forces, thereby transferring momentum to the bulk fluid flow. Numerical modeling of such devices have been performed using the full Navier-Stokes equations including turbulence models with energy and momentum source terms that depend on the electromagnetics [24]. These source terms are obtained by describing the plasma parameters through phenomenological models. Macheret et al. [23] also developed an analytical model for the moving plasma column using force balance equations for ions and electrons perpendicular and along the plasma column.

Electric propulsion devices such as pulsed plasma thrusters (PPT)[26], Magneto plasmadynamic thruster (MPDT) [10] and Hall thrusters [11] use the magnetic Lorentz force to accelerate charged particles in a plasma to very high velocities, unattainable by conventional chemical propulsion devices. These devices such as pulsed plasma thrusters commonly operate in a so called snowplow mode where the discharge is confined to a luminous region in the form of a current sheet that propagates from the upstream to the downstream end of the device by the action of Lorentz forces. Analytical models such as the mass-slug and the snowplow model have been developed to study the motion of the moving front [27]. Both these models are essentially force balance equations for the moving current sheet. The mass-slug model treats the current sheet like an impermeable piston while the snowplow model assumes it to be a porous piston that entrains neutral gas in front of it thus accounting for the drag caused by mass increase. Thermal plasmas in such devices have also been studied using the resistive MHD equations which includes diffusive effects due to plasma conductivity, unlike ideal MHD. Sankaran et al. [15] developed a resistive MHD model to simulate the plasma in an MPD thruster. Parameters such as axial velocity and current densities were validated against experimental data. MHD simulation tools such as MACH (Multi-grid Arbitrary Computational Hydromagnetic) code [28–30] have also been used to study electric propulsion devices such as MPD thrusters [31] and magnetic nozzle flows [32]. Cassibry et al. [33, 34] studied the current sheet dynamics in coaxial plasma thrusters using the MACH code and found qualitative agreement with experimental measurements regarding current sheet distribution and magnetic field

strengths.

Thermal plasmas in plasma torches have been employed in several applications that include metal welding and cutting, plasma spraying, waste treatment as well as in the synthesis of fine particles [1, 35]. These devices typically operate at atmospheric pressures in the power range of 10 to 100 kW. The arc plasma tends to be in a state of near LTE conditions with temperatures $\sim$ 1 eV in the bulk, but non-equilibrium effects dominate in the regions close to the bounding surfaces where thermal conduction losses are high. Numerical modeling of such devices is challenging due to several effects that include chemical non-equilibrium effects, electromagnetics, radiation and turbulent fluid flow. Thermal plasmas in plasma torches have been studied using the incompressible Navier-Stokes equations with Lorentz forcing ($\vec{J} \times \vec{B}$) and Joule heating source terms [36–39]. The incompressible flow assumption is valid in these situations because of high acoustic speeds at typical operating temperatures which in turn leads to a low Mach number flow. For instance, Trelles et al. [38] studied direct current (DC) arc plasma torches using the source term based approach with a magnetic vector potential formulation for the Maxwell's equations. Qualitative agreement with experiments with regard to arc reattachment process was obtained but a non-equilibrium model is necessary for capturing the arc dynamics accurately.

Plasmas in high energy applications such as nuclear fusion devices like tokomaks [40], spheromaks [41] and Dense Plasma Focus (DPF) devices [42–44] have been successfully simulated using the resistive MHD equations. Local thermodynamic equilibrium assumption may not be valid here, but the use of

ideal MHD equations can give valuable insights about several instabilities in these devices. Non-linear MHD effects such as formation of magnetic islands and magnetic reconnection can lead to cross field transport and instabilities that diminish the performance of these devices. The NIMROD (Non-ideal Magnetohydrodynamics with Rotation - Open Discussion) code developed by Glasser et al. [13] has been used to simulate the instabilities that arise in the poloidal plane of the tokomak using a two fluid resistive MHD model. Stepneiwski et al. [43] used a resistive MHD model based on momentum and energy source terms to simulate the discharge in a DPF device. There was qualitative agreement with respect to the pinching effects at the exit, observed in experiments.

Astrophysical phenomenon such as solar wind interaction with the earth's magnetosphere [45], accretion disks [46] and astrophysical jets [47] have been simulated using the MHD governing equations. Watanabe et al. [45] studied interaction of solar wind with the earth's magnetic field using three dimensional ideal MHD simulations. The MHD model used was able to capture the magnetosphere formation and magneto-hydrodynamic bow shock on the solar side of the earth. Toth et al. [48] have developed a high performance space weather modeling tool for predicting solar wind interactions which are critical for satellite communications and successful spacecraft missions. Ideal MHD is a reasonable simplification in astrophysical problems due to extremely large length scales resulting in magnetic convection dominated flows as opposed to resistive diffusion. The large magnetic Reynolds numbers can also lead to MHD turbulence [49], much like turbulent phenomenon in flu-

ids, due to large flow Reynolds numbers. MHD turbulence has been simulated through techniques such as Large Eddy Simulations (LES) [50] and spectral methods [51] much like strategies used in turbulent fluid flow simulations [52]. High energy phenomenon in astrophysics can lead to extremely high velocities and interactions between electromagnetic and gravitational fields. Relativistic MHD models [53–55] are used to study such phenomenon that occur in supernovae collapse, pulsars and astrophysical jets. ATHENA [56] is an open source astrophysical relativistic MHD code that has been used to study the interstellar medium, star formation, and accretion flow problems. Anisotropic transport in magnetized astrophysical plasmas and magneto-thermal instabilities [57] have been simulated using this code.

1.1.2 Numerical methods for solving MHD equations

Finite volume formulations to solve the MHD equations have been successfully used predominantly on structured grids using explicit methods such as Runge Kutta schemes [45, 58–63]. The explicit schemes are restricted by the fast plasma wave transit time scales which can severely increase computational costs for steady state problems. The time step restrictions are more severe for low conductivity cases such as high pressure arc plasmas at relatively lower temperatures. Magnetic diffusion time scales for low conductivity plasmas are extremely small. In such situations the low magnetic Reynold's number approximation [64] is used where the Lorentz force and Joule heating terms are treated as source terms as opposed to the magnetic pressure based formulation used at high magnetic Reynold's numbers . An implicit treatment

of the hyperbolic and parabolic terms can potentially help in the seamless capture of both high and low Reynold's number physics observed in MHD. Semi-implicit numerical methods have been widely used to solve the compressible Navier-Stokes equations which are essentially a subset of the MHD governing equations. The flux Jacobian for the hyperbolic terms has been analytically derived [65] for unstructured grids which can be used in a linear system solve at each time step. The semi-implicit scheme developed by Jones et al. [66] for the MHD governing equations is similar to implicit methods used for compressible Navier-Stokes equations. This method was formulated for structured grids. Fully implicit techniques have also been implemented in the context of MHD but they tend to become expensive for large three dimensional problems [67–69].

Spatial discretization techniques for calculating hyperbolic fluxes in the context of MHD governing equations are similar to schemes used by the Navier-Stokes community. The schemes are modified to account for the various wave speeds that arise in MHD as opposed to just acoustic speeds in gas dynamics systems. The flux splitting methods such as Advection Upwind Splitting Method (AUSM) [70] and Van Leer splitting [71] techniques commonly used for discretization of inviscid terms in the compressible Navier-Stokes equations require the homogeneity property [72] to be satisfied which is not the case in MHD equations. Therefore, flux difference techniques using approximate Riemann solvers such as modified Roe scheme [4], Lax Friedrich's method [73] and HLL (Harten Lax Van Leer) [74–76] scheme are commonly used for discretization of hyperbolic flux in finite volume MHD simulations. Higher

order methods using Total Variation Diminishing (TVD) schemes [77] have also been formulated and found to give stable and accurate solutions for three dimensional MHD problems predominantly on structured grids.

Satisfying the divergence free constraint for magnetic field ($\vec{\nabla}.\vec{B} = 0$) has been a challenging task in general three dimensional MHD simulations. This constraint is imposed while deriving the MHD equations and is never solved as a separate equation. The numerical discretization errors give rise to finite divergence of magnetic field in the domain creating numerical instabilities and regions with negative pressures [74, 78]. There are several methods used for divergence cleaning in MHD simulations [79–82]. The elliptic divergence cleaning technique [83], similar to projection methods used in incompressible Navier-Stokes equations [84, 85], have been used here. The magnetic field is corrected at the end of every time step by solving a Poisson equation with the divergence of uncorrected field as the source term. Other techniques such as the Powell formulation [80] or the one by Dedner et al. [81] use a hyperbolic divergence cleaning scheme where errors in divergence of magnetic field are convected out of the computational domain at finite wave speeds. For instance, in the Powell formulation, the terms that involve the divergence of magnetic field are not ignored during the derivation of the governing equations and are used as source terms in the finite volume scheme. An algebraic simplification of the governing equations results in a hyperbolic equation for the divergence of magnetic field. Therefore, divergence free boundary conditions will ensure mitigation of errors within the domain.

Finite difference approaches were one of the earliest techniques used

in MHD simulations where higher order methods such as Weighted Non-Oscillatory (WENO) schemes were also formulated [79, 86–88]. The non-conservative nature of these methods can potentially influence truncation errors in divergence free constraint for high speed flows [79]. These methods are prevalent in the study of MHD turbulence using Direct Numerical Simulations (DNS) [89] or Large Eddy Simulations (LES) [90, 91]. Standard schemes, typically used in turbulent hydrodynamic flows, such as second order accurate central schemes on staggered grids or a combination of second and fourth order schemes have been used in simulating MHD turbulence. Accurate methods to ensure conservation are seen to be important for extension of these techniques to electromagnetics equations [92].

Other numerical techniques such as finite element [93, 94] and discontinuous Galerkin methods [95] have also been used to solve the resistive MHD equations. Sovinec et al. [93] developed a higher order finite element method to solve the nonlinear MHD equations using a semi-implicit leapfrog method where electromagnetic field variables are advanced at half-integer time indices. The code was used to simulate tearing mode evolution in a tokomak. Warburton et al. [95] developed a discontinuous Galerkin method for the resistive MHD equations on general three dimensional mixed unstructured grids with explicit time integration. Higher order accuracy was obtained with the use of orthogonal spectral basis on polymorphic domains.

1.2 Objectives

The principal objective of this research is to develop a high fidelity magneto-hydrodynamics simulation tool to study thermal plasmas in plasma acceleration devices. Two such devices will be studied. One of them is the plasma deflagration phenomenon in a coaxial plasma accelerator and the other is a magneto-hydrodynamic flow control device which we refer to as the Rail Plasma Actuator (RailPAc)

1.2.1 Plasma deflagration in coaxial plasma accelerator

Pulsed coaxial plasma accelerators have been employed in several applications such as in space propulsion [12], as a neutron source for nuclear fusion (Dense Plasma Focus [8]) and in materials processing [96]. Experimental studies on co-axial plasma accelerators [2] have revealed two modes of operation based on the delay between gas loading and discharge ignition. It has been observed that larger delay led to the plasma detonation or snowplow mode where a luminous current sheet propagates from the breech to the muzzle. On the other hand, shorter delay times led to a relatively diffuse, plasma deflagration mode where the input gas is continuously processed and accelerated to high velocities. It was also observed that the deflagration mode gave rise to higher particle energies at the muzzle for lower applied voltages. The physics of the discharge as well as the pinching effects at the muzzle pertaining to this mode of operation has remained relatively unexplored. The plasma in the coaxial plasma accelerator falls under the regime of a thermal plasma with a high degree of ionization which can be studied using the resistive MHD equations.

1.2.2 Rail Plasma Actuator

Flow control using plasma actuators have been currently realized using discharge devices such as Dielectric Barrier Discharges (DBD) [97], nanosecond pulsed plasmas [98] and though Direct Current (DC) discharges [99]. These devices have been successfully employed in controlling boundary layer separation in external flows typically over airfoils. One of the main limitations of these devices is the inability to provide effective actuation at high Reynolds numbers due to low induced velocities. These devices are typically non equilibrium weakly ionized plasmas and rely either on the electro-hydrodynamic (EHD) force or thermalization of energetic ions (ion Joule heating) to provide actuation. The EHD force depends on the charge imbalance and electric field which is dominant only in the plasma sheath. The sheaths tend to be a very small region close to the wall and therefore the actuation tends to be restricted to a small volume. Another approach would be to use a highly conducting thermal plasma and rely on the magnetic Lorentz force ($\vec{J} \times \vec{B}$) to deliver the momentum surplus to the bulk flow. This idea has been used in several other applications such as space propulsion devices [12].For instance, in a parallel plate pulsed plasma thruster, a discharge is ignited between two long parallel electrodes which induces an out of plane magnetic field. The $\vec{J} \times \vec{B}$ force thus propels the high density plasma along the length of the electrodes. A flow control device that uses such a concept has been proposed by our research group and is being investigated experimentally. The work reported in this dissertation is a modeling effort that coordinates with this project.

1.3 Contributions

The contributions of this research are as follows:

- Development of a resistive magneto-hydrodynamics model
  - Implementation of stable convective flux schemes based on approximate Riemann solvers from literature.
  - Formulation of a semi-implicit scheme including derivation of an analytic flux Jacobian and implementation of the Lower Upper Symmetric Gauss Seidel (LU-SGS) method to solve the resulting linear system
  - Parallelization of the code using domain decomposition and implementation of a highly scalable grid coloring based algorithm for the LU-SGS technique.
- Development of a model based physical understanding of coaxial plasma accelerator and its deflagration mode of operation
- Simulation study of the proposed novel flow control device (RailPAc) at atmospheric pressure.

Prior to the MHD research work, a previous research project on modeling of microdischarges (during the years 2009-2011) is also described in chapter 8 including:

- One dimensional simulation study of gas temperature effects in micrometer length scale Dielectric Barrier Discharges (DBD). The results have been published in ref. [100].

- Multidimensional simulation study of micro-cavity discharges as a micropropulsion device. The results have been published ref. [101, 102].

Chapter 2

Governing equations

The derivation of the MHD governing equations using the magnetic pressure formulation is presented in this chapter. The electromagnetics and fluid physics equations are combined together to give rise to a coupled set of eight conservation equations.

2.1 Assumptions

The assumptions made while deriving the MHD governing equations are as follows.

- The plasma is assumed to be a single quasi-neutral electrically conducting fluid.
- Local Thermodynamic Equilibrium (LTE) is assumed. The plasma is sufficiently collisional to be characterized by a single temperature for all species.
- The bulk fluid motion time scales are assumed to be much larger than collisional (reciprocal of collision frequency) and plasma oscillation (reciprocal of plasma frequency) time scales.

- The displacement currents are assumed to be much smaller than conduction currents in the plasma due to large characteristic time scales of the plasma flow.

- The modified Ohms law $\vec{J} = \sigma(\vec{E} + \vec{V} \times \vec{B})$ is used here assuming the Hall effect terms are neglected. This can be done if the collision frequencies are much larger than cyclotron frequencies.

- The conducting fluid is assumed to be sufficiently collisional that the transport properties are taken as scalars, i.e. cross B-field and Hall effects are ignored.

2.2 Validity of LTE assumption

The conditions for a steady state, optically thin plasma, to be in a state of LTE are as shown below. These assumptions are enlisted in the text book on thermal plasmas by Boulos et al. [1].

- All the species in the plasma must have a Maxwellian velocity distribution function.

- The heavy species and electrons are in kinetic equilibrium. This implies, the translational temperatures of all the heavy species are equal to the electron temperature.

- Excited state population in different energy levels should have a Boltzmann distribution.

- There is ionization equilibrium where the rate of ionization will equal the rate of recombination reactions.

Sufficient collisionality in the plasma will ensure the above conditions to be true. Specific case of kinetic equilibrium can be analysed as follows. For a typical plasma initiated by an electric discharge, the electrons are accelerated by the electric field. These electrons undergo collisions with the heavy species and transfer energy through elastic collisions. A simple balance of electron Joule heating and elastic collision loss (Eq. 2.1) can be used to obtain an estimate of the difference between electron and heavy species temperatures.

$$\vec{J_e}.\vec{E} = \frac{3}{2}k_B n_e(T_e - T_g)\frac{2m_e}{m_h}\nu \tag{2.1}$$

Here, J_e represents the electron current density and $\vec{E}$ is the electric field. The right hand side of Eq. 2.1 represents the energy gained by the heavy species through elastic collisions with electrons. Here T_e is the electron temperature, T_g is the gas temperature, m_e is mass of an electron, m_h is the mass of a heavy species atom, ν is the electron heavy species collision frequency and n_e is the electron number density. The electron current density, J_e, can be written in terms of mobility μ_e as shown in Eq. 2.2.

$$\vec{J_e} = -e\mu_e n_e \vec{E} = \frac{e^2 n_e}{m_e \nu}\vec{E} \tag{2.2}$$

An expression for the difference between the electron and heavy species temperature can be obtained by substituting the above in Eq. 2.1. This is given in Eq. 2.3.

$$\frac{T_e - T_g}{T_e} = \frac{\pi m_h}{24 m_e} \left(\frac{eE\lambda}{k_B T_e} \right)^2 \tag{2.3}$$

Here, λ is the mean free path associated with electron heavy species collisions given by Eq. 2.4. $\bar{v_e}$ represents the average thermal speed of electrons.

$$\lambda = \frac{\bar{v_e}}{\nu}$$

$$\bar{v_e} = \sqrt{\frac{8 k_B T_e}{\pi m_e}} \tag{2.4}$$

From Eq. 2.3, it is seen that the difference in the electron and heavy species temperature depends directly on the product of the electric field and mean free path. The mean free path varies as the reciprocal of thermodynamic pressure and hence the ratio of electric field to pressure ($\frac{E}{p}$) becomes an important parameter that determines kinetic equilibrium. Substituting typical values for a high-intensity argon arc plasma [103] ($E = 1700\ V/m$, $\lambda = 1\ \mu m$, $m_h/m_e = 7 \times 10^4$ and $T_e = 2\ eV$), the LHS of Eq. 2.3 works out to be about 0.6 %.

Serious deviations from LTE is seen close to the bounding walls and electrodes of a thermal plasma where the heat loss through thermal conduction and radiation is high. These fringe regions near the surface have thickness on the order of thermal diffusion length scale. The LTE assumption tends to be a good engineering approximation, if the size of the bulk plasma is large

compared to the fringe regions and helps in the simplification of the governing equations.

2.3 Governing equations

The resistive magneto-hydrodynamics equations can be written out as the compressible Navier-Stokes equations with magnetic Lorentz force and Joule heating source terms in the momentum and energy equations respectively. This is shown in Eqs. 2.5, 2.6 and 2.7. These equations can be derived by adding up the mass, momentum and energy conservation equations for each individual species in the plasma. The detailed derivation from first principles is given in ref. [104].

$$\frac{\partial \rho}{\partial t} + \vec{\nabla}.(\rho \vec{V}) = 0 \tag{2.5}$$

$$\frac{\partial \rho \vec{V}}{\partial t} + \vec{\nabla}.(\rho \vec{V}\vec{V}) = -\vec{\nabla} P + (\vec{J} \times \vec{B}) + \vec{\nabla}.\bar{\bar{\tau}} \tag{2.6}$$

$$\begin{aligned} &\frac{\partial (\rho E_t)}{\partial t} + \vec{\nabla}.\left[(\rho E + P)\, \vec{V} \right] = \\ &\quad \vec{J}.\vec{E} + \vec{\nabla}.(k \vec{\nabla} T) + \vec{\nabla}.(\bar{\bar{\tau}}.\vec{V}) \end{aligned} \tag{2.7}$$

Here $\rho, \vec{V}, \vec{B}, \vec{E}, \vec{J},$ and P represent the variables for density, velocity, magnetic field, electric field, electrical current density and thermodynamic pressure respectively. $\rho, \rho\vec{V},$ and ρE_t represent the conservative variables for mass, momentum and energy per unit volume. $\bar{\bar{\tau}}$ represents the viscous stress tensor and k is the thermal conductivity. The total energy per unit volume

can be written in terms of the thermodynamic pressure and kinetic energy as shown in Eq. 2.8.

$$\rho E_t = \frac{P}{\gamma - 1} + \frac{1}{2}\rho |V|^2 \tag{2.8}$$

The viscous stress tensor $\bar{\bar{\tau}}$ is as shown in Eq. 2.9 where μ represents the coefficient of viscosity and $u_i \, (i = 1 \; to \; 3)$ represent the three components of velocity.

$$\tau_{ij} = \mu \left(\frac{\partial u_i}{\partial x_j} + \frac{\partial u_j}{\partial x_i} \right) - \frac{2\mu}{3} \frac{\partial u_k}{\partial x_k} \delta_{ij} \tag{2.9}$$

In order to obtain the electromagnetic parameters in the above equations, one needs to use the Faraday's and Ampere's law from the Maxwell's equations as shown in Eq. 2.10 and 2.11.

$$\vec{\nabla} \times \vec{E} = -\frac{\partial \vec{B}}{\partial t} \tag{2.10}$$

$$\vec{\nabla} \times \vec{B} = \mu_0 \vec{J} \tag{2.11}$$

The displacement current term is ignored in Eq. 2.11 as per the MHD approximation. The equations are closed by the modified Ohm's law which can be derived from the sum of all the species momentum equations multiplied by their respective charges, as shown in Eq. 2.12.

$$\vec{J} = \sigma \left(\vec{E} + \vec{V} \times \vec{B} \right) \tag{2.12}$$

Here, σ is the electrical conductivity and μ_0 is the magnetic permeability of free space. The bulk fluid velocity appears in the Ohm's law thereby coupling the fluid mechanics with the electromagnetics equations.

These equations can be further simplified by substituting for $\vec{J}$ from Ampere's law (Eq. 2.11) into the momentum source term and the electric field from Ohm's law (Eq. 2.12) into the energy source term.

The momentum source term can be simplified using vector identities and the divergence free constraint on magnetic field ($\vec{\nabla}.\vec{B} = 0$) as shown below in Eq. 2.13.

$$\vec{J} \times \vec{B} = \left(\frac{\vec{\nabla} \times \vec{B}}{\mu_0} \right) \times \vec{B}$$

$$\vec{B} \times (\vec{\nabla} \times \vec{B}) = \vec{\nabla} \left(\frac{B^2}{2} \right) - (\vec{B}.\vec{\nabla})\vec{B}$$

$$(\vec{B}.\vec{\nabla})\vec{B} = \vec{\nabla}.(\vec{B}\vec{B}) - (\vec{\nabla}.\vec{B})\vec{B} = \vec{\nabla}.(\vec{B}\vec{B})$$

$$\vec{J} \times \vec{B} = -\vec{\nabla} \left(\frac{B^2}{2\mu_0} \right) + \vec{\nabla}. \left(\frac{\vec{B}\vec{B}}{\mu_0} \right) \tag{2.13}$$

The energy source term can be simplified as shown below. The vector identity shown in Eq. 2.14 is also used here.

$$\vec{\nabla}.(\vec{P} \times \vec{Q}) = \vec{Q}.(\vec{\nabla} \times \vec{P}) - \vec{P}.(\vec{\nabla} \times \vec{Q}) \tag{2.14}$$

$$\vec{J}.\vec{E} = \left(\frac{\vec{\nabla} \times \vec{B}}{\mu_0}\right).\vec{E} \tag{2.15}$$

$$\left(\frac{\vec{\nabla} \times \vec{B}}{\mu_0}\right).\vec{E} = \vec{\nabla}.\left(\frac{\vec{B} \times \vec{E}}{\mu_0}\right) + \frac{\vec{B}}{\mu_0}.\left(\vec{\nabla} \times \vec{E}\right) \tag{2.16}$$

The first term in Eq. 2.16 can be simplified by using the modified Ohm's law as shown below.

$$\vec{\nabla}.\left(\frac{\vec{B} \times \vec{E}}{\mu_0}\right) = \vec{\nabla}.\left(\frac{\vec{B}}{\mu_0} \times \left(\frac{\vec{J}}{\sigma} - \vec{U} \times \vec{B}\right)\right)$$

$$\vec{\nabla}.\left(\frac{\vec{B} \times \vec{E}}{\mu_0}\right) = -\vec{\nabla}.\left(\frac{\vec{J} \times \vec{B}}{\mu_0 \sigma}\right) - \vec{\nabla}.\left(\frac{\vec{B}}{\mu_0} \times \left(\vec{U} \times \vec{B}\right)\right) \tag{2.17}$$

$$\vec{\nabla}.\left(\frac{\vec{B} \times \vec{E}}{\mu_0}\right) = -\vec{\nabla}.\left(\frac{\vec{J} \times \vec{B}}{\mu_0 \sigma}\right) - \vec{\nabla}.\left(\frac{|B|^2}{\mu_0}\vec{U} - \frac{\left(\vec{U}.\vec{B}\right)\vec{B}}{\mu_0}\right) \tag{2.18}$$

The second term in Eq. 2.16 can be simplified using Faraday's law to yield the time derivative of magnetic pressure as shown below.

$$\frac{\vec{B}}{\mu_0}.\left(\vec{\nabla} \times \vec{E}\right) = \frac{\vec{B}}{\mu_0}.-\frac{\partial \vec{B}}{\partial t} = -\frac{\partial}{\partial t}\left(\frac{|B|^2}{2\mu_0}\right) \tag{2.19}$$

The Joule heating can be expressed by using the simplified expressions derived in 2.18 and 2.19 as shown in Eq. 2.20.

$$\vec{J}.\vec{E} = -\frac{\partial}{\partial t}\left(\frac{|B|^2}{2\mu_0}\right) - \vec{\nabla}.\left(\frac{|B|^2}{\mu_0}\vec{U} - \frac{\left(\vec{U}.\vec{B}\right)\vec{B}}{\mu_0}\right) - \vec{\nabla}.\left(\frac{\vec{J} \times \vec{B}}{\mu_0 \sigma}\right) \tag{2.20}$$

The last term in Eq. 2.20 can be further simplified using vector identity in Eq. 2.14 to the form shown in Eq. 2.21. This form is also used in the representation of the energy source term in the literature [17, 18] but the divergence form will be used here for ease of simplification into the finite volume method.

$$-\vec{\nabla}.\left(\frac{\vec{J}\times\vec{B}}{\mu_0\sigma}\right)=\frac{|J|^2}{\sigma}-\frac{\vec{B}}{\mu_0}.\vec{\nabla}\times\left(\frac{J}{\sigma}\right) \tag{2.21}$$

A convection-diffusion equation for the evolution of magnetic field can be derived by combining the Faraday's and Ampere's law together. The vector identity $\vec{\nabla}\times(\vec{P}\times\vec{Q})=\vec{\nabla}.(\vec{Q}\vec{P}-\vec{P}\vec{Q})$ is used here in the simplification.

$$\frac{\partial\vec{B}}{\partial t}=-\vec{\nabla}\times\vec{E}$$

$$\vec{\nabla}\times\vec{E}=\vec{\nabla}\times\left(\frac{\vec{J}}{\sigma}-\vec{V}\times\vec{B}\right)$$

$$\frac{\partial\vec{B}}{\partial t}=\vec{\nabla}\times(\vec{V}\times\vec{B})-\vec{\nabla}\times\left(\frac{\vec{J}}{\sigma}\right)$$

$$\frac{\partial\vec{B}}{\partial t}=\vec{\nabla}.(\vec{B}\vec{V}-\vec{V}\vec{B})-\vec{\nabla}\times\left(\frac{\vec{\nabla}\times\vec{B}}{\mu_0\sigma}\right)$$

$$-\vec{\nabla}\times\left(\frac{\vec{\nabla}\times\vec{B}}{\mu_0\sigma}\right)=\frac{1}{\mu_0\sigma}\nabla^2\vec{B}+\frac{\vec{\nabla}\sigma\times\vec{J}}{\sigma^2} \tag{2.22}$$

The resistive MHD equations then reduce to 8 conservation equations for mass, three momentas, three components of magnetic field and energy as shown in Eq. 2.23, 2.24, 2.25 and 2.26 [17].

$$\frac{\partial \rho}{\partial t} + \vec{\nabla}.(\rho \vec{V}) = 0 \tag{2.23}$$

$$\frac{\partial \rho \vec{V}}{\partial t} + \vec{\nabla}.(\rho \vec{V}\vec{V} - \vec{B}\vec{B}) = -\vec{\nabla}\left(P + \frac{|B|^2}{2\mu_0}\right) + \vec{\nabla}.\bar{\bar{\tau}} \tag{2.24}$$

$$\frac{\partial \vec{B}}{\partial t} + \vec{\nabla}.(\vec{V}\vec{B} - \vec{B}\vec{V}) = -\vec{\nabla} \times \left(\frac{\vec{\nabla} \times \vec{B}}{\mu_0 \sigma}\right) \tag{2.25}$$

$$\begin{aligned} \frac{\partial \rho Z}{\partial t} + \vec{\nabla}.\left[\left(\rho Z + P + \frac{|B|^2}{2\mu_0}\right)\vec{V} - \frac{\vec{V}.\vec{B}}{\mu_0}\vec{B}\right] = \\ \vec{\nabla}.\left(k\vec{\nabla}T\right) + \vec{\nabla}.\left(\bar{\bar{\tau}}.\vec{V}\right) - \frac{1}{\mu_0}\vec{\nabla}.\left(\frac{\vec{J} \times \vec{B}}{\sigma}\right) \end{aligned} \tag{2.26}$$

The modified total energy per unit volume, ρZ, can be written in terms of the thermodynamic pressure, kinetic energy and magnetic pressure as shown in Eq. 2.27.

$$\rho Z = \frac{P}{\gamma - 1} + \frac{1}{2}\rho |V|^2 + \frac{|B|^2}{2\mu_0} \tag{2.27}$$

Chapter 3

Numerical formulation

3.1 Non-dimensionalization of governing equations

The governing equations (Eqs. 2.23-2.26) are recast in non-dimensional form with problem specific scales for length (l_s), density (ρ_s) and velocity (v_s).

Quantity	Scaling
time	$t_s = l_s(v_s)^{-1}$
Thermodynamic pressure	$p_s = \rho_s v_s^2$
Temperature	$T_s = v_s^2(\gamma R)^{-1}$
Magnetic field	$B_s = \sqrt{\mu_0 \rho_s v_s^2}$
Current density	$J_s = B_s(\mu_0 l_s)^{-1}$
Coefficient of viscosity	$\mu_s = \rho_s v_s l_s$
Thermal conductivity	$k_s = \rho_s v_s l_s \gamma R$
Electrical conductivity	$\sigma_s = (\mu_0 v_s l_s)^{-1}$

Table 3.1: Scaling of variables

The scaling factors for other quantities are given in table 3.1. Note that the scaling assumed for magnetic field eliminates the occurrence of magnetic permeability (μ_0) in the non-dimensional governing equations. The tempera-

ture and thermal conductivity scales depend on the gas constant and the specific heat ratio. Equations from this point on will be in the non-dimensional form unless specified.

3.2 Finite volume formulation

The governing equations are essentially convection-diffusion equations which can be written out in conservation form as shown in Eq. 3.1.

$$\frac{\partial \mathbf{U}}{\partial t} + \vec{\nabla}.\vec{\mathbf{F}}_{inv} = \vec{\nabla}.\vec{\mathbf{F}}_{diff} + \mathbf{S} \tag{3.1}$$

Here $\mathbf{U}$ is a vector of the 8 conservative variables corresponding to mass, momentum, magnetic induction and energy given in Eq. 3.2. $\vec{\mathbf{F}}_{inv}$ is the inviscid flux vector and $\vec{\mathbf{F}}_{diff}$ is the vector of diffusive fluxes as shown in Eqs. 3.3 and 3.4 respectively. $\mathbf{S}$ denotes the volumetric source term which consist of terms that arise due to gradients of plasma resistivity ($\eta = \sigma^{-1}$) and the terms that involve the divergence of magnetic field as shown in Eq. 3.5. The latter is associated with the mitigation of magnetic field divergence in the numerical calculation. In order to satisfy the divergence free constraint for magnetic field in the domain, Powell et al. [80] suggested a technique wherein the divergence terms that arise during the derivation of the MHD equations be retained and treated as source terms. Once this is done, manipulation of the governing equations yields a pure convection equation for the divergence of magnetic field. Therefore, if a divergence free magnetic field is specified at the boundaries, the field in the domain will remain solenoidal. Other divergence

cleaning methods such as by Dedner et al. [81] and Balsara [82] can also be used. The Powell formulation was chosen for this work due to the simplicity of implementation and its direct extension to unstructured grids. The implicit scheme formulated in this work treats the divergence terms explicitly and hence any of the above mentioned divergence cleaning techniques may be used.

$$\mathbf{U} = \begin{bmatrix} \rho \\ \rho u \\ \rho v \\ \rho w \\ B_x \\ B_y \\ B_z \\ \rho Z \end{bmatrix} \tag{3.2}$$

$$\vec{\mathbf{F}}_{inv} = \begin{bmatrix} \rho\vec{V} \\ \rho u\vec{V} + P_t\hat{x} - B_x\vec{B} \\ \rho v\vec{V} + P_t\hat{y} - B_y\vec{B} \\ \rho w\vec{V} + P_t\hat{z} - B_z\vec{B} \\ B_x\vec{V} - u\vec{B} \\ B_y\vec{V} - v\vec{B} \\ B_z\vec{V} - w\vec{B} \\ (\rho Z + P_t)\vec{V} - (\vec{V}.\vec{B})\vec{B} \end{bmatrix} \tag{3.3}$$

$$\vec{\mathbf{F}}_{diff} = \begin{bmatrix} 0 \\ \tau_{11}\hat{x} + \tau_{21}\hat{y} + \tau_{31}\hat{z} \\ \tau_{12}\hat{x} + \tau_{22}\hat{y} + \tau_{32}\hat{z} \\ \tau_{13}\hat{x} + \tau_{23}\hat{y} + \tau_{33}\hat{z} \\ \eta\vec{\nabla}B_x \\ \eta\vec{\nabla}B_y \\ \eta\vec{\nabla}B_z \\ k\vec{\nabla}T + (\bar{\bar{\tau}}.\vec{V}) - \eta(\vec{J}\times\vec{B}) \end{bmatrix} \tag{3.4}$$

$$\mathbf{S} = -\begin{bmatrix} 0 \\ 0 \\ 0 \\ 0 \\ (\vec{\nabla}\eta\times\vec{J}).\hat{x} \\ (\vec{\nabla}\eta\times\vec{J}).\hat{y} \\ (\vec{\nabla}\eta\times\vec{J}).\hat{z} \\ 0 \end{bmatrix} - \left(\vec{\nabla}.\vec{B}\right)\begin{bmatrix} 0 \\ B_x \\ B_y \\ B_z \\ u \\ v \\ w \\ (\vec{V}.\vec{B}) \end{bmatrix} \tag{3.5}$$

$$\frac{\Delta\mathbf{U_i}}{\Delta t}\,\Omega_i + \sum_{j=1}^{N_f}\left(\vec{\mathbf{F}}_{inv}.\hat{n}\right)_{ij}\,A_{ij} = \sum_{j=1}^{N_f}\left(\vec{\mathbf{F}}_{diff}.\hat{n}\right)_{ij}\,A_{ij} + \mathbf{S}\,\Omega_i \tag{3.6}$$

$$\Delta\mathbf{U_i} = \mathbf{U_i^{n+1}} - \mathbf{U_i^n} \tag{3.7}$$

Consider cell i as shown in figure 3.1 surrounded by four different cells (j=1,2..4). The finite volume formulation applied to the governing equations for this cell would give rise to Eq. 3.6. Here $\Delta\mathbf{U_i}$ represents the change in

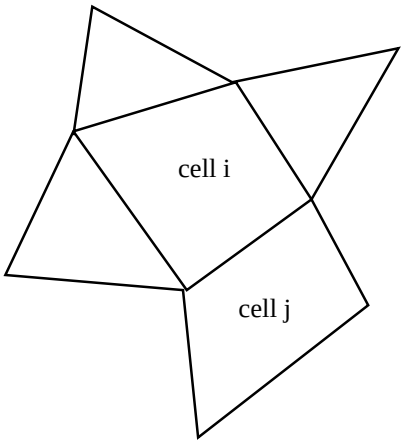

Figure 3.1: Unstructured grid showing cell i surrounded by four different cells

conservative variables between successive time levels n and $n+1$ as shown in equation 3.7, Δt is the time step, Ω_i is the volume of cell i, A_{ij} is the area of the face f that separates cells i and j, $\hat{n}$ is the unit normal to the face directed from cell i to cell j, and N_f is the number of faces surrounding cell i. The basic technique to find a steady state solution to Eq. 3.6 is through time stepping. An implicit time stepping scheme can be formulated for each cell i in an unstructured grid framework as shown below in Eq. 3.8.

$$\frac{\Delta \mathbf{U}}{\Delta t}\,\Omega_i + \sum_{j=1}^{N_f} \left(\vec{\mathbf{F}}_{inv}.\hat{n}\right)_{ij}^{n+1} A_{ij} = \sum_{j=1}^{N_f} \left(\vec{\mathbf{F}}_{diff}.\hat{n}\right)_{ij}^{n+1} A_{ij} + \mathbf{S}^{n+1}\,\Omega_i \qquad (3.8)$$

3.3 Implicit treatment of inviscid flux

The subsequent linearization of the inviscid flux term from Eq. 3.8 for a particular face f that separates cells i and j (Fig. 3.1) can be written as

shown in Eq. 3.9. Note that the flux at the face that separates cells i and j depend only on the values of conservative variables on its left and right cells.

$$\left(\vec{\mathbf{F}}_{inv}.\hat{n}\right)_{ij}^{n+1} = \left(\vec{\mathbf{F}}_{inv}.\hat{n}\right)_{ij}^{n} + \left(\frac{\partial\left(\vec{\mathbf{F}}_{inv}.\hat{n}\right)_{ij}}{\partial \mathbf{U_i}}\right)^{n} \Delta \mathbf{U_i}^{n} + \left(\frac{\partial\left(\vec{\mathbf{F}}_{inv}.\hat{n}\right)_{ij}}{\partial \mathbf{U_j}}\right)^{n} \Delta \mathbf{U_j}^{n} \tag{3.9}$$

The terms on the right hand side of Eq. 3.9 involve the convective flux Jacobians associated with each cell interface. One approach to calculating the Jacobian is through a finite-difference method which involves perturbing each of the 8 conservative variables and calculating the change in the inviscid flux. This is computationally expensive for large scale three dimensional MHD calculations. An alternative technique is to derive the flux Jacobian analytically, which is invariably much more accurate than the finite-difference approach. The inviscid flux at face f can be written as shown in Eq. 3.10. Here we use a Lax Friedrich's method [105] for simplicity of calculation where $(\vec{\mathbf{F}}_{inv}.\hat{n})_i$ and $(\vec{\mathbf{F}}_{inv}.\hat{n})_j$ represent the component of inviscid flux along the face normal computed from cell center values of conservative variables, λ_{max} is the fastest wave speed which is the sum of the contravariant velocity and the fast plasma wave speed at face f as shown in Eq. 3.11. λ_{max} is also a function of the conservative variables at cells i and j. The contravariant velocity $\vec{V}.\hat{n}$, acoustic wave speed a, magnitude of magnetic field $|\vec{B}|$ and its normal component B_n are obtained as arithmetic averages of values from either cell.

$$\left(\vec{\mathbf{F}}_{inv}.\hat{n}\right)_{ij} = \frac{\left(\vec{\mathbf{F}}_{inv}.\hat{n}\right)_i + \left(\vec{\mathbf{F}}_{inv}.\hat{n}\right)_j}{2} - \frac{|\lambda_{max}|\left(\mathbf{U_j} - \mathbf{U_i}\right)}{2} \tag{3.10}$$

$$\lambda_{max}(\mathbf{U_i}, \mathbf{U_j}) = |\vec{V}.\hat{n}| + \sqrt{\frac{1}{2}\left(a^2 + \frac{|\vec{B}|^2}{\rho} + \sqrt{\left(a^2 + \frac{|\vec{B}|^2}{\rho}\right)^2 - 4\frac{B_n^2}{\rho}a^2}\right)} \tag{3.11}$$

$$\left(\frac{\partial\left(\vec{\mathbf{F}}_{inv}.\hat{n}\right)_{ij}}{\partial \mathbf{U_i}}\right) = \frac{1}{2}\left(\frac{\partial\left(\vec{\mathbf{F}}_{inv}.\hat{n}\right)_i}{\partial \mathbf{U_i}}\right) + \frac{|\lambda_{max}|I}{2} \tag{3.12}$$

$$\left(\frac{\partial\left(\vec{\mathbf{F}}_{inv}.\hat{n}\right)_{ij}}{\partial \mathbf{U_j}}\right) = \frac{1}{2}\left(\frac{\partial\left(\vec{\mathbf{F}}_{inv}.\hat{n}\right)_j}{\partial \mathbf{U_j}}\right) - \frac{|\lambda_{max}|I}{2} \tag{3.13}$$

Equations 3.12 and 3.13 represent the Jacobian obtained from differentiation of numerical flux shown in Eq. 3.10. Note that λ_{max} in equation 3.10 is a function of the conservative variables at cells i and j and hence should also be differentiated further to obtain the true Jacobian associated with the numerical flux. It is assumed to be locally constant in this work. This approximation can potentially restrict the maximum Courant number for stable calculations as well as steady state convergence rates [106]. Other methods that can be an improvement on the current strategy is to use differentiable fluxes such as Osher flux [107] or automatic differentiation of source code [108]. The above equations are written for an interior face which has a left and a right cell

adjacent to it. At boundary cells, only the diagonal contribution from Eq. 3.12 is used. The addition on the diagonal tends to stabilize the matrix solve calculations. The Jacobian matrices in Eqs. 3.12 and 3.13 can be computed by writing the cell center inviscid flux in terms of the conservative variables $\mathbf{U} = [U_0, U_1, ...U_7]$, such that the variables in the original governing equations are defined in terms of the conservative variables as shown in Eq. 3.14.

$$
\begin{aligned}
u = \frac{U_1}{U_0}; v = \frac{U_2}{U_0}; w = \frac{U_3}{U_0} \\
P_t = (\gamma - 1)\left(U_7 - \frac{U_1^2 + U_2^2 + U_3^2}{2U_0}\right) + \frac{(2-\gamma)}{2}\left(U_4^2 + U_5^2 + U_6^2\right) \\
\vec{V}.\vec{B} = \frac{(U_1 U_4 + U_2 U_5 + U_3 U_6)}{U_0}
\end{aligned} \tag{3.14}
$$

0	n_x	n_y	n_z	0	0	0	0
$\frac{1}{2}\gamma_1\lvert V\rvert^2 n_x - uV_n$	$-\gamma_2 u n_x + V_n$	$-\gamma_1 v n_x + u n_y$	$-\gamma_1 w n_x + u n_z$	$-\gamma_1 B_x n_x - B_n$	$-\gamma_2 B_y n_x - B_x n_y$	$-\gamma_2 B_z n_x - B_x n_z$	$\gamma_1 n_x$
$\frac{1}{2}\gamma_1\lvert V\rvert^2 n_y - vV_n$	$v n_x - \gamma_1 u n_y$	$-\gamma_2 v n_y + V_n$	$-\gamma_1 w n_y + v n_z$	$-B_y n_x - \gamma_2 B_x n_y$	$-\gamma_1 B_y n_y - B_n$	$-\gamma_2 B_z n_y - B_y n_z$	$\gamma_1 n_y$
$\frac{1}{2}\gamma_1\lvert V\rvert^2 n_z - wV_n$	$w n_x - \gamma_1 u n_z$	$w n_y - \gamma_1 v n_z$	$-\gamma_2 w n_z + V_n$	$-B_z n_x - \gamma_2 B_x n_z$	$-B_z n_y - \gamma_2 B_y n_z$	$-\gamma_1 B_z n_z - B_n$	$\gamma_1 n_z$
$-\frac{1}{\rho}((B_x v - uB_y)n_y + (B_x w - uB_z)n_z)$	$-\frac{1}{\rho}(B_y n_y + B_z n_z)$	$\frac{1}{\rho} B_x n_y$	$\frac{1}{\rho} B_x n_z$	$v n_y + w n_z$	$-u n_y$	$-u n_z$	0
$-\frac{1}{\rho}((B_y u - vB_x)n_x + (B_y w - vB_z)n_z)$	$\frac{1}{\rho} B_y n_x$	$-\frac{1}{\rho}(B_x n_x + B_z n_z)$	$\frac{1}{\rho} B_y n_z$	$-v n_x$	$u n_x + w n_z$	$-v n_z$	0
$-\frac{1}{\rho}((B_z u - wB_x)n_x + (B_z v - wB_y)n_y)$	$\frac{1}{\rho} B_z n_x$	$\frac{1}{\rho} B_z n_y$	$-\frac{1}{\rho}(B_x n_x + B_y n_y)$	$-w n_x$	$-w n_y$	$u n_x + v n_y$	0
$(\frac{1}{2}\gamma_1\lvert V\rvert^2 - \frac{1}{\rho}(\rho Z + P_t))V_n + \frac{1}{\rho}(\vec{V}.\vec{B})B_n$	$-\gamma_1 u V_n - \frac{1}{\rho} B_x B_n + \frac{1}{\rho}(\rho Z + P_t)n_x$	$-\gamma_1 v V_n - \frac{1}{\rho} B_y B_n + \frac{1}{\rho}(\rho Z + P_t)n_y$	$-\gamma_1 w V_n - \frac{1}{\rho} B_z B_n + \frac{1}{\rho}(\rho Z + P_t)n_z$	$-\gamma_2 B_x V_n - uB_n - (\vec{V}.\vec{B})n_x$	$-\gamma_2 B_y V_n - vB_n - (\vec{V}.\vec{B})n_y$	$-\gamma_2 B_z V_n - wB_n - (\vec{V}.\vec{B})n_z$	γV_n

Table 3.2: Inviscid flux Jacobian in terms of primitive and conservative variables

Substituting Eq. 3.14 into Eq. 3.3, we get the cell center inviscid flux

Jacobian in terms of the primitive variables as shown in Table 3.2. Additional variables used in the Jacobian matrix (Table 3.2) are given in Eq. 3.15.

$$
\begin{aligned}
V_n &= un_x + vn_y + wn_z \\
B_n &= B_x n_x + B_y n_y + B_z n_z \\
\gamma_1 &= \gamma - 1; \gamma_2 = \gamma_2 - 2
\end{aligned}
\tag{3.15}
$$

where (n_x, n_y, n_z) are the components of the unit normal vector to the cell face. This matrix is similar to that derived by Brio et al. [4] for the one dimensional case where the magnetic field equation along the spatial coordinate direction is neglected due to divergence free constraint. The matrix in Table 3.2 recovers the one dimensional version if the face normal is assumed to be along just one coordinate direction.

The Eigen values for the inviscid flux Jacobian was verified using symbolic function evaluations in the software MATHEMATICA [109]. The Eigen values are of the form $(V_n - c_f, V_n - \alpha, V_n - c_s, 0, V_n, V_n + c_s, V_n + \alpha, V_n + c_f)$ where c_s, α and c_f are the wave speeds corresponding to slow plasma waves, Alfven waves and fast plasma waves, as shown in Eq. 3.16.

$$\alpha^2 = \frac{B_n^2}{\rho}$$

$$a^2 = \frac{\gamma P}{\rho}$$

$$2c_f^2 = a^2 + \frac{|\vec{B}|^2}{\rho} + \sqrt{\left(a^2 + \frac{|\vec{B}|^2}{\rho}\right)^2 - 4\frac{B_n^2}{\rho}a^2}$$

$$2c_s^2 = a^2 + \frac{|\vec{B}|^2}{\rho} - \sqrt{\left(a^2 + \frac{|\vec{B}|^2}{\rho}\right)^2 - 4\frac{B_n^2}{\rho}a^2} \tag{3.16}$$

3.3.1 Implicit treatment of diffusion terms

The diffusion flux in Eq. 3.4 consists of viscous terms, magnetic diffusion as well thermal conduction terms. The gradients of the conservative variables at the cell centres are computed using the Green Gauss reconstruction technique [110]. The gradient $\vec{\nabla}\mathbf{U}|_{ij}$ is computed at the interface between any two cells i and j using the scheme proposed by Haselbacher et al. [111] as shown below.

$$\overline{\vec{\nabla}\mathbf{U}}|_{ij} = \frac{1}{2}\left(\vec{\nabla}\mathbf{U}|_i + \vec{\nabla}\mathbf{U}|_j\right) \tag{3.17}$$

$$\vec{\nabla}\mathbf{U}|_{ij} = \overline{\vec{\nabla}\mathbf{U}}|_{ij} - \left(\overline{\vec{\nabla}\mathbf{U}}|_{ij}.\hat{d}_{ij}\right)\hat{d}_{ij} + \frac{(\mathbf{U}_j - \mathbf{U}_i)}{d_{ij}}\hat{d}_{ij} \tag{3.18}$$

$\vec{\nabla}\mathbf{U}|_i$ and $\vec{\nabla}\mathbf{U}|_j$ represent the gradient of conservative variables at the cell centres of cells i and j. $\hat{d}_{ij}$ represents the unit vector along the line connecting the centroids of cells i and j. The implicit contribution of the diffusion

operator is the diagonal term that arises from the third term in Eq. 3.18. The diffusion velocity is added along with the spectral radius term while updating the diagonal contribution at each cell. The diffusion velocity at the interface between cells i and j (Fig. 3.1) is given by $v_D = \frac{\nu}{d_{ij}}$ where d_{ij} is the distance between the centroids of i and j and ν is the diffusion coefficient as shown in Eq. 3.19 for the different equations. ν_{vel}, ν_B and ν_T are diffusion coefficients for velocity, magnetic field and energy respectively. Note that these coefficients are not scaled and C_p is the specific heat at constant pressure.

$$\nu_{vel} = \frac{\mu}{\rho} \quad \nu_B = \frac{1}{\mu_0 \sigma} \quad \nu_T = \frac{k}{\rho C_p} \tag{3.19}$$

The implicit treatment of the magnetic diffusion term is important for simulations at higher resistivity due to extremely small magnetic diffusion time scales. The explicit treatment of these terms can lead to stringent time step restrictions.

3.3.2 Matrix solution strategy

Equations 3.12 and 3.13 compute the face inviscid flux Jacobians in Eq. 3.9 as a function of neighboring cell center matrices. Substituting Eq. 3.9 into Eq. 3.8 we get a linear equation with the change in the conservative variables for each cell as the unknowns and the sum of all the known explicit terms on the right hand side. In total we have N linear equations for N cells in an unstructured grid. Note that each linear system associated with a cell consists of eight equations corresponding to the eight different conservation equations.

Therefore, the implicit algorithm will involve an 8N x 8N linear system solve at each time step.

One approach to solving the linear system is to assemble a global sparse matrix and solve the system using an iterative method such as GMRES (Generalized Minimum Residual) [112] with a pre-conditioning technique such as block Jacobi. A parallel implementation of this technique is available in the PETSc (Portable Extensible Toolkit for Scientific computation) libraries [113] as one among many sparse linear solvers. The major disadvantage of this technique is the memory cost associated with storing the sparse matrix and the cost associated with storage for the iterative solution algorithm and also the computational cost of time spent on evaluating the values in the global matrix.

Another alternative is a matrix free method where the convective flux Jacobian is not stored explicitly and a global matrix is never created. One of the many matrix free technique known as the LU-SGS [114, 115] (Lower Upper Symmetric Gauss Seidel) algorithm can be summarized as follows. The linear system to be solved can be written as $[\mathbf{A}][X] = [B]$ where $[\mathbf{A}]$ is the global matrix obtained from combining Eqs. 3.8 and 3.9, $[X]$ is the solution vector which represents the change in value of the conservative variables $\Delta\mathbf{U}$ and $[B]$ represents terms in the discrete equation that are treated explicitly. The global matrix $[\mathbf{A}]$ can be written as a sum of a lower triangular $[\mathbf{L}]$, diagonal $[\mathbf{D}]$ and upper triangular matrix $[\mathbf{U}]$ (that is $[\mathbf{A}] = [\mathbf{L}] + [\mathbf{D}] + [\mathbf{U}]$) and the linear equation can be cast into the form as shown below in Eq. 3.20. Note that the left hand side of Eq. 3.20 simplifies to give an approximation of the

matrix as shown in Eq. 3.21.

$$([\mathbf{D}] + [\mathbf{L}])\,[\mathbf{D}]^{-1}\,([\mathbf{D}] + [\mathbf{U}])\,[X] = [B] + [\mathbf{L}][\mathbf{D}]^{-1}[\mathbf{U}][X] \tag{3.20}$$

$$\begin{aligned}([\mathbf{D}] + [\mathbf{L}])\,[\mathbf{D}]^{-1}\,([\mathbf{D}] + [\mathbf{U}]) &= [\mathbf{L}] + [\mathbf{D}] + [\mathbf{U}] + [\mathbf{L}][\mathbf{D}]^{-1}[\mathbf{U}] \\ &= [\mathbf{A}] + [\mathbf{L}][\mathbf{D}]^{-1}[\mathbf{U}] \end{aligned} \tag{3.21}$$

The above technique can be written as two steps - a forward sweep and a backward sweep. The forward sweep corresponds to solving the system, $([\mathbf{D}] + [\mathbf{L}])\,[X]^{*} = [B]$, while the backward sweep solves the system, $([\mathbf{D}] + [\mathbf{U}])\,[X] = [\mathbf{D}][X]^{*}$, resulting in the approximate solution of the system in Eq. 3.20 by neglecting the last term on the right hand side of the equation. This term will typically be a small contribution for diagonally dominant sparse matrices, but the approximate factorization due to neglect of this term can severely affect steady state convergence rates compared to global matrix solve method for low speed flows as will be seen in section 4.3 when discussing the Hartmann flow problem. The forward and backward sweeps can be written in discrete form for every cell i as a function of flux contributions from its neighboring cells j as shown in the following Eqs. 3.22 and 3.23. Here $\hat{n}$ and A_f represents the unit normal and area magnitude of the face that separates cell i and j. $\mathbf{R}_i$ represents the sum of all explicit terms for the cell i. $[\mathbf{D}_i]$ represents the local diagonal contribution to the global matrix at cell i.

$$\Delta \mathbf{U}_i^* = [\mathbf{D}_i]^{-1} \left(\mathbf{R}_i - \sum_{j:j<i} \frac{1}{2} \left(\Delta \left(\vec{\mathbf{F}}_{inv}.\hat{n} \right)_j - |\lambda_{max}| \, \Delta \mathbf{U}_j^* \right) A_f \right) \tag{3.22}$$

$$\Delta \mathbf{U}_i = \left([X]_i^* - [\mathbf{D}_i]^{-1} \sum_{j:j>i} \frac{1}{2} \left(\Delta \left(\vec{\mathbf{F}}_{inv}.\hat{n} \right)_j - |\lambda_{max}| \, \Delta \mathbf{U}_j \right) A_f \right) \tag{3.23}$$

The value of the change in inviscid flux is computed as shown in Eq. 3.24 where [**J**] is the analytically derived convective flux Jacobian.

$$\Delta \left(\vec{\mathbf{F}}_{inv}.\hat{n} \right)_j = \left(\vec{\mathbf{F}}_{inv}(\mathbf{U}_j + \Delta \mathbf{U}_j).\hat{n} \right) - \left(\vec{\mathbf{F}}_{inv}(\mathbf{U}_j).\hat{n} \right) = [\mathbf{J}] \Delta \mathbf{U}_j \tag{3.24}$$

3.4 Parallel implementation

The forward and backward sweeps described by Eq. 3.22 and 3.23, cannot be parallelized because of the inherent dependencies. For instance, to find the value of $[X]_{i+1}$ in the forward sweep, the updated value of $[X]_i$ is required. The intuitive way of partitioning the mesh and distributing contiguous rows to each processor will result in a sequence of blocking calculations where one processor will have to wait until the one sharing its adjacent set of rows has finished its work. The current implementation uses the structure of the global matrix to create data parallelism. The entries in the global matrix are related to the numerical stencil used in writing out the finite volume scheme, given by Eq. 3.6. For a cell i (shown in Fig. 3.1), the entries in the global matrix corresponds to only its neighbors. Therefore a coloring scheme similar to the

red- black Gauss Seidel technique [116] is used here. The only difference here is that there could more than just 2 colors required, so that no two adjacent cells in the unstructured grid have the same color. The operations can then be vectorized by performing the Gauss-Seidel iterations for each color, one after the other. This technique has been used previously in semi-implicit methods for solving compressible Navier-Stokes equations on unstructured grids [117, 118].

3.4.1 Pre-processing of the unstructured grid

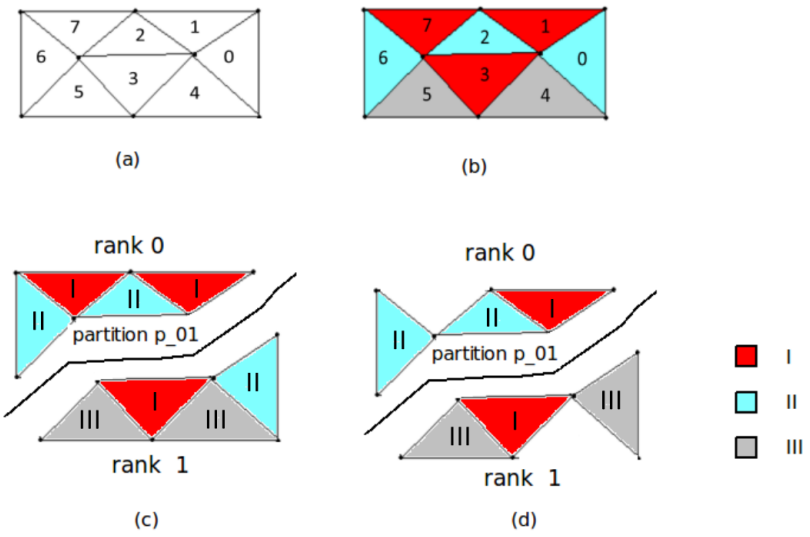

Figure 3.2: (a) Unstructured mesh with cells numbered from 0 to 7, (b) mesh after coloring is done (c) mesh is partitioned among 2 processors (d) partition boundary and the adjacent cells that live on either processor.

The general algorithm that is followed to pre-process the mesh is as follows. Fig. 3.2 shows the mesh pre-processing steps required for the coloring algorithm. Fig. 3.2(a) shows the layout of a simple unstructured mesh with 8

cells and Fig. 3.2(b) shows the same mesh after coloring is done. A total of three colors numbered I to III is used in the coloring. A sequential algorithm is used to assign colors to each cell [119], which in general leads to sub-optimal coloring. This technique is of linear complexity with respect to the number of cells. Fig. 3.2(c) shows the partitioned mesh on two processors, p_01 being the partition boundary. Fig. 3.2(d) shows the partition boundary and the adjacent cells from either processor. After the partitioning is done, one more step is required to store the coloring scheme in the ghost cells for each processor. This is achieved by creating two maps per partition boundary on each processor that stores the coloring information corresponding to cells on either side of each boundary face. The algorithm for pre-processing of the mesh is as shown below.

```
1. Read mesh and create cell,face and node data structures

2. Assign color to each cell so that no adjacent
   cell have the same color; do steps I,II

I. Create a graph with cells as vertices and edges
   being their connectivity

II. Color the graph using a sequential coloring method

3.  Partition the mesh
```

```
4.  Assign ghost color to each face on all partitions
    do steps I, II

I.  Get color of cell on the other side of a
partition boundary face

II. Assign ghost color at partition boundary
for each face
```

3.4.2 LU-SGS algorithm

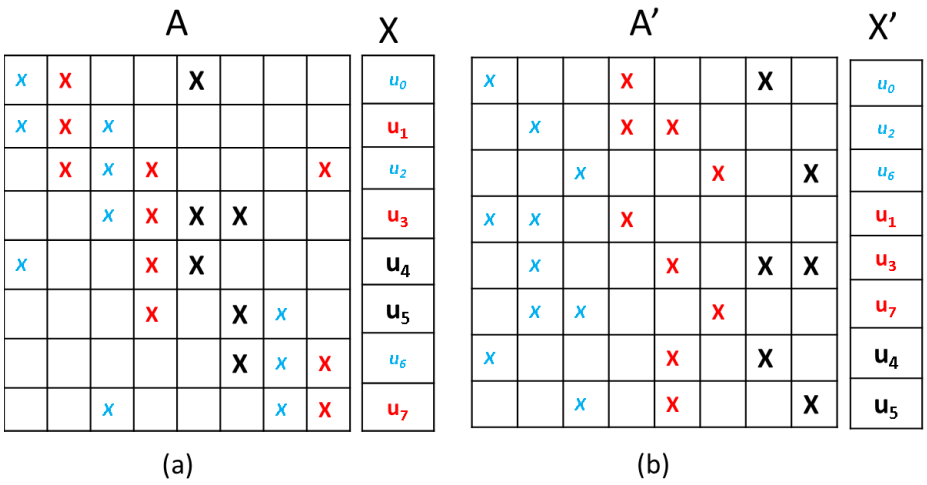

Figure 3.3: (a) Global matrix for the example mesh shown in Fig. 3.2 and (b) Reordered global matrix with clustering of solution vector $[X]$ elements with same color. Note that the colored entries are also distinguished by the font size.

Fig. 3.3(a) and 3.3(b) demonstrates the inherent data parallelism that

can be formulated using the coloring algorithm. The global matrix for the example mesh shown in Fig. 3.2 is depicted in Fig. 3.3(a).

Note that every element of matrix A is an 8 x 8 matrix corresponding to the 8 conservation equations for mass, momentum, energy and induced magnetic field. Each element of the $[X]$ vector is the tuple of the change in the 8 conservative variables between successive time levels at each cell center. The rows of the matrix represent the linear system associated with a particular cell. The equations are ordered from cell 0 to cell 7. The potential non-zero entries in the A matrix are marked by "x" with the color/font size associated with the cell under consideration. Fig. 3.3(b) shows the same linear system where the solution vector is reordered by grouping elements of the same color together which results in the interchange of rows in the global matrix. The forward sweep can now be performed on each color without dependencies. For instance, all the blue colored elements in the solution vector $[X]$ can be computed using a vectorized operation because no element of the same color exists on the left side of the diagonal. Similarly, the subsequent calculation for the red elements would require only the updated values of blue elements performed in the previous step. The backward sweep can also be done without dependencies by reversing the order in which the colors are dealt with.

There are mainly four different steps involved in the LU-SGS technique. First step is to compute the explicit flux terms which will constitute the $[B]$ vector in the linear system ($[\mathbf{A}][X] = [B]$). The second step is to compute $[\mathbf{D}_i]^{-1}$ associated with each cell. Note that $[\mathbf{D}_i]$ is an 8 x 8 matrix that involves the flux Jacobian at a given cell and the numerical dissipation term along with

the time derivative term. The numerical dissipation contribution is an identity matrix scaled by the spectral radius of the convective flux Jacobian (sum of fast plasma wave speed and the fluid speed). The inversion of matrix $[\mathbf{D}_i]$ is a time consuming process. Hence, the contribution of the spectral radius and time derivative terms are only used to do this calculation as shown in Eq. 3.25. Here I represents an 8 x 8 identity matrix. The diffusion velocities are also added along with λ_{max} at cell interfaces to stabilize the diffusion terms.

$$[\mathbf{D}_i] = \left[\frac{\Omega_i}{\Delta t} + \sum_{j=1}^{N_f} \lambda_{max}(\mathbf{U_i}, \mathbf{U_j}) A_{ij} \right] I \tag{3.25}$$

The third and the fourth steps are the forward and backward sweeps respectively. The forward sweep is done one color after the other. The coloring of the cells eliminates dependencies and can be easily vectorized, except at the boundaries of each partition. The ghost values for conservative variables, $\mathbf{U}$ and $\Delta\mathbf{U}$ have to be updated at partition boundaries for the color that is already iterated. A special set of iterations at the partition boundary cells has to be done by each processor using the updated values of conservative variables across the boundary. For the example mesh shown in Fig. 3.2, while processor 0 performs the calculations for color II at the partition boundary, it needs the values of conservative variables of cells in processor 1 that has a color I and color III. This information is communicated by processor 1, which is stored as values on a layer of ghost cells on processor 0. The backward sweep algorithm is almost the same as the forward sweep except that the looping of the colors is reversed. The updated value of $\Delta\mathbf{U}$ from the forward sweep is used for the

backward sweep update.

3.5 Other numerical aspects

3.5.1 Dual-time implicit method

The semi-implicit method developed here is extremely dissipative for large time steps resulting in large errors for a time accurate calculation. The method developed works very well for steady-state problems where accuracy in time is not required. To solve the equations accurately in time, a dual-time algorithm [65] can be used to modify the existing implicit method. The algorithm essentially consists of performing sub-iterations for every physical time step. The original finite volume approximation given in Eq. 3.6 can be written as shown below.

$$\frac{\Delta \mathbf{U}}{\Delta t}\Omega_{cell} + \mathbf{R} = 0 \tag{3.26}$$

Here $\mathbf{R}$ represents the residual term which consists of the convective and diffusive fluxes as well as the source term contributions. This equation is inherently non-linear which requires either Newton's method or a time-stepping method to solve it accurately in time. The time stepping method can be used to let the second term in Eq. 3.27 go to zero at steady state. Here t^* is referred to as the pseudo-time variable.

$$\frac{d\mathbf{U}}{dt^*}\Omega_{cell} + \left(\frac{\Delta \mathbf{U}}{\Delta t}\Omega_{cell} + \mathbf{R}\right) = 0 \tag{3.27}$$

Therefore the time accurate calculation is reduced to solving a steady state problem in t^* at each physical time step. The implicit method for Eq. 3.27 can be formulated as shown below. Here m denotes time level in pseudo-time while n is the time level in actual physical time.

$$\frac{\Delta \mathbf{U}}{\Delta t^*}\Omega_{cell} + \left(\frac{\Delta \mathbf{U}}{\Delta t}\Omega_{cell} + \mathbf{R}\right)^{m+1} = 0 \tag{3.28}$$

Here,

$$\left(\frac{\Delta \mathbf{U}}{\Delta t}\Omega_{cell} + \mathbf{R}\right)^{m+1} = \frac{(\mathbf{U}^{m+1} - \mathbf{U}^n)}{\Delta t}\Omega_{cell} + \mathbf{R}^m + \frac{\partial \mathbf{R}}{\partial \mathbf{U}}\Delta \mathbf{U} \tag{3.29}$$

$$\left(\Omega_{cell}\left(\frac{1}{\Delta t^*} + \frac{1}{\Delta t}\right) I + \frac{\partial \mathbf{R}}{\partial \mathbf{U}}\right)\Delta \mathbf{U} = \frac{(\mathbf{U}^n - \mathbf{U}^m)}{\Delta t} - \mathbf{R}^m \tag{3.30}$$

Note that $\Delta \mathbf{U} \equiv \mathbf{U}^{m+1} - \mathbf{U}^m$ denotes the difference in the conservative variables between successive pseudo-time steps within a given physical time step.

3.5.2 Higher order inviscid flux discretization

The semi-implicit method developed, assumed a simple Lax Friedrich's formulation for the inviscid flux to obtain the linear operator. However the calculation of the explicit term $\left(\vec{\mathbf{F}}_{inv}.\hat{n}\right)_{ij}^{n}$ in Eq. 3.9 can be in principle, obtained through any stable flux discretization and the implicit scheme is observed to be stable. A higher order Lax Friedrich's scheme can be formulated by obtaining

the gradients of the primitive variables within each cell and reconstructing a higher order estimate for the left and right states across a face. This is shown in Eq. 3.31 for cells i and j in Fig. 3.1 assuming the face normal is from i to j.

$$\left(\vec{\mathbf{F}}_{inv}.\hat{n}\right)_{ij} = \frac{\vec{\mathbf{F}}_{inv}\left(\mathbf{U}_i'\right).\hat{n} + \vec{\mathbf{F}}_{inv}\left(\mathbf{U}_j'\right).\hat{n}}{2} - \frac{|\lambda_{max}|\left(\mathbf{U}_j' - \mathbf{U}_i'\right)}{2} \tag{3.31}$$

Here $\mathbf{U}_i'$ and $\mathbf{U}_j'$ represent higher order estimates of the conservative variables on the left and right sides of the face that separates cells i and j. The values of the primitive variables $W = [\rho, u, v, w, B_x, B_y, B_z, P]$ are first reconstructed at the face locations of each cell using their gradients as shown below.

$$W_k{}' = W_k + \vec{\nabla} W_k.\vec{r}_{if} \;\; (k = 0, 1, 2, 3...7) \tag{3.32}$$

Eq. 3.32 represents the second-order estimate of W_k for the cell i. Here $\vec{r}_{if}$ is the vector that connects the centroid of cell i with the centroid of face that separates cells i and j. The higher order estimate for the conservative variables is then obtained using these values. The gradients are calculated using the Green Gauss gradient reconstruction technique [110]. The Barth gradient limiter [120] was used to perform stable calculations using the above method.

A modified E-CUSP (Convective Upwind Splitting) scheme [121] is also implemented to obtain the inviscid flux. The E-CUSP scheme splits $\vec{\mathbf{F}}_{inv}$ into convective and pressure flux terms. The convective term at the face is

computed based on upwind direction while the pressure flux is weighted based on fast magneto-sonic Mach number.

3.5.3 Boundary conditions

3.5.3.1 Inflow and outflow boundaries

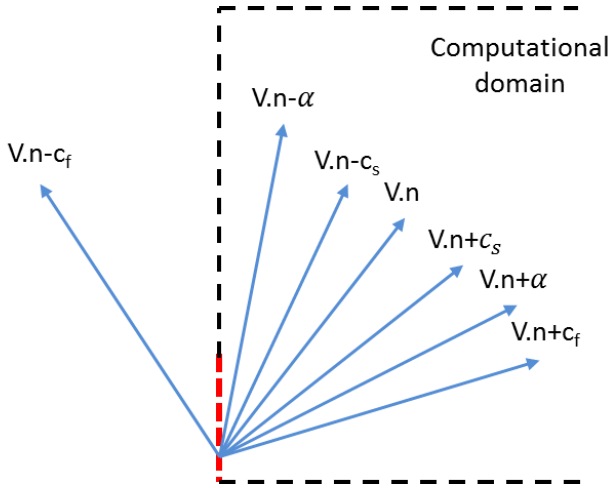

Figure 3.4: An inflow case where only one of the characteristics come out of the computational domain at boundary face shown in red

A characteristic based boundary condition is applied at both inflow and outflow boundaries. Only a certain set of specified parameters are used to find the hyperbolic flux at inflow boundaries depending on the number of characteristics (Eigen values of the hyperbolic flux Jacobian) that go into the computational domain. At inflow boundaries, the pressure, temperature, velocity and magnetic field are specified. If the contravariant speed at the inflow face is greater than c_f (fast magnetosonic wave speed), then all the specified parameters are used. For a case (Figure 3.4) where the contravariant

speed is less than c_f and greater than α (Alfven wave speed), one of the components of magnetic field is interpolated from within the computational domain. The rest of the primitive variables are obtained from user defined values.

At outflow boundaries, the pressure and two components of magnetic field are specified. Quantities are interpolated from within the computational domain depending on the number of characteristics that go out of the computational domain.

3.5.3.2 Wall boundaries

Wall boundary condition	Remark
Inviscid	normal velocity $V_n = 0$
Viscous	velocity $\vec{V} = 0$
PEC	normal magnetic field $B_n = 0$
Dielectric	normal magnetic field need not be zero, interpolated from adjacent cell
Adiabatic	normal gradient of temperature $\vec{\nabla}T.\hat{n} = 0$
Fixed temperature	temperature at the boundary $T = T_{wall}$

Table 3.3: Different types of wall boundary conditions used in the model

The various wall boundary condition attributes used in the model are shown in Table 3.3. Inviscid walls require the normal component of velocity

to go to zero. Viscous wall boundaries require the velocity to vanish which is accomplished through a ghost cell technique [65]. A ghost cell is assumed next to the wall boundary face which has a velocity that is negative of that in the adjacent cell in the domain. These boundaries also require a condition on temperature. An Adiabatic wall condition assumes no thermal conduction flux while a fixed temperature wall assumes a Dirichlet condition for temperature. The normal component of magnetic field is assumed to be zero at PEC (Perfect Electric Conductor) boundaries which imposes the null tangential electric field condition. The magnetic field components are interpolated onto the boundary face for a dielectric wall condition.

3.5.4 Real gas effects

A calorically perfect gas assumption was made in the derivation of the governing equations in chapter 2 (Eq. 2.27) and in the flux Jacobian used in the implicit operator. The use of a constant isentropic exponent γ, and an equation of state using a temperature independent gas constant R, is not true in the case of a thermal plasma. Studies on isentropic exponent in atomic plasmas such as argon plasma has revealed that it is a constant value equal to 1.16 over ionization fractions between 5 and 80 percent [122]. This value of γ is used in the implicit operator for simulations with real gas effects in application problems studied in chapters 5 and 6. An example where a temperature dependent equation of state is necessary, is in the case of an air plasma. Diatomic nitrogen in air starts dissociating at approximately 3000 K and subsequent ionization of dissociated nitrogen becomes significant between

6000 and 7000 K [1]. The specific internal energy is also no longer a constant with temperature because of other energy transfer modes such as dissociation and ionization that come into picture.

In order to account for the variation in specific heat capacities, Eq. 2.27 is modified as shown in Eq. 3.33 where e is the specific internal energy which is assumed to be a function of temperature (thermally perfect gas assumption). The internal energy data for gases such as hydrogen and air are given in tabular form in the textbook by Boulos et al. [1].

$$\rho Z = \rho e + \frac{1}{2}\rho|V|^2 + \frac{|B|^2}{2\mu_0} \tag{3.33}$$

A look up table for specific internal energy is created for a wide range of temperatures and the total fluid energy is obtained at every time step. A linear search technique is used to obtain the temperature corresponding to a given internal energy for computing thermodynamic pressure after the conservative variables are advanced after each time step. The specific internal energy is a monotonically increasing function with respect to temperature, which allows the use of a linear search technique.

To obtain pressure from density and temperature (obtained from specific internal energy) a Newton-Raphson method is used to solve the equation of state. The gas constant is assumed to be a function of temperature obtained from tabulated data in ref. [1]. An approximate polynomial fit is obtained for both hydrogen gas and air which are the gases used in the simulations of co-axial plasma accelerator (chapter 5) and the rail plasma actuator (chapter

6) respectively.

Eq. 3.34 shows the gas constant for hydrogen in $J/kg/K$ with varying temperature in kelvin. This is used in the simulation of deflagration mode in coaxial plasma accelerator (chapter 5).

$$R = \begin{cases} 4157.0 & T \leq 2369.28, \\ 2.08e(-29)T^8 - 2.92e(-24)T^7 + 1.69e(-19)T^6 & \\ -5.13e(-15)T^5 + 8.84e(-11)T^4 - 8.54e(-7)T^3 & \\ +0.0043T^2 - 9.08T + 10479.78 & T \in (2369.28, 24900] \\ 15960.0 & T > 24900 \end{cases} \tag{3.34}$$

Eq. 3.35 shows the gas constant for air as a function of temperature in kelvin. This expression is used in the rail plasma actuator simulations in chapter 6.

$$R = \begin{cases} 287.0 & T \leq 500.0, \\ -8.82e(-16)T^5 + 9.65e(-12)T^4 - 3.63e(-8)T^3 & \\ +5.99e(-5)T^2 - 0.043T + 295.43 & T \in (500.0, 4750] \\ -8.4e(-17)T^5 + 4.26e(-12)T^4 - 8.27e(-8)T^3 & \\ +0.00076T^2 - 3.31T + 5681.9 & T \in (4750.0, 14053.0] \\ -3.22e(-17)T^5 + 3.03e(-12)T^4 - 1.12e(-7)T^3 & \\ +0.002T^2 - 18.4T + 65184.08 & T \in (14053.0, 22000.0] \\ 1120.9 & T > 22000 \end{cases} \tag{3.35}$$

The transport properties such as viscosity, thermal conductivity and electrical conductivity are also obtained as function of temperature using approximate polynomial fits from data given in ref. [1].

Chapter 4

Code verification

The verification of the MHD numerical model is presented in this chapter. The convective flux implementation is tested using the MHD shock tube as well as the oblique shock test case. The non ideal MHD effects and viscous implementation are verified through the Hartmann flow test case. The rate of convergence for steady state problems as well as parallel performance of the two implicit methods are also compared.

4.1 MHD shock tube

The MHD shock tube problem was first studied by Brio and Wu [4] and has been used extensively as a test case for the numerical discretization of convection term in MHD codes. This case is used here, to verify the numerical implementation discussed in chapter 3. Specifically, the LU-SGS approach is used here. The problem comprises of a one-dimensional magnetized plasma domain with a sharp discontinuity at a specified location and uniform conditions otherwise, at time $t = 0$. The transient evolution of the plasma serves as a verification benchmark. A finite domain from x = 0 to x = 1 (non-dim. units) is modelled here with a uniform mesh of 1000 cells. Initial non-dimensional values for pressure, density and magnetic field are given in Eq. 4.1. The x-

component of magnetic field is a constant so as to satisfy the divergence free constraint and is equal to 0.75.

$$
\begin{aligned}
P &= 1 \; \forall x < 0.5 \\
&= 0.1 \; \forall x \geq 0.5 \\
\rho &= 1 \; \forall x < 0.5 \\
&= 0.1 \; \forall x \geq 0.5 \\
B_y &= 1.0 \; \forall x < 0.5 \\
&= -1.0 \; \forall x \geq 0.5
\end{aligned} \tag{4.1}
$$

Since the problem needs a time accurate solution a dual-time implicit scheme with the LU-SGS technique was used. Sub-iterations were performed for each time step until the residual reached a relative tolerance of 10^{-4}. The physical time step was set as 0.001. The fast plasma wave transit time (ratio of mesh cell size to fast plasma wave speed) in each cell is calculated and the minimum value among all the cells is used as the pseudo time step. The Courant Friedrich Lewy (CFL) number was set to 100 for the dual-time iterations performed in each time step. Typically about 15-20 sub-iterations were required per time step to reach the tolerance value. Figure 4.1 shows the density solution at time t=0.1. The explicit part of the inviscid flux was determined using the E-CUSP scheme. The second-order spatial accuracy was achieved using the method described in section 3.5.2.

From Fig. 4.1 it is clear that the present solutions agree well with the

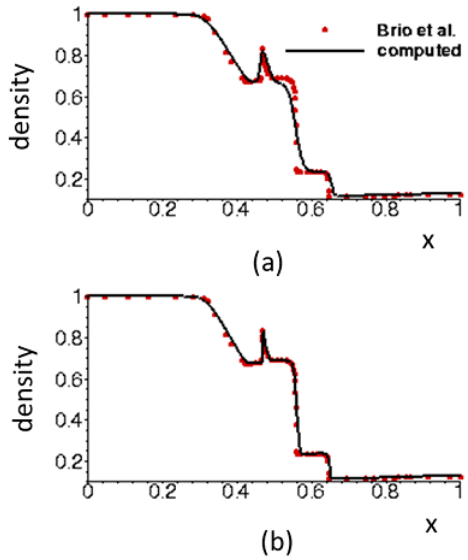

Figure 4.1: (a) 1st-order and (b) 2nd-order solution for density at time $t = 0.1$ using dual time implicit LU-SGS method compared with Brio-Wu solution on a one-dimensional mesh.

benchmark Brio-Wu solution with higher accuracy achieved with the second-order spatially accurate scheme. The technique is able to capture accurately the shocks and the expansion waves brought about by the slow and fast plasma waves, respectively. The contact and slow compound waves are also captured without much dissipation in the second-order solution despite the large CFL number used in the implicit calculation. We note that the benchmark Brio-Wu solution was computed using a second-order Roe scheme. A discussion of the various features that appear in the MHD shock tube and the non-convex nature of the MHD equations appears in appendix A.

The same MHD shock-tube problem is studied in two-dimensional planar coordinate system as shown in Fig. 4.2. The symmetry boundary condi-

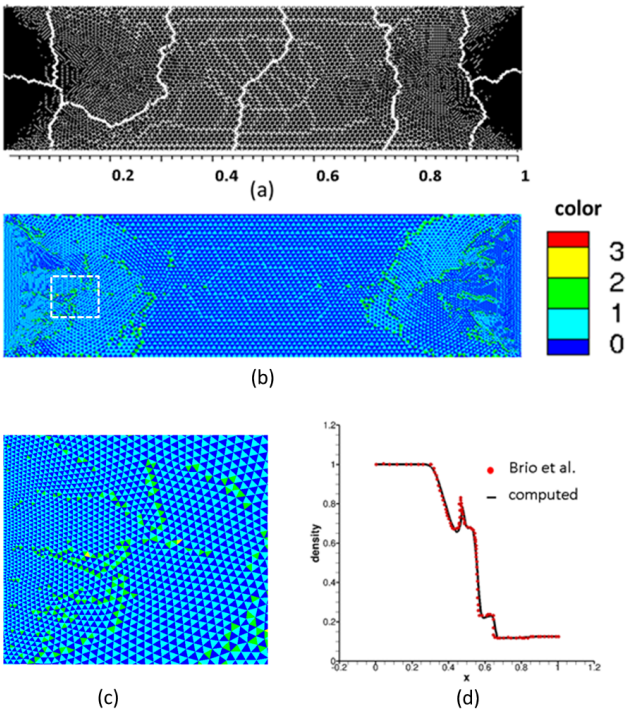

Figure 4.2: (a) Computational mesh consisting of 16,000 triangular elements along with domain decomposition, (b) coloring scheme used for the calculation, (c) closer view of the mesh with coloring information (d) density solution extracted along center line through the axis at t=0.1. The solution was computed using dual time implicit LU-SGS method.

tion is imposed at the top and bottom boundaries to specify a one-dimensional problem on the two-dimensional domain. An unstructured grid consisting of about 16,000 triangular elements was used for this calculation as shown Fig. 4.2(a). The simulation was performed using 8 processors with the domain decomposition done using the PMETIS libraries [123]. The partitioning is done in such a way that the number of cells in each domain is the same thereby ensuring load balance. The partition boundaries are shown in Fig. 4.2(a). The

coloring of the unstructured grid required four colors as shown in Fig. 4.2(b). A closer view of the mesh along with the coloring information is shown in 4.2(c). The solution extracted along a horizontal line midway between the top and bottom boundaries at time $t = 0.1$ is shown in Fig. 4.2(d). The present solution agrees well with the Brio-Wu solution thereby verifying the numerical implementation of the MHD governing equations with the LU-SGS technique.

Time integration method	CFL number	CPU time (s)
Euler Explicit	0.8	59
4th order RK(Runge-Kutta)	1.0	211
LU-SGS (tol. 10^{-2})	100*	57
LU-SGS (tol. 10^{-4})	100*	111
PETSc GMRES (tol. 10^{-2})	100*	190
PETSc GMRES (tol. 10^{-4})	100*	367

Table 4.1: CPU time comparison of explicit and implicit techniques for the two dimensional MHD shock tube problem on 8 processors. * indicates CFL number used in dual-time iterations

Table 4.1 shows the wall clock times associated with different time integration methods used to solve the two dimensional MHD shock tube. The conditions and spatial discretization schemes used were exactly the same for each of the methods. The implicit methods using LU-SGS and GMRES were done using the dual-time algorithm unlike the Euler explicit and Runge-Kutta methods. The associated relative tolerance for dual-time convergence is also varied for the two implicit methods. It is seen that the Euler explicit and the LU-SGS method with a tolerance of 10^{-2} were the fastest. The implicit

methods tend to take longer for larger relative tolerances. Implicit methods by themselves yield very dissipative solutions for high CFL numbers. The use of a dual-time algorithm is crucial to obtain time accurate solutions using the implicit methods. Tolerance of 10^{-2} was seen to be sufficient here to get solutions as accurate as the explicit methods.

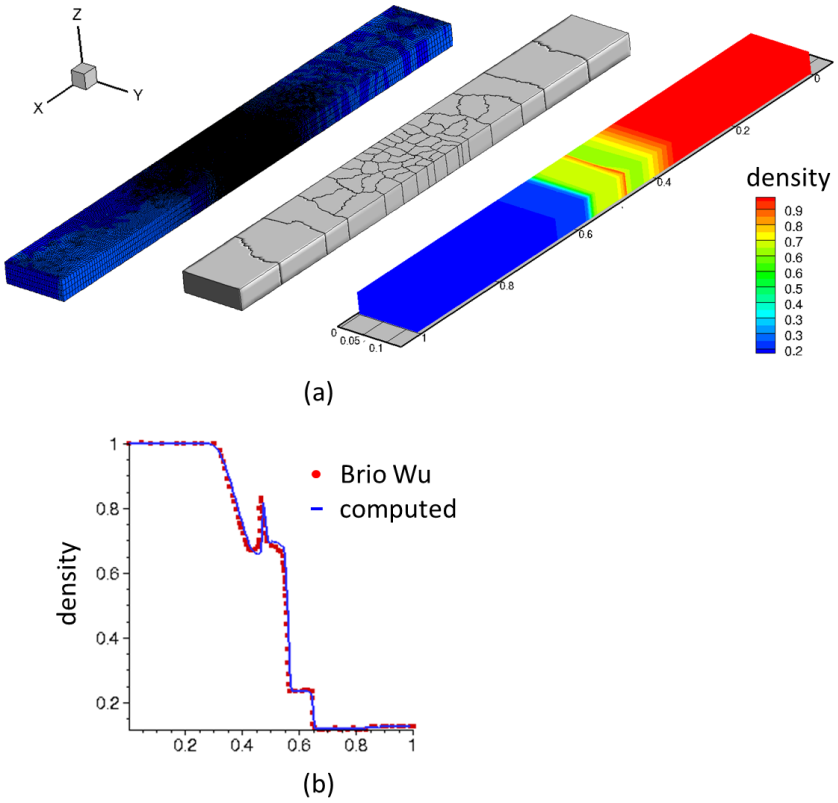

Figure 4.3: (a) Unstructured grid, partition boundaries and density solution at t=0.1 (b) Spanwise averaged density solution on an XY plane through the center compared with the Brio Wu solution. The simulation was done using dual time implicit LU-SGS method.

To assess the performance of the spatial discretization as well as the time implicit technique developed, the MHD shock tube test case is done in a

three-dimensional unstructured grid as shown in Fig. 4.3(a). The grid consists of about 185,000 hexahedrons, not necessarily rectangular in shape, with grid clustering towards the middle so as to resolve the complex wave structures that evolve until a final time $t = 0.1$. The simulation is performed on 48 cores and the partition boundaries are shown in Fig. 4.3(a).

The CFL and tolerance parameters used were the same as the one-dimensional MHD shock tube test case. About 50 iterations were required to reach the specified residual tolerance of 10^{-4} in a physical time step. The spatial discretization scheme used is a second-order E-CUSP scheme. The density solution is shown in Fig. 4.3(a) and the spanwise averaged solution on an XY plane through the center is shown in Fig. 4.3(b). The solutions agree well with the Brio-Wu solution.

4.2 MHD oblique shock problem

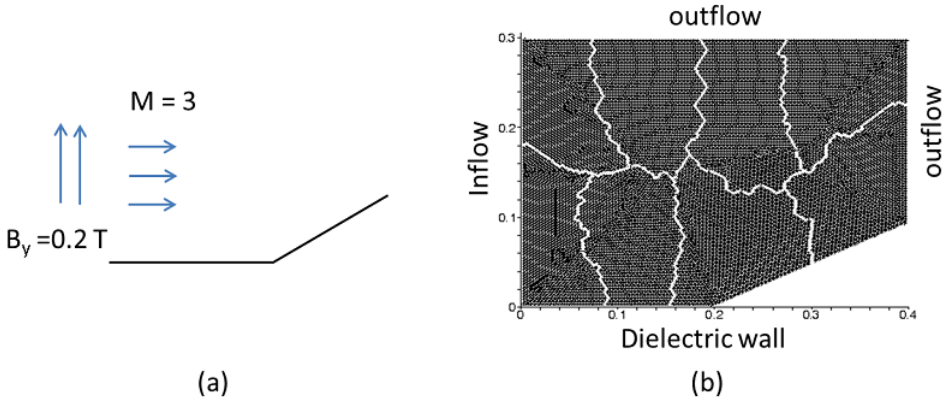

Figure 4.4: (a) Schematic of oblique shock test case and (b) computational mesh consisting of about 17,000 triangular cells partitioned on 8 processors.

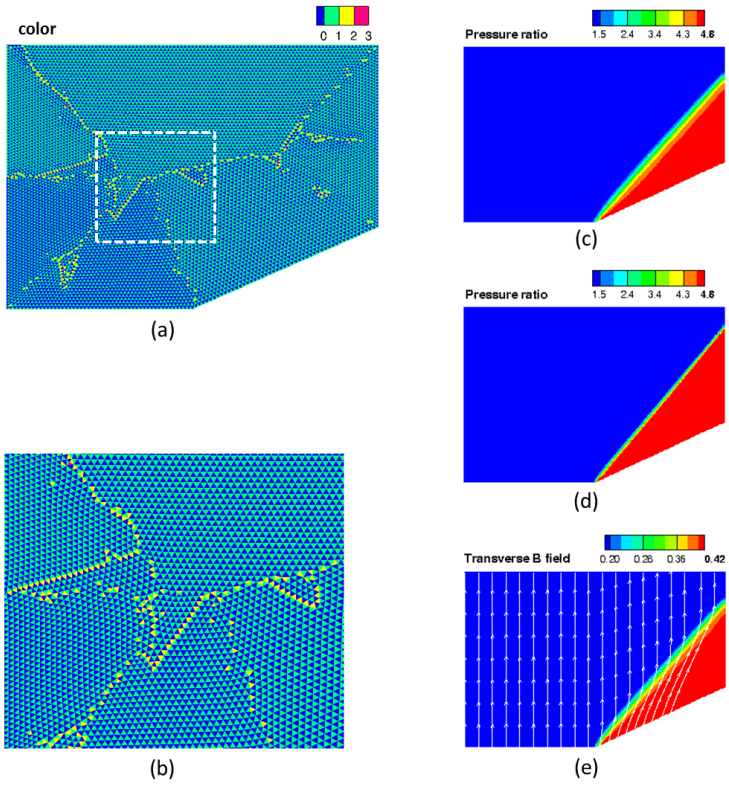

Figure 4.5: (a) Coloring of the mesh using four different colors (b) Closer view of the mesh along with coloring information (c) Pressure ratio with first-order method (d) Pressure ratio with second-order spatial discretization (e) Magnitude of transverse magnetic field with magnetic field lines.

The MHD oblique shock problem is posed as shown in Fig. 4.4. It is essentially a super- magnetosonic flow past a wedge resulting in an attached oblique shock wave. This is a two-dimensional inviscid ideal MHD test case which has a steady state solution. The Mach number with respect to the acoustic speed is 3 while the fast magnetosonic Mach number (ratio of flow speed to fast plasma wave speed) is 2.73. The wedge angle is 25^o. Pressure

and density equal to 100 kPa and 1.16 kg/m^3 are assumed as initial conditions in the domain. The x component of initial velocity is set to the value corresponding to Mach 3 in the domain. A constant y component of magnetic field along with free stream pressure and density are assumed at the inflow boundary. The top and the right boundaries are outflow boundaries where quantities are extrapolated from the interior. The outflow boundary conditions are possible because the flow speeds at these boundaries are faster than the local wave speeds resulting in characteristics directed out of the computational domain. The bottom boundary along with the wedge is assumed to be a dielectric inviscid wall. The normal component of magnetic field does not go to zero at the bottom dielectric walls, in contrast to a perfect electric conductor (PEC) boundary condition. The value of magnetic field is merely extrapolated from the cell center onto the face for flux calculation at these boundaries. The mesh consists of 17,000 triangular elements. The simulation is performed on 8 processors and the mesh partition boundaries are indicated in Fig. 4.4(b). Fig. 4.5(a) shows the mesh after the coloring step with four different colors. Fig. 4.5(b) shows a closer view of the mesh in the inset region in Fig. 4.5(a). There is an imbalance in the number of cells with a given color due to the sub-optimal coloring algorithm. Fig. 4.5(c) shows the steady state solution for the pressure ratio (pressure normalized to the free stream pressure) across the shock using the implicit scheme and 1st order Lax Friedrichs flux discretization. The pressure ratio solution using second-order Lax Friedrichs method is shown in Fig. 4.5(d). The higher-order method captures the shock within 2 cells as opposed to the more dissipative first- order method. The

magnitude of magnetic field along the shock is plotted in Fig. 4.5(e) for the observed shock angle of 50 degrees. The transverse component increases across the shock indicating that the shock is formed due to fast magnetosonic waves. The magnetic field lines along with contours of the transverse magnetic field magnitude are also plotted in Fig. 4.5(e). An x component of magnetic field is induced as the flow changes direction on the wedge.

The exact solution to the oblique shock problem can be found by solving the Rankine-Hugoniot jump conditions across the shock along its normal (n) and tangential (t) directions. The equations are shown in Eq. 4.2 where [ ] denotes the jump between the left (state 1) and right (state 2) states.

$$\begin{aligned}
[\rho V_n] &= 0 \\
\left[\rho V_n^2 + P + \frac{B_t^2}{2\mu_0}\right] &= 0 \\
\left[\rho V_n V_t - \frac{B_n B_t}{\mu_0}\right] &= 0 \\
[B_n] &= 0 \\
[V_n B_t - V_t B_n] &= 0 \\
\left[\frac{1}{2}\rho V^2 V_n + \frac{\gamma P}{\gamma - 1} V_n + \frac{B_t(V_n B_t - V_t B_n)}{\mu_0}\right] &= 0
\end{aligned} \tag{4.2}$$

Additional constraints need to be applied on the normal and tangential components of velocity and magnetic field along with Eq. 4.2 due to the unknown shock angle α. The flow is assumed to be aligned along the wedge on the downstream side. Eq. 4.3 enlists the additional constraints to solve the oblique shock problem where θ denotes the wedge angle.

$$
\begin{aligned}
B_{n1} &= -B_1\ cos\alpha \\
B_{t1} &= B_1\ sin\alpha \\
V_{n1} &= V_1\ sin\alpha \\
V_{t1} &= V_1\ cos\alpha \\
V_{n2} &= V_2\ sin(\alpha - \theta) \\
V_{t2} &= V_2\ cos(\alpha - \theta)
\end{aligned} \tag{4.3}
$$

The analytic solution to the coupled set of equations 4.2 and 4.3 are difficult to obtain. Hence, Newton-Raphson method is used to solve these equations. The final solution is as shown in Eq. 4.4. This solution can be easily verified by substituting back into the Eq. 4.2 and 4.3.

$$
\begin{aligned}
\frac{\rho_2}{\rho_1} &= 2.73 \\
\frac{P_2}{P_1} &= 4.87 \\
\frac{V_2}{V_1} &= 0.69 \\
\frac{B_{t2}}{B_{t1}} &= 2.83 \\
\alpha &= 48.1^o
\end{aligned} \tag{4.4}
$$

Figure 4.6(a) shows the convergence histories of the implicit LU-SGS scheme as well as Euler explicit time stepping method for the above MHD oblique shock problem. A CFL number of 1 was used for the explicit scheme

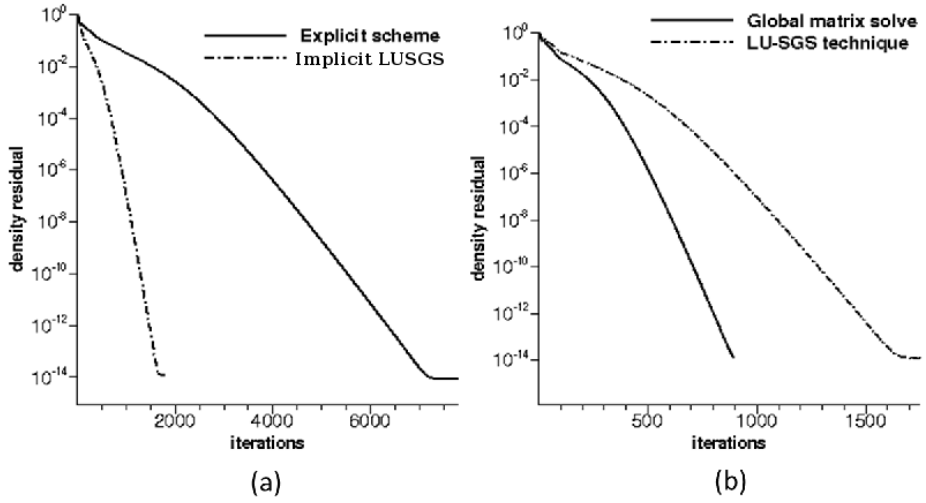

Figure 4.6: (a) Convergence history of explicit and implicit methods and (b) convergence history of global matrix solve using GMRES and LU-SGS technique for the MHD oblique shock problem.

while it was set to 1000 for the implicit LU-SGS scheme. A relative error tolerance of 10^{-14} in the mass density residual is achieved in about 1700 iterations for the implicit scheme using LU-SGS method while the explicit scheme converges about four times slower. The wall clock time for the simulation using the implicit LUSGS scheme was about one minute while the explicit scheme took about two minutes. The time per iteration for the explicit scheme is about 60% lower compared to the LU-SGS scheme. The computational cost associated with the implicit scheme developed is thus comparable to a multistage explicit scheme such as a fourth- order Runge Kutta method. Figure 4.6(b) shows the comparison of convergence between the global matrix solve technique using GMRES with block Jacobi pre-conditioning and the LU- SGS technique. It is seen that the convergence rate of the LU-SGS technique is

slower than the global matrix solve. However, the wall clock time associated with the global matrix solve is about 7.5 minutes compared to about 1 minute using the LU-SGS technique.

4.3 Hartmann flow problem

To test the non-ideal MHD terms and viscous dissipation terms, the Hartmann flow problem is used as a verification test case. Hartmann flow is essentially the flow of a conducting fluid between two parallel electrodes with a constant applied magnetic field perpendicular to the flow direction. Fig. 4.7(a) shows the geometry and computational mesh used for the two- dimensional planar simulation. The channel is assumed to have a length $l = 10\,cm$ and width $2a = 2\,cm$ and the mesh contains 12,500 rectangular cells. The pressure at the inflow (left boundary) is fixed at 100 kPa while the downstream end is at 92 kPa. The variation of pressure in the domain is self consistently computed and is linear at steady state. The coefficient of viscosity is assumed to be a constant value equal to 0.00625 kg/m-s. A constant magnetic field ($B_0\hat{y}$) is imposed by applying a Dirichlet boundary condition with the same value at all boundaries. The simulation is performed using the LU-SGS as well as the global matrix solve technique with a central difference scheme for the convective flux discretization. Note that the flow is of sufficiently low speeds that artificial dissipation is not required to stabilize the hyperbolic flux.

Analytical solution to the problem can be obtained as shown in ref. [124], which depends on the Hartmann number (Ha) of the flow, given by Eqs. 4.5 and 4.6. Hartmann number is a quantity similar to the flow Reynolds

number. It is essentially the ratio of the magnetic Lorentz force to the viscous forces.

$$Ha = \left(\frac{\sigma B_0^2 a^2}{\mu} \right)^{\frac{1}{2}} \tag{4.5}$$

$$\frac{u}{\bar{u}} = H_a \left(\frac{cosh H_a - cosh \frac{H_a y}{a}}{H_a cosh H_a - sinh H_a} \right) \tag{4.6}$$

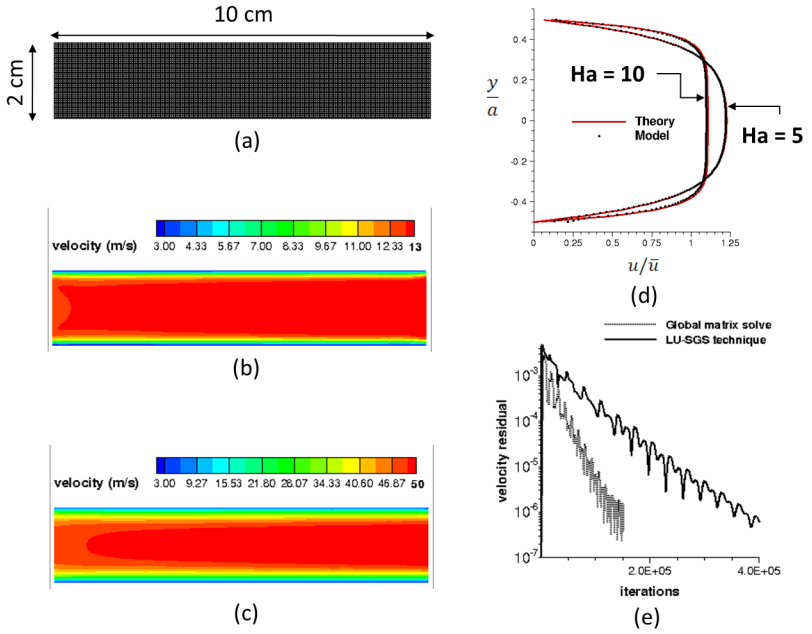

Figure 4.7: (a) Geometry and computational mesh used for the Hartmann flow test case, (b) Velocity profile for Hartmann number Ha=10, (c) Velocity profile for Hartmann number Ha = 5, (d) Comparison of velocity profile at x = 5 cm with theory. (e) Steady state convergence histories for the LU-SGS and global matrix solve techniques.

Here $\bar{u}$ represents the average velocity, μ is the coefficient of viscosity

and σ is the electrical conductivity of the fluid. Figure 4.7(b) and (c) show the axial velocity for two different Hartmann numbers. The magnetic field is assumed to be 0.125 tesla for case (b) and is halved for case (c). The solution obtained from the model agrees well with theoretical solution shown in Fig. 4.7(d). Fig. 4.7(e) shows the steady state convergence of the velocity residual using both the implicit matrix solve techniques for the Hartmann flow test case. It is again observed that the global matrix solve method using GMRES converges in about 150,000 iterations, about half the number iterations using the LU-SGS technique. The number of iterations to steady state are much higher compared to the oblique shock problem because of the increased stiffness of compressible governing equations while solving an incompressible low speed flow. The wall clock time taken for the global matrix solve was around 190 minutes while the LU-SGS technique took about 120 minutes despite the larger number of iterations. The simulations were performed in parallel using 48 processors.

4.4 Parallel performance

Here we use the two-dimensional MHD shock tube problem described in section 4.1 to study the scalability and performance of the LU-SGS and the global matrix solve implicit schemes. A finer version of the mesh shown in figure 4.2 with 33000 triangular elements is used here for performance studies. The global matrix assembly and solve are done using the Krylov Subspace (KSP) subroutines in PETSc libraries. The KSP solver used is GMRES with block Jacobi preconditioning. Figure 11 shows timing and scalability informa-

tion for both the techniques on a maximum of 48 cores.

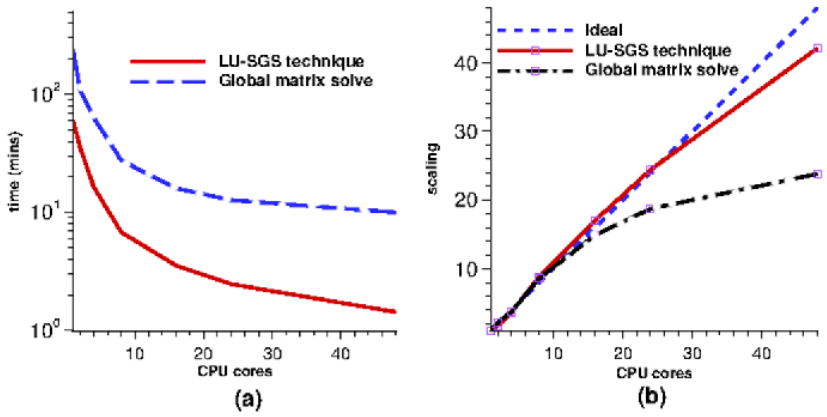

Figure 4.8: Parallel performance (a) time in minutes vs number of CPU cores and (b) strong scaling curve.

The run times show that the LU-SGS scheme is more efficient compared to the global matrix solve. The strong scaling curve for the LU-SGS technique shown in Fig. 4.8(b) reveals that the communication and partition boundary calculations start degrading performance around 48 cores. Performance of the LU-SGS technique can be enhanced by an optimal coloring strategy. Sub-optimal coloring leads to certain colors being far more dominant compared to the others. This creates a situation where processors communicate very little or no data, leading to inefficient use of memory bandwidth and increased latency. The global matrix solve technique scales well until 24 cores and takes about four times longer than the LU-SGS solve for the serial run. It takes only 1.5 minutes for the entire run for the LU-SGS technique with 48 cores while it takes about 10 minutes for the same problem with the global matrix method.

Chapter 5

Plasma deflagration in coaxial plasma accelerators

5.1 Introduction

Acceleration of a plasma using electromagnetic Lorentz forces has been extensively used in space propulsion devices such as pulsed plasma thrusters (PPT) [26], magneto-plasmadynamic thrusters [10] (MPDT) and also in devices such as dense plasma focus (DPS) [8] which is used as a neutron source for nuclear fusion applications. Pulsed coaxial plasma accelerators are a subset of electromagnetic accelerators which are comparatively more efficient than their parallel-plate counterparts with regard to reduced magnetic flux leakage and current sheet distortion. They have been employed in several applications such as space propulsion [10], dense plasma focus devices and in materials processing [96]. Experimental studies on co-axial plasma accelerators [2, 125–127] have revealed two modes of operation based on the delay between gas loading and discharge ignition. It has been observed that larger delay led to the plasma detonation or snowplow mode where a luminous current sheet propagates from the breech to the muzzle. On the other hand, shorter delay times led to a relatively diffuse, plasma deflagration mode where the input gas is continuously processed and accelerated to high velocities. It was also observed

that the deflagration mode is more efficient in terms of generating higher directed particle energies at the muzzle for lower applied voltages. The physics of the discharge as well as the pinching effects at the muzzle pertaining to this mode of operation has remained relatively unexplored. There are predominantly two different theories associated with the two modes of operation. The magneto-hydrodynamic (MHD) Rankine-Hugoniot theory was first proposed by Cheng [128] to explain the deflagration and detonation phenomenon. In this theory, the discharge is modeled as a rapid energy addition process similar to combustion. The only difference lies in the mechanism of energy addition, which is through electrical energy input for the former case while for the latter case it is through chemical reactions. The Rankine-Hugoniot shock jump conditions for the ideal MHD equations were used here and an analogy of detonation and deflagration phenomenon in combustion physics was used. The other theory is based on plasma resistivity. This was first proposed by Woodall and Len [129] where they concluded that deflagration mode operation happens at lower temperatures $\sim$ 1 eV (higher resistivities) where magnetic field diffusion is dominant. The detonation mode was observed at relatively higher temperatures $\sim 10 - 50$ eV where magnetic field convection is dominant. In a recent study on coaxial plasma accelerators done by Poehlmann et al. [130], the MHD Rankine-Hugoniot theory has been modified with a magnetic field convection fraction which yields better agreement with experimental work. In this paper, we perform a numerical study of the coaxial plasma accelerator and closely look at its operation in low and high resistivity regimes. The plasma in the co-axial plasma accelerator falls under the regime of a thermal plasma

with a high degree of ionization which can be studied using the resistive MHD equations. This study uses the numerical model described in chapters 2, 3 and 4 to study the high density plasma in a coaxial plasma accelerator. The chapter is organized as follows. Section 5.2 describes the modifications that are made to the computational model to perform axi-symmetric calculations. Section 5.3 shows the results regarding the operation of a coaxial plasma accelerator. The device that will be modeled is similar to the experimental work done at Stanford University. The results regarding current measurements in their experiment have been published in ref. [2] which will be compared with our numerical calculation. Simulation results showing the pressure, temperature and velocity transients in the device and a comparison between operation at lower and higher plasma conductivities will be presented in this section.

5.2 Numerical model

The inviscid form of the resistive MHD equations shown in equations 2.23 - 2.26 from chapter 2 are used to model the plasma in the coaxial plasma accelerators. The effects of fluid viscosity and thermal conductivity can be neglected in these devices because the flow Reynolds numbers are sufficiently high.

5.2.1 Axi-symmetric representation

The simulations are performed in two dimensional axi-symmetric coordinate system. The azimuthal momentum equation is neglected in the model. The governing equations are modified to account for terms that arise due to

formulation in cylindrical coordinates. The governing equations and numerical formulation is exactly the same as shown in chapters 2 and 3. The governing equations (Eqs. 2.23 - 2.26), conservative variables (Eq. 3.2), inviscid and diffusive fluxes and source terms (Eqs. 3.3 - 3.5) can be modified assuming the x coordinate is in the axial direction while the radial and azimuthal directions are the y and z coordinates, respectively. The resistive MHD equations can be written in convection diffusion form as shown in Eq. 5.1.

$$\frac{\partial \mathbf{U}}{\partial t} + \vec{\nabla}.\vec{\mathbf{F}}_{inv} = \vec{\nabla}.\vec{\mathbf{F}}_{diff} + \mathbf{S} \tag{5.1}$$

Here $\mathbf{U}$ represents the set of conservative variables in axi-symmetric coordinates as shown in Eq. 5.2. The inviscid flux term $\vec{\mathbf{F}}_{inv}$ is as shown in Eq. 5.3. The diffusive flux consists only of terms due to plasma resistivity η, is shown in Eq. 5.4.

$$\mathbf{U} = \begin{bmatrix} \rho \\ \rho v_r \\ \rho v_z \\ B_r \\ B_\theta \\ B_z \\ \rho Z \end{bmatrix} \tag{5.2}$$

$$\vec{\mathbf{F}}_{inv} = \begin{bmatrix} \rho\vec{V} \\ \rho v_r\vec{V} + P_t\hat{r} - B_r\vec{B} \\ \rho v_z\vec{V} + P_t\hat{z} - B_z\vec{B} \\ B_r\vec{V} - v_r\vec{B} \\ B_\theta\vec{V} \\ B_z\vec{V} - v_z\vec{B} \\ (\rho Z + P_t)\vec{V} - (\vec{V}.\vec{B})\vec{B} \end{bmatrix} \tag{5.3}$$

$$\vec{\mathbf{F}}_{diff} = \begin{bmatrix} 0 \\ 0 \\ 0 \\ \eta\vec{\nabla}B_r \\ \eta\vec{\nabla}B_\theta \\ \eta\vec{\nabla}B_z \\ \eta(\vec{J}\times\vec{B}) \end{bmatrix} \tag{5.4}$$

$$\mathbf{S} = -\begin{bmatrix} 0 \\ 0 \\ 0 \\ (\vec{\nabla}\eta\times\vec{J}).\hat{r} \\ (\vec{\nabla}\eta\times\vec{J}).\hat{\theta} \\ (\vec{\nabla}\eta\times\vec{J}).\hat{z} \\ 0 \end{bmatrix} - \left(\vec{\nabla}.\vec{B}\right)\begin{bmatrix} 0 \\ B_r \\ B_z \\ v_r \\ 0 \\ v_z \\ (\vec{V}.\vec{B}) \end{bmatrix} + \begin{bmatrix} 0 \\ 0 \\ P_t r^{-1} \\ 0 \\ -\eta B_r r^{-2} \\ -\eta B_\theta r^{-2} \\ 0 \end{bmatrix} \tag{5.5}$$

The divergence and Laplacian terms present in Eq. 5.1 should be represented in cylindrical coordinates. This results in additional axi-symmetric

source terms as shown by the third term in Eq. 5.5. The radial momentum equation has a source term associated with vector divergence of pressure tensor in cylindrical coordinates. The r and θ direction magnetic field equations have source terms associated with Laplacian of a vector that come from the diffusion terms in the magnetic field equations. The current density $\vec{J}$, obtained from the curl of magnetic field can be written in axi-symmetric coordinate system as shown in Eq. 5.6.

$$J_r = \left(\frac{1}{r}\frac{\partial B_z}{\partial \theta} - \frac{\partial B_\theta}{\partial z}\right)$$

$$J_\theta = \left(\frac{\partial B_r}{\partial z} - \frac{\partial B_z}{\partial r}\right)$$

$$J_z = \left(\frac{\partial B_\theta}{\partial r} + \frac{B_\theta}{r} - \frac{1}{r}\frac{\partial B_r}{\partial \theta}\right) \tag{5.6}$$

5.3 Results

The coaxial plasma accelerator that is modeled here correspond to the experiments performed at Stanford Plasma Physics Lab. Following is a brief description of the experiments which was published in ref. [2].

5.3.1 Description of experiments

Figure 5.1(a) shows the geometry of the coaxial plasma accelerator that was used in the experiments. The length of the accelerator was 23 cm and the diameter of the outer electrode was 5 cm. The diameter of the inner electrode

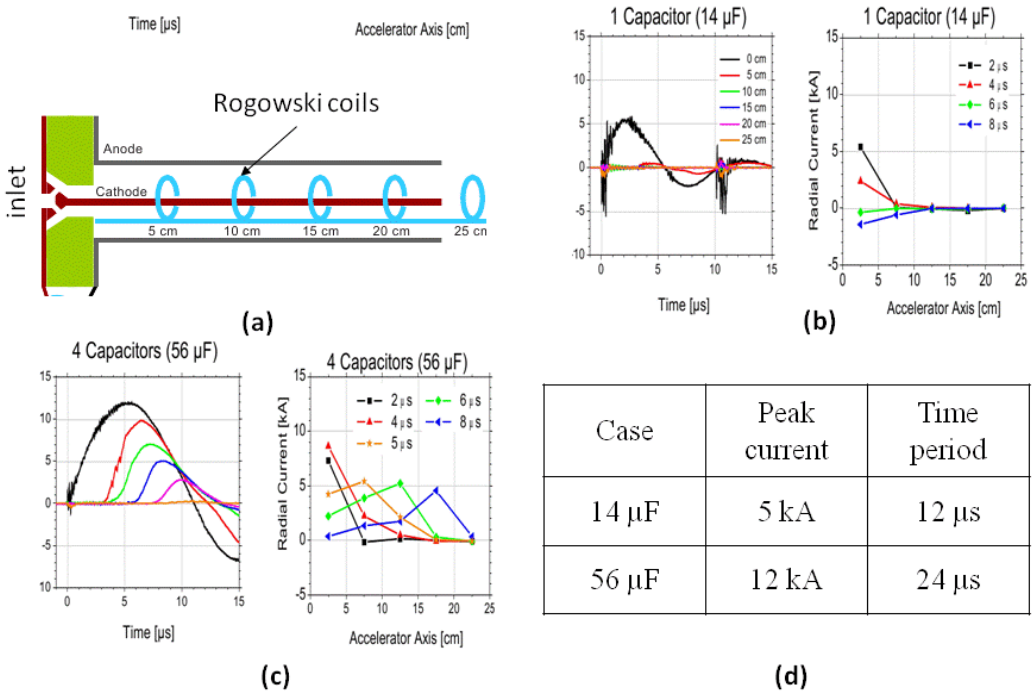

Case	Peak current	Time period
14 μF	5 kA	12 μs
56 μF	12 kA	24 μs

Figure 5.1: (a) geometry of the coaxial plasma accelerator (b) radial current measurements along axis for operation with 14 μF bank capacitance (c) radial current measurements along axis for operation with 56 μF bank capacitance (d) Table listing the peak currents and pulse time periods for cases (b) and (c). The figures were obtained from ref. [2]

was 5 mm. The inlet is a fast acting gas valve which puffs in hydrogen gas immediately after which the discharge is ignited. The inside of the accelerator was at near vacuum conditions before it was operated. The experimental setup also had Rogowski coils placed at 5 cm intervals along the axis. These coils measured the total axial current passing through the cathode at that point which is the total integrated radial current from the plasma upstream of the coil. The currents measured by each of the coils are shown in figure 5.1(b) and (c) for two different power settings. The difference between the currents measured by any two adjacent coils gives the integrated current between the coils. The piecewise integrated currents are also plotted in figures 5.1 (b) and (c) along the axis at different times in the current waveform. The power input for the case shown in figure 5.1(c) is higher due to larger bank capacitance. The time periods also scale as $\sqrt{C}$ (C is the capacitance) resulting in larger time periods for the higher power setting. The peak currents also increase with increasing power. The values for the time period and peak currents are summarized in figure 5.1 (d). One of the important observations from the radial current measurements is regarding the extent over which the current density is spread out. For the lower power setting, the current is concentrated close to the inlet end while it spreads out with current sheet like features for the higher power setting. We make the following hypothesis pertaining to these observations: The plasma must be of lower conductivity for the lower power case compared to the higher power case. The current sheet like features seen in the latter must be due to a transition to the higher conductivity mode which is a characteristic of the detonation mode.

Boundary	Boundary condition	Parameters specified
inlet	Inflow	P, T, $\vec{B}(r,t)$
anode	Perfect electric conductor (PEC)	$B_n = 0$
cathode	Perfect electric conductor (PEC)	$B_n = 0$
exit	Outflow	P

Table 5.1: Conditions at the four boundaries indicated in figure 5.2

5.3.2 Simulation parameters and conditions

We perform two dimensional axi-symmetric simulations of the coaxial plasma accelerator shown in figure 5.1. The boundaries are indicated in figure 5.2.

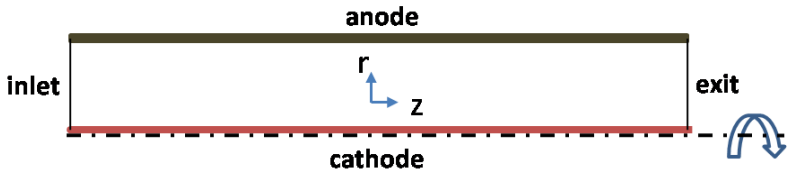

Figure 5.2: Two dimensional axi-symmetric domain of the coaxial plasma accelerator

Table 5.1 shows the boundary conditions and the parameters specified at each of them. An inflow boundary condition is assumed at the inlet where the pressure (P), temperature (T) and a Dirichlet condition for the magnetic field is specified. The flow is assumed to be at a stagnation pressure of 1 atm. at the inlet which is similar to the operating pressures in the experiments. A sensitivity study based on the inlet pressures is reported in section 5.3.5.

Case	T_{inlet}	Conductivity range	Current input
Low conductivity	1 eV	$\sim 10^3$ - 10^4 S/m	5 kA,83 kHz
High conductivity	10 eV	$\sim 10^4$ - 10^5 S/m	12 kA,42 kHz

Table 5.2: Two different cases that will be studied with varying inlet temperatures

Two different cases will be studied where the temperature at the inlet is varied as shown in Table 5.2. The temperature at the inlet is assumed to be equal to 1 eV which corresponds to the low power setting in the experiments which we hypothesize as the deflagration mode. The conductivities for this case fall in the high resistivity regime for the assumed temperatures where magnetic field diffusion will be dominant. The temperature at the inlet is assumed to be equal to 10 eV corresponding to the high power setting in the experiments where current sheet like features are observed. The conductivities in this case are high enough for magnetic field convection to play a role. The assumed values for the temperatures are consistent with measurements made by Woodall and Len [129], which was a few eVs for the deflagration mode while it was few 10s of eVs for the detonation mode of operation. The current input to the device is a damped sinusoidal pulse as shown in figures 5.1 (b) and (c) which translates to a Dirichlet condition for the azimuthal magnetic field at the inlet as shown below.

$$\frac{\partial B_\theta}{\partial z} = -\mu_0 J_r \tag{5.7}$$

$$rB_\theta = \int_0^z J_r r dz + C \tag{5.8}$$

$$since\ B_\theta(\infty) = 0 \implies rB_\theta(0) = C = \int_0^\infty J_r r dz = \frac{\mu_0 I_{input}}{2\pi} \tag{5.9}$$

This idea was also used by Powell et al. [131] in the study of plasma armatures in electromagnetic accelerators. The one dimensional version of Ampere's law is used as shown in Eq. 5.7 which is integrated along the axial coordinates. Supposing that the azimuthal field vanishes at infinity, the constant of integration in Eq. 5.8 can be found out in terms of the input current (I_{input}). The expression for the azimuthal magnetic field at the inlet is shown in Eq. 5.9. The other two components are assumed to be zero at the inlet.

The anode and cathode are assumed be perfect electric conducting boundaries where the normal component of magnetic field goes to zero. A near vacuum pressure $\sim$ 10 Pa is used as initial condition in the domain and at at the exit plane, consistent with the experiments. Spitzer formulation [132] is used to obtain conductivity as a function of temperature. Real gas effects are accounted for by using tabulated energy and gas constant data for hydrogen obtained from ref. [1]. The computational mesh used consists of 20,000 cells with 100 along the radial direction and 200 along the axial direction.

5.3.3 Simulation results

A time accurate calculation is done using the pseudo-time stepping algorithm for both the cases shown in table 5.2. Figure 5.3 shows the axial ve-

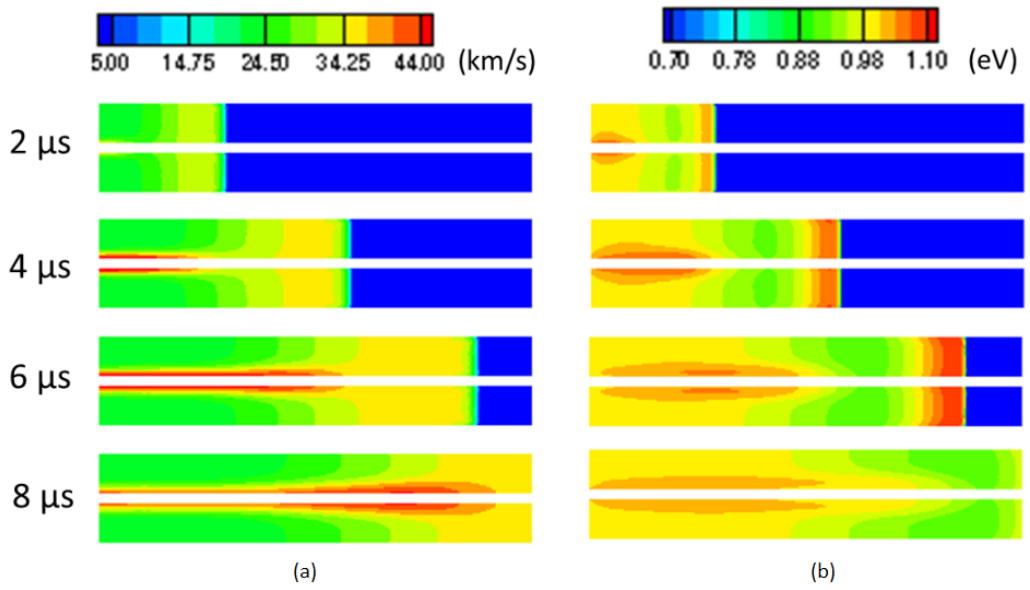

Figure 5.3: (a) Axial velocity and (b) temperature transients for the low conductivity case

locity and temperature transients for the low conductivity case at four different instances in the current waveform. The axial velocities are seen to be higher close to the axis due to stronger magnetic fields at smaller radii. The temperatures are seen to be higher close to the axis due to larger Joule heating brought about high axial currents. The temperatures are also high immediately after the propagating front due to shock heating. Maximum axial velocities $\sim$ 40 km/s is seen close to the axis which translates to Mach number on the order of 5. Figure 5.4 shows the azimuthal magnetic field transients for both the low and the high conductivity cases. Magnetic field diffusion is seen to play a dominant role in the low conductivity case compared to the high conductivity case. The azimuthal field is convected along the accelerator with the bulk fluid

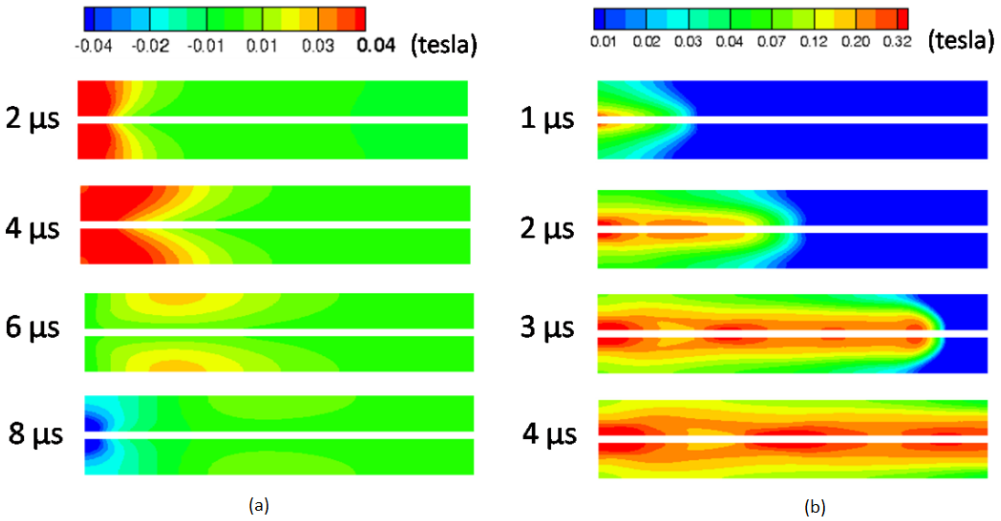

Figure 5.4: Azimuthal magnetic field transients for (a) low conductivity case and (b) high conductivity case. The residence time associated with low conductivity case is smaller compared to the other case. Hence, the times associated with the transient plots are different.

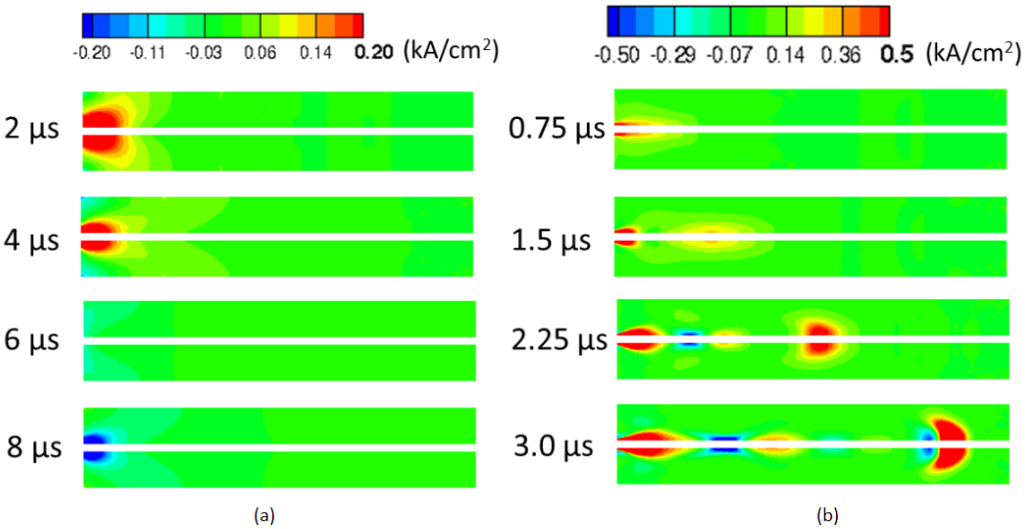

Figure 5.5: Radial current density transients for (a) low conductivity case and (b) high conductivity case.

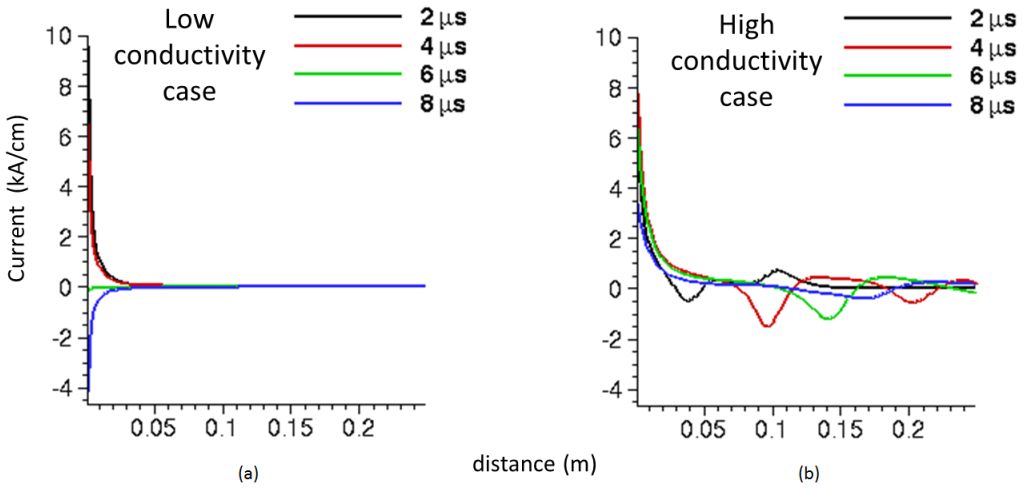

Figure 5.6: Radial current density transients at the cathode along the axial direction for (a) low conductivity case and (b) high conductivity case

velocity for the latter. The convection effects are greater close to the axis again due to larger fluid velocities. The bulk fluid velocities are higher for the high conductivity case and hence the fluid residence time associated with this case is smaller compared to the low conductivity case. The azimuthal fields are higher in figure 5.4(b) due to the higher peak currents used for this case (Table 5.2). Figure 5.5 shows the variation of radial current densities for the two cases. The radial currents are essentially the axial gradients of the azimuthal magnetic fields. The current densities are seen to be high close to the inlet end for the low conductivity case. This is typically seen in the deflagration mode of operation. Propagating current sheet like features are observed for the high conductivity case which is generally seen in the detonation mode. The regions of negative current densities are like localized current loops formed

due to the transient nature of the current input. Plasma conductivity thus plays an important role in determining the mode of operation as theorized by Woodall and Len [129] from their experiments. The axial variation of radial current density at the cathode is plotted in Figure 5.6 for both the cases. It is again seen that the current densities are more or less confined close to the inlet end for the low conductivity case while the axial extent is larger for the high conductivity case. Current sheet like features are also observed in the high conductivity case, similar to what will be seen in the detonation mode of operation. Figure 5.7 shows the comparison of experimental radial current measurements for the two cases with what is obtained from the simulations. The plots show the piecewise integrated currents between intervals 0-5, 5-10, 10-15 cm and so on. There is very good agreement between the simulated current distribution and the experiments for the low conductivity case where the current densities are concentrated close to the inlet end of the accelerator. The simulated current densities do not compare very well for the high conductivity case which we hypothesized as the detonation mode of operation. One of the reasons for the mismatch is due to the over-predicted conductivity used in the simulations which led to a much lower fluid residence time compared to the experiments. The formation of localized current loops at higher power settings have also been confirmed in the experiments [133].

5.3.4 Simulations with exit plume

In order to study the parameters at the exit of the accelerator an extended computational domain is used in the two dimensional axi-symmetric

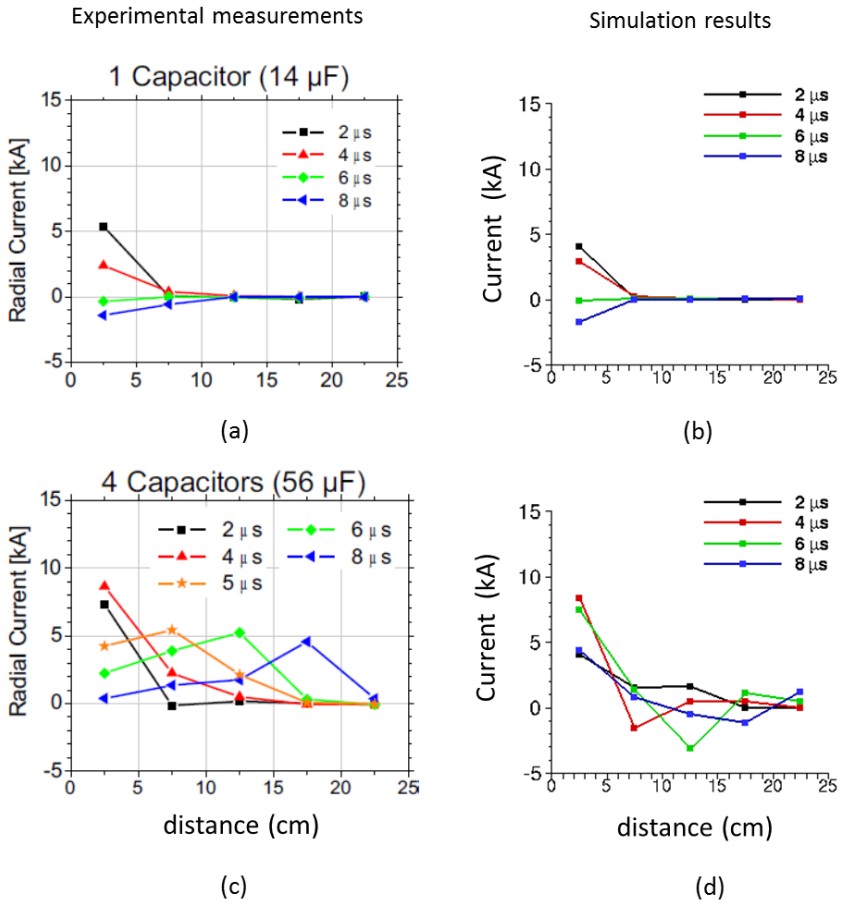

Figure 5.7: Comparision of axial distribution of integrated radial currents at the cathode from experiments, (a) and (c), and from simulations, (b) and (d), for the low and high conductivity cases respectively

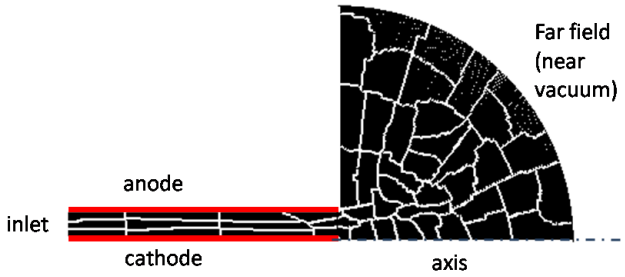

Figure 5.8: computational mesh for simulations with exit plume done on 48 processors. The white lines indicate partition boundaries for each processor.

simulations as shown in Figure 5.8. The mesh consists of 87,000 cells and the simulation is performed on 48 processors using the domain partitioning shown in Figure 5.8. The boundary conditions for the inlet, anode and cathode are the same as before. An outflow boundary condition with near vacuum pressure is used at the far-field boundary and zero flux boundary condition is imposed on axis. Figure 5.9 shows the contour plots for temperature, axial velocity, magnetic field and mass densities after 4 μs for the high conductivity case. The plume structure is essentially a strong shock wave that propagates out into the vacuum exit domain. The temperature tends to rise sharply at the exit end of the cathode due to the pinching effects brought about high axial currents. The axial current varies as the reciprocal of radius times the azimuthal magnetic field. Therefore, it is higher close to the axis as shown in figure 5.11(a). Axial velocities $\sim$ 450 km/s are seen at the exit close to the axis which corresponds to directed particle energies $\sim$ 1 keV (figure 5.11(b)) which are consistent with experimental measurements [133]. The azimuthal magnetic field tends to drop at the exit end of the cathode as shown in figure 5.10(a), which corresponds

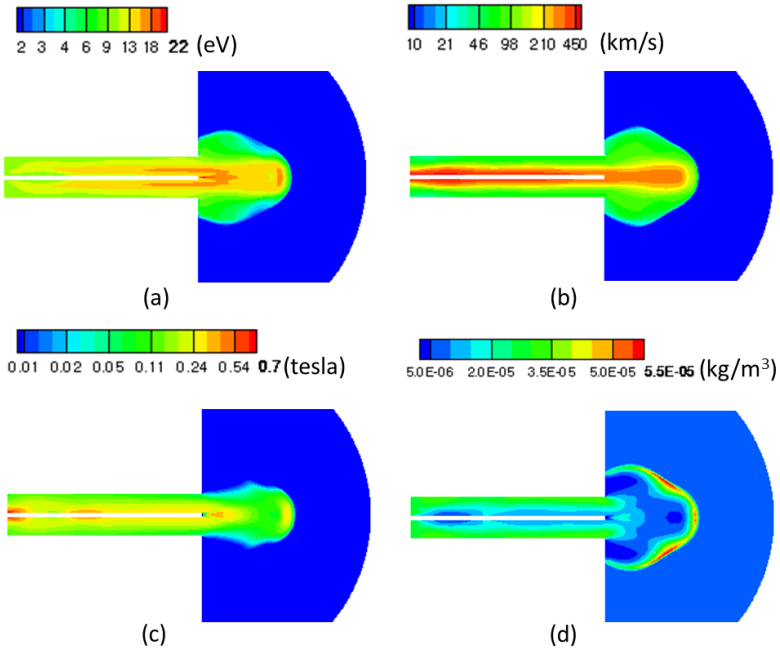

Figure 5.9: a) temperature, (b) axial velocity (c) azimuthal magnetic field and (d) mass density at time t = 4 μs for the high conductivity case.

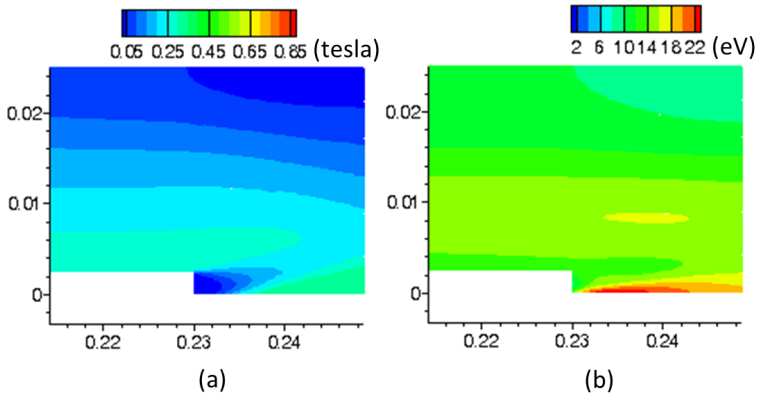

Figure 5.10: Closer view of (a) azimuthal magnetic field and (b) temperature distribution near the exit end of the inner electrode at time t = 4 μs for the high conductivity case.

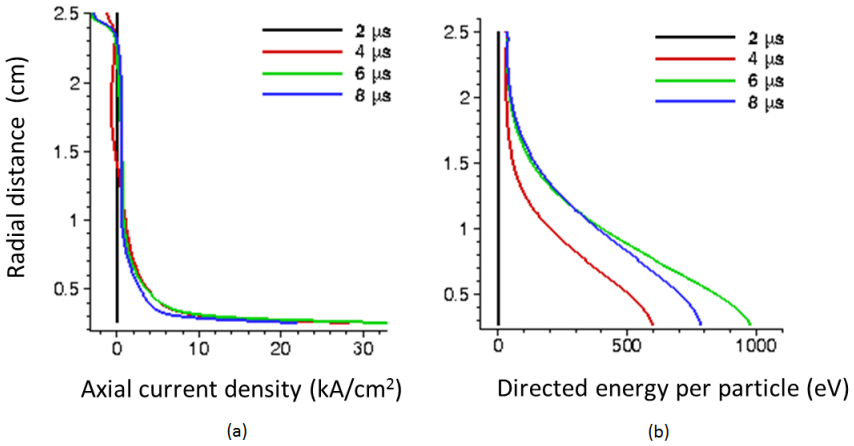

Figure 5.11: (a) Axial current density and (b) directed particle energy at the exit plane plotted against distance along radial direction.

to the pinching effect where the energy in the magnetic field is converted to thermal energy (figure 5.10(b)). The density contours show a region of high density that is formed after the shock which decays to low values when the temperature in the region rises. Such propagating regions of high density also arise in the solution of a Sedov-Taylor blast wave. The densities tend to drop on axis at the cathode end due to the higher temperatures brought about by pinching effects.

5.3.5 Inlet pressure sensitivity study

The inlet pressure assumed for the base line cases is 52 kPa which corresponds to choked flow of hydrogen gas at 1 atm. stagnation pressure. The experiments do not explicitly quote a value of pressure at the inlet but mention the integrated mass bit that is processed over the input current waveform. Figure 5.12 (a) shows the variation of the integrated mass bit size over a cycle of

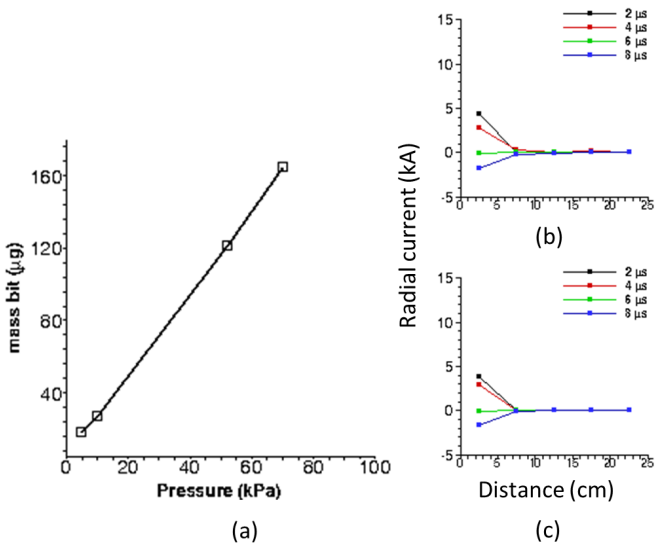

Figure 5.12: (a) variation of integrated mass bit size with inlet pressure, piecewise integrated radial current distribution for inlet pressure (b) 4.8 kPa and (c) 52 kPa

input current waveform for the low power case for varying inlet pressures. The temperature at the inlet is assumed to be the same (1 eV) for all the cases. The mass bit size is seen to be directly proportional to the inlet stagnation pressure. The piecewise integrated radial current distributions for inlet pressures of 4.8 kPa and 52 kPa are shown in Fig. 5.12 (b) and (c). There is very little difference in the axial distribution of radial currents with the change in inlet pressure. This is because the current waveforms are only sensitive to the plasma conductivity which depends on the plasma temperatures.

5.4 Grid convergence study

A grid convergence study for the high conductivity case shown in table 5.2 is described in this section. All the simulations in this study are performed using a dual time stepping algorithm where sub-iterations are performed for a given physical time step, using an implicit method, with a CFL number of 3. The pseudo-time step in each sub-iteration is calculated as the product of CFL number and the fast plasma wave transit time scale. The physical time step is assumed to be 1 ns for all the simulations. The inviscid flux term is discretized using a first order Lax Friedrich's method. Figures 5.13(a) and (b) show the

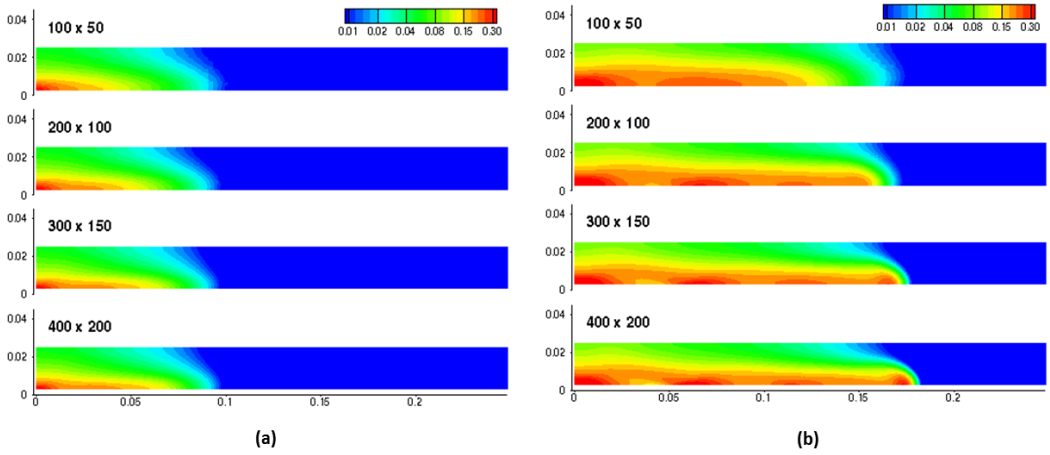

Figure 5.13: Azimuthal magnetic field solution at (a) 1.5 μs and (b) 2.5 μs for simulations done using four different grids

azimuthal magnetic field solution at time $t = 1.5\ \mu s$ and $t = 2.5\ \mu s$ for four different meshes, respectively. The azimuthal magnetic field distribution is seen to approach a converged solution with grid refinement. The refined grids (300 x 150 and 500 x 250) in figure 5.13(b) are able to capture more features

with less amount of dissipation. There is a slight error in the location of the front in Figure 5.13 (b) because of errors in temporal discretization. The pseudo-time step, which is proportional to the ratio of grid size to fast plasma wave speed, reduces with grid refinement. Therefore, it is smaller for finer grids due to the constant CFL number used in all the simulations.

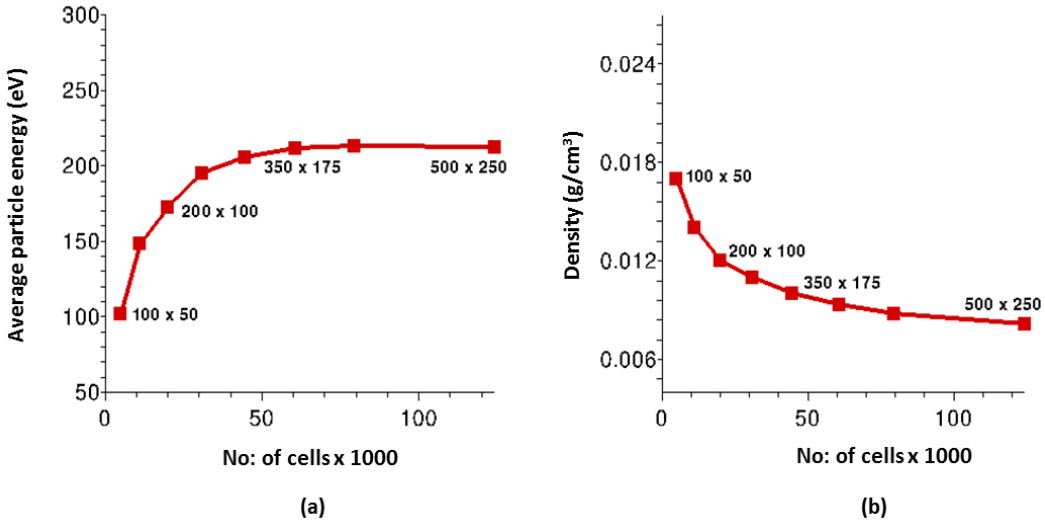

Figure 5.14: (a) Average particle energy and (b) density at the inner electrode at axial location $x = 0.125$ and time $t = 3\ \mu s$ plotted for varying number of mesh elements

Figure 5.14 shows the variation of an integrated quantity (average particle energy) and a point-wise quantity (density at inner electrode) with varying grid sizes. The values are seen to stabilize to a constant value with larger number of mesh elements thus confirming grid convergence.

Chapter 6

Modeling of magneto-hydrodynamic flow actuator (RailPAc)

6.1 Introduction

Fluid flow actuation has been a topic of research in recent years which involve problems like delaying boundary layer separation [134–138], supersonic and hypersonic flow control [16, 139–141] as well as the control of aircraft jet noise [142–144]. The use of plasmas in flow actuation has been proposed as a way of active control for aerodynamics applications and offers several advantages like no movable parts and high bandwidth operation compared to their mechanical counterparts. Non-thermal plasmas have been extensively studied as a means of delaying boundary layer separation [145] as well as in supersonic flow control [140]. Discharges such as Direct Current(DC) discharges [99], Dielectric Barrier Discharges (DBD)[134] and nanosecond pulsed discharges [139] have been proposed for these applications. For instance, DBDs in the asymmetric configuration [137] have been used for delaying boundary layer separation for low speed flows $\sim$ few m/s over airfoils. Nano-second pulsed discharges [139] have also been used in the control of shock stand off distance for hypersonic blunt body flows. These devices are typically non equilibrium weakly ionized plasmas and rely on the electro-hydrodynamic (EHD) force or

thermalization of energetic ions (gas heating) to provide actuation. The EHD force depends on the charge imbalance and electric field which is dominant only in the plasma sheath. The sheaths have dimensions on the order of a few Debye lengths (0.01 to 0.1 mm for typical atmospheric pressure glow discharges) which tend to be a very small region close to the electrode surface. The actuation is thus restricted to a small volume. Another approach would be to use a highly conducting and constricted thermal arc plasma and rely on the magnetic Lorentz force to deliver the momentum surplus to the bulk flow. The idea of using the magnetic Lorentz forces have been used in flow actuation studies for shock boundary layer interaction as well as in boundary layer separation control [20–25]. These devices studied by Kalra et al. [24, 25] require a strong applied magnetic field $\sim$ 3-4 tesla to drive the actuation. This is accomplished through solenoidal coils that is situated outside the flow/discharge. A device that uses the induced magnetic fields generated by plasma currents that we call the RailPAc (Rail Plasma Actuator) has been constructed by our research group and is being investigated experimentally. The device consists of two parallel rail electrodes in the stream-wise flow direction across which a thermal plasma is ignited. The self-induced magnetic field due to the current flow, results in large J B Lorentz forces acting on the arc which in turn can be used to deliver momentum to the bulk flow. The RailPAc is a magneto-hydrodynamic plasma actuator that has the same principle of operation as a space propulsion device described in chapter 5. A magneto-hydrodynamics modeling study of the RailPAc device is presented in this chapter. The physical phenomena in its operation and its effectiveness

for atmospheric pressure aerodynamic flow actuation is characterized. A device that is similar in construction to the RailPAc has also been developed for combustion and fuel reforming applications [146, 147] which is referred to as a gliding arc discharge. It is operated at relatively lower power settings compared to the RailPAc. Fridman et al. [146] also studied the nature of the discharge which tends to be an equilibrium plasma in the initial stages and becomes a non-equilibrium plasma in the later stages thus aiding in the formation of reactive free radicals.

6.2 Numerical model

The resistive MHD equations shown in Eqs. 2.23 - 2.26 from chapter 2 is used to model the discharge in the RailPAc device. Note that these equations only account for the induced magnetic fields which are a consequence of the motion of the plasma. The induced fields tend to be dominant in high conductivity plasma flows but at lower conductivities, the applied electric and magnetic fields have to be incorporated into the model. The plasma in the RailPAc is strongly affected by the applied voltage between the rails as well as the magnetic fields brought about by the current through the rails. The modification to the governing equations is as follows.

We can write the total magnetic field B_T as shown in Eq. 6.1

$$\vec{B}_T = \vec{B}_{in} + \vec{B}_{app} + \vec{B}_{es} \tag{6.1}$$

Here $\vec{B}_{in}$ represents the induced magnetic fields resulting from the mo-

tion of the plasma, $\vec{B}_{app}$ represents the externally applied magnetic field and $\vec{B}_{es}$ represents the magnetic fields brought about by the applied electric fields in the system. The applied magnetic field is assumed to satisfy the conditions as shown in Eq. 6.2.

$$\vec{\nabla}.\vec{B}_{app} = 0 \quad \vec{\nabla} \times \vec{B}_{app} = 0 \tag{6.2}$$

The total electric field $\vec{E}_T$ is also the sum of the induced electric fields and the electrostatic fields due to applied voltages in the system as shown in Eq. 6.3. The applied electric field $\vec{E}_{app} = -\vec{\nabla}\phi$, is obtained from current continuity equation shown in Eq. 6.4 where ϕ is the electrostatic potential.

$$\vec{E}_T = \vec{E}_{in} + \vec{E}_{app} \tag{6.3}$$

$$\vec{\nabla}.(-\sigma\vec{\nabla}\phi) = 0 \tag{6.4}$$

Ohm's law can be written in terms of the applied and induced fields as shown in Eq. 6.5.

$$\begin{aligned} \vec{J}_T &= \sigma\left(\vec{E}_T + \vec{V} \times \vec{B}_T\right) \\ \vec{J}_T &= \sigma\left(\vec{E}_{in} + \vec{V} \times \vec{B}_{in}\right) + \sigma\vec{V} \times \vec{B}_{app} + \sigma\vec{E}_{app} \\ \vec{J}_T &= \vec{J}_{in} + \vec{J}_0 + \vec{J}_{es} \end{aligned} \tag{6.5}$$

$\vec{J}_{in}$ denotes the currents brought about by the induced fields. $\vec{J}_0$ is the currents due to the applied magnetic field and the motion of the plasma. $\vec{J}_{es}$ is the current in the plasma brought about by electrostatic fields. The electrostatic currents $\vec{J}_{es}$ also produces a relatively weak magnetic field $\vec{B}_{es}$ which is typically neglected in arc discharges. The thermal effects due to these currents are more important compared to the pinching effects. The Ampere's law for $\vec{B}_{es}$ can be written as shown in Eq. 6.6 which can be solved using magnetic vector potential formulation with the Coulomb gauge ($\vec{\nabla}.\vec{A} = 0$).

$$\begin{aligned} \vec{\nabla} \times \vec{B}_{es} &= \mu_0 \vec{J}_{es} \\ \vec{B}_{es} &= \vec{\nabla} \times \vec{A}_{es} \\ \vec{\nabla} \times (\vec{\nabla} \times \vec{A}_{es}) &= \nabla(\vec{\nabla}.\vec{A}_{es}) - \nabla^2 \vec{A}_{es} \\ \nabla^2 \vec{A}_{es} &= -\mu_0 \vec{J}_{es} \end{aligned} \tag{6.6}$$

The conservation equation for the induced magnetic field can be derived by modifying the Ampere's and Faraday's law using the applied fields. Eq. 6.7 is the modified Ampere's law with the applied magnetic fields. Note that the applied fields are assumed to be curl free. The Faraday's law can be simplified using the current densities obtained from Ampere's law to yield a modified version of the induction equation as shown in Eq. 6.8.

$$\vec{\nabla} \times \vec{B}_T = \mu_0 \vec{J}_T$$

$$\vec{\nabla} \times \left(\vec{B}_{in} + \vec{B}_{app} + \vec{B}_{es} \right) = \mu_0 \left(\vec{J}_{in} + \vec{J}_0 \right) + \mu_0 \vec{J}_{es}$$

$$\vec{\nabla} \times \vec{B}_{in} = \mu_0 \left(\vec{J}_{in} + \vec{J}_0 \right) \tag{6.7}$$

$$\vec{\nabla} \times \vec{E}_T = -\frac{\partial \vec{B}_T}{\partial t}$$

$$-\frac{\partial \vec{B}_{in}}{\partial t} - \frac{\partial \vec{B}_{app}}{\partial t} =$$

$$\vec{\nabla} \times \left(\frac{\vec{J}_{in} + \vec{J}_0}{\sigma} - \vec{V} \times \vec{B}_{app} - \vec{V} \times \vec{B}_{in} \right)$$

$$\frac{\partial \vec{B}_{in}}{\partial t} + \vec{\nabla}. \left(\vec{V} \vec{B}_{in} - \vec{B}_{in} \vec{V} \right)$$

$$+\vec{\nabla}. \left(\vec{V} \vec{B}_{app} - \vec{B}_{app} \vec{V} \right) = -\vec{\nabla} \times \left(\frac{\vec{\nabla} \times \vec{B}_{in}}{\mu_0} \right) - \frac{\partial \vec{B}_{app}}{\partial t} \tag{6.8}$$

The Lorentz forcing source term in the fluid momentum equation can be written in terms of the induced and applied fields as shown in Eq. 6.9. Lorentz force terms that involve $\vec{B}_{es}$ are assumed to be small. The pinching effects of the magnetic fields induced by the electrostatic fields are not strong enough at the operating conductivities of the RailPAc.

$$\vec{J_T} \times \vec{B_T} = (\vec{J_{in}} + \vec{J_0} + \vec{J_{es}}) \times (\vec{B_{in}} + \vec{B_{app}} + \vec{B_{es}})$$

$$\vec{J_T} \times \vec{B_T} = \vec{J_{es}} \times \vec{B_T} + (\vec{J_{in}} + \vec{J_0}) \times \vec{B_{in}} + (\vec{J_{in}} + \vec{J_0}) \times \vec{B_{app}} \tag{6.9}$$

Equation 6.9 can be further simplified by using $(\vec{J_{in}} + \vec{J_0}) = \frac{(\vec{\nabla} \times \vec{B_{in}})}{\mu_0}$ from Eq. 6.7. The momentum source term can then be written as shown in Eq. 6.10.

$$\vec{J_T} \times \vec{B_T} = \vec{J_{es}} \times \vec{B_T} + \vec{\nabla}. \left(\vec{B_{in}} \vec{B_{in}} - \frac{|\vec{B_{in}}|^2}{2\mu_0} I \right) + \vec{\nabla}. \left((-\vec{B_{app}}.\vec{B_{in}})I + \vec{B_{app}} \vec{B_{in}} + \vec{B_{in}} \vec{B_{app}} \right) \tag{6.10}$$

The Joule heating source term can also be modified using the applied electric and magnetic fields as shown in equations 6.11 and 6.12. $\vec{J_{es}} = \sigma \vec{E_{app}}$ is substituted here to simplify the contribution of electrostatic fields to the total Joule heating.

$$\vec{J_T}.\vec{E_T} = \left(\vec{J_{in}} + \vec{J_0} + \vec{J_{es}} \right) . \left(\vec{E_{app}} + \vec{E_{in}} \right) \tag{6.11}$$

$$\vec{J_T}.\vec{E_T} = \sigma |\vec{E_{app}}|^2 + \left(\vec{J_0} + \vec{J_{in}} \right) .\vec{E_{app}} + \vec{J_{es}}.\vec{E_{in}} + \left(\vec{J_0} + \vec{J_{in}} \right) .\vec{E_{in}} \tag{6.12}$$

The last term in Eq. 6.12 can be further simplified by using the Ampere's law from Eq. 6.7 for the current density terms and the Ohm's law (Eq. 6.5) for the induced electric field as shown below.

$$\left(\vec{J}_0 + \vec{J}_{in}\right).\vec{E}_{in} = \frac{(\vec{\nabla} \times \vec{B}_{in})}{\mu_0}.\vec{E}_{in}$$

$$\frac{(\vec{\nabla} \times \vec{B}_{in})}{\mu_0}.\vec{E}_{in} = \vec{\nabla}.\left(\frac{\vec{B}_{in} \times \vec{E}_{in}}{\mu_0}\right) + \frac{\vec{B}_{in}}{\mu_0}.\left(\vec{\nabla} \times \vec{E}_{in}\right)$$

$$\vec{E}_{in} = \left(\frac{\vec{J}_{in} + \vec{J}_0}{\sigma} - \vec{V} \times \vec{B}_{in} - \vec{V} \times \vec{B}_{app}\right)$$

$$\vec{\nabla}.\left(\frac{\vec{B}_{in} \times \vec{E}_{in}}{\mu_0}\right) = -\vec{\nabla}.\left(\frac{(\vec{J}_{in} + \vec{J}_0) \times \vec{B}_{in}}{\mu_0 \sigma}\right)$$

$$-\frac{1}{\mu_0}\vec{\nabla}.\left(|\vec{B}_{in}|^2\vec{V} - (\vec{V}.\vec{B}_{in})\vec{B}_{in}\right) - \vec{\nabla}.\left((\vec{B}_{app}.\vec{B}_{in})\vec{V} - (\vec{V}.\vec{B}_{in})\vec{B}_{app}\right)$$

$$\frac{\vec{B}_{in}}{\mu_0}.\left(\vec{\nabla} \times \vec{E}_{in}\right) = -\frac{\vec{B}_{in}}{\mu_0}.\frac{\partial \vec{B}_{in}}{\partial t} - \frac{\vec{B}_{in}}{\mu_0}.\frac{\partial \vec{B}_{app}}{\partial t}$$

$$= -\frac{\partial}{\partial t}\left(\frac{|\vec{B}_{in}|^2}{2\mu_0}\right) - \frac{\vec{B}_{in}}{\mu_0}.\frac{\partial \vec{B}_{app}}{\partial t} \quad (6.13)$$

The modified governing equations accounting for the applied fields can be written as shown in Eq. 6.14.

$$\frac{\partial \mathbf{U}}{\partial t} + \vec{\nabla}.\vec{\mathbf{F}}_{inv} + \vec{\nabla}.\vec{\mathbf{F}}_{app} = \vec{\nabla}.\vec{\mathbf{F}}_{diff} + \mathbf{S} + \mathbf{S}_{app} \quad (6.14)$$

The set of conservative variables in Eq. 6.14 are given in Eq. 6.15. Here $\rho Z = \rho e + \frac{1}{2}\rho|V|^2 + \frac{|\vec{B}_{in}|^2}{2\mu_0}$ where e is the specific internal energy of the plasma.

$$\mathbf{U} = \begin{bmatrix} \rho \\ \rho\vec{V} \\ \vec{B}_{in} \\ \rho Z \end{bmatrix} \tag{6.15}$$

The analytical form of the inviscid flux $\vec{\mathbf{F}}_{inv}$ and $\vec{\mathbf{F}}_{diff}$ remains the same as in Eq. 3.3 except that the magnetic field components are those of induced fields. $\vec{\mathbf{F}}_{app}$ represent the flux terms that arise due to the applied magnetic fields and is as shown below. Note that the applied magnetic fields are also scaled the same way as the induced magnetic fields thereby eliminating the occurrence of magnetic permeability (μ_0) in the equations shown below.

$$\vec{\mathbf{F}}_{app} = \begin{bmatrix} 0 \\ (\vec{B}_{app}.\vec{B}_{in})I - (\vec{B}_{app}\vec{B}_{in} + \vec{B}_{in}\vec{B}_{app}) \\ \vec{B}_{app}\vec{V} - \vec{V}\vec{B}_{app} \\ (\vec{B}_{app}.\vec{B}_{in})\vec{V} - (\vec{V}.\vec{B}_{in})\vec{B}_{app} \end{bmatrix} \tag{6.16}$$

The source term $[S_{app}]$ is as shown in Eq. 6.17.

$$\mathbf{S}_{app} = \begin{bmatrix} 0 \\ \vec{J}_{es} \times \vec{B}_T \\ -\frac{\partial \vec{B}_{app}}{\partial t} \\ \sigma|\vec{E}_{app}|^2 + \left(\vec{J}_0 + \vec{J}_{in}\right).\vec{E}_{app} + \vec{J}_{es}.\vec{E}_{in} - \vec{B}_{in}.\frac{\partial \vec{B}_{app}}{\partial t} \end{bmatrix} \tag{6.17}$$

6.3 Snowplow model

The plasma acceleration process in the RailPAc is similar to that of most Lorentz force based space propulsion devices. The snowplow model has been successfully used in predicting the motion of the current sheet in unsteady electromagnetic acceleration devices such as parallel plate pulsed plasma thrusters [27] over a broad range of operation. The principal idea behind the snowplow model is to use the equation of motion for the current sheet which is accelerated by the magnetic Lorentz forces. The current sheet also entrains the ambient gas in front of it thereby increasing its own mass just like a "snowplow". The equation of motion of the current sheet can be written as shown below.

$$\frac{d(m\dot{x})}{dt} = m\ddot{x} + \dot{m}\dot{x} = h(2d)\int_0^{\delta} j_z B_y dx \tag{6.18}$$

Here m and x denote the mass and position of the current sheet respectively. h and $2d$ represent the extent of the plasma above the rails (along y direction in figure 6.3) and the distance between the rails respectively. The integral on the RHS of Eq. 6.18 represents the Lorentz force acting on the

current sheet whose stream-wise dimension is δ. The following assumptions are made to simplify this term. The out of plane magnetic field B_y is assumed to linearly decrease to zero along the stream-wise direction within the current sheet and the current density $j_z = -\frac{\partial B_y}{\partial x}$ is assumed to be a constant within the current sheet. An analysis similar to the method shown in Eq. 5.7 in section 5.3.2 yields Eq. 6.19.

$$m\ddot{x} + \dot{m}\dot{x} = \frac{1}{2}L_1 I(t)^2$$

$$L_1 = \frac{\mu_0 2d}{h} \tag{6.19}$$

Here L_1 represents the inductance of the RailPAc per unit length and $I(t)$ is the input current waveform. The inductance of the RailPAc increases linearly with the position of the current sheet as it moves along the streamwise direction. This is because of increase in area over which the out of plane magnetic field is present which in turn increases the magnetic flux for the same current input.

The mass of the current sheet increases in time due to entrainment of the ambient gas in front of it. The instantaneous mass of the current sheet can be obtained in terms of the density of the ambient gas (ρ_a) and its position as shown in Eq. 6.20.

$$m(x) = m_0 + \int_0^t \rho_a h(2d)\dot{x}dt = m_0 + \rho_a h(2d)x \tag{6.20}$$

Substituting Eq. 6.20 into Eq. 6.19 a non-linear ordinary differential equation is obtained which can be numerically solved by writing it as two first order equations as shown in Eq. 6.21.

$$(m_0 + 2hd\rho_a x)\ddot{x} + 2hd\rho_a \dot{x}^2 = \frac{1}{2} L_1 I(t)^2$$

$$\dot{x} = u$$

$$\dot{u} = \frac{1}{m_0 + 2hd\rho_a x}\left(\frac{1}{2} L_1 I(t)^2 - 2hd\rho_a \dot{x}^2\right) \tag{6.21}$$

6.3.1 Results

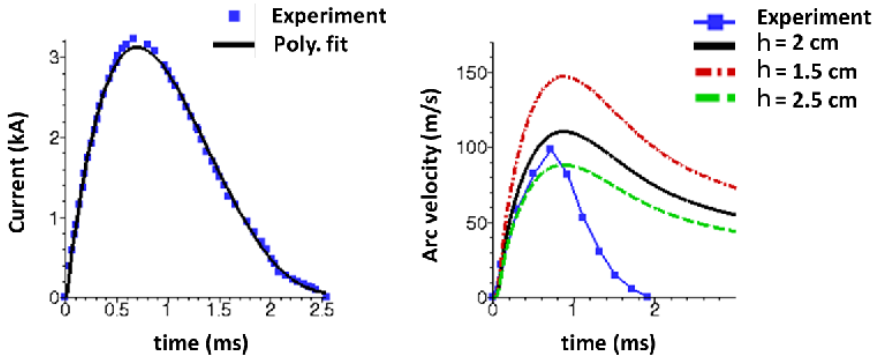

Figure 6.1: (a) Experimental current waveform with approximate polynomial fit used in the model (b) comparison of current sheet propagation speeds with the results of snowplow model

The current waveform from experiments on the RailPAc conducted by our group at UT Austin is as shown in figure 6.1(a). A fourth order polynomial fit is used as input to the snowplow model shown in Eq. 6.21. The other

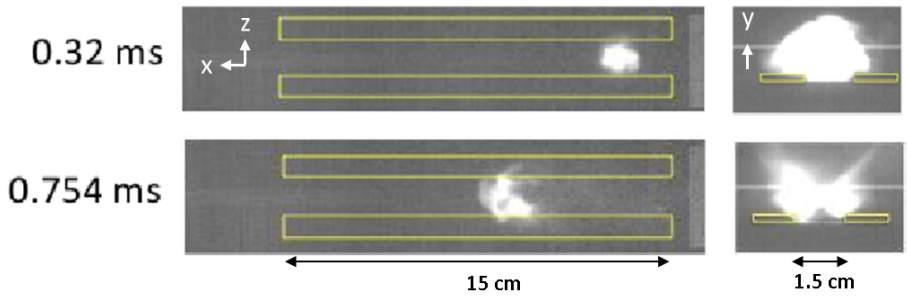

Figure 6.2: Top and side view of transient plasma phenomenon in the RailPAc at two different times obtained from ref. [3]

quantity	value
m_0	0.5 mg
ρ_a	1.16 kg/m^3
2d	1.5 cm
h	2.0 cm

Table 6.1: Values of parameters used in the snowplow model

quantities that are used in the model are shown in Table 6.1.

The value of m_0 used in the model corresponds to the mass of the exploding aluminium fuse wire that is used to initiate the discharge in the RailPAc. The wire is of 0.127 mm in diameter and 15 mm in length. The density ρ_a is assumed to be that of air at standard conditions (1 atm. and 300 K). The height h over which the plasma extends over the bottom surface is assumed to be 2.0 cm for the base case. This is a reasonable assumption from the transients shown in figure 6.2 obtained from ref. [3]. The extent of the plasma along the y direction is approximately 2 cm from the side view.

Figure 6.1(b) shows the comparison of arc velocity measurements from the experiments to that obtained from the snowplow model for 3 different values of h. The velocities predicted by the model are reasonably close to measurements in the first half of the current pulse. The peak velocity increases with lower values of h due to increase in the inductance per unit length resulting in larger Lorentz forcing. The arc velocity from the snowplow model starts dropping in the ramp down phase of the current pulse when the Lorentz forcing reduces. The entrainment of mass in the ramp down phase causes the velocity to reduce due to conservation of momentum. The snowplow model does not compare well with the experiments for the latter half of the current pulse. The drag on the current sheet due to the pressure build up in front of it is not accounted for in the model. The plasma also tends to become non-thermal during this time.

6.4 Two dimensional simulations

6.4.1 Computational domain and boundaries

A schematic depicting our proposed design for the Rail Plasma Actuator (RailPAc) is shown in figure 6.3. The design consists of two rails separated by a distance $2d$ connected to an external circuit that supplies a current, $I(t)$. This problem is inherently three dimensional but for simplicity of computation, the gap between the rails is assumed to be much smaller compared to its stream-wise dimensions and a plane passing midway between the rails is assumed to be the computational domain as shown in figure 6.4(b). The mesh consists of 30,000 quadrilateral elements with decreasing size close to the bot-

tom wall boundary as depicted in the closer view of the inset domain.

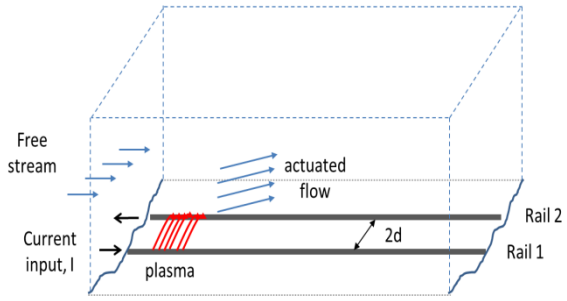

Figure 6.3: Schematic of rail plasma actuator

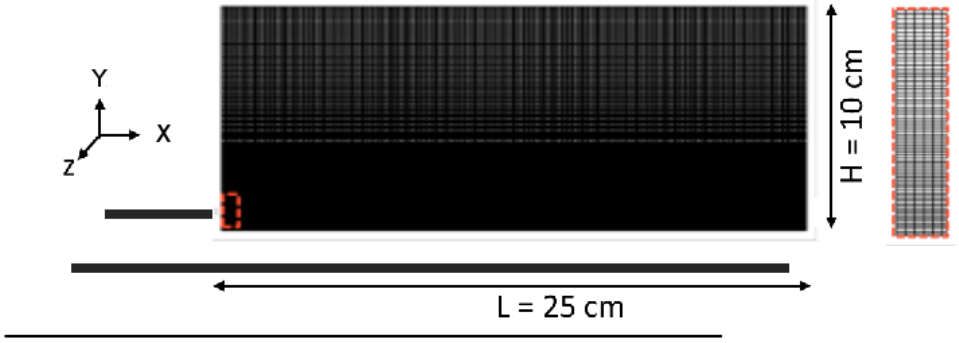

Figure 6.4: Computational domain and mesh

The actuation of the setup is studied under quiescent free stream conditions (free stream velocity is 0) at atmospheric pressure and at room temperature. A time dependent applied magnetic field of the form shown in Eq. 6.22 is assumed.

$$B_y(y) = \frac{\mu_0 I(t)}{\pi}\left(\frac{d}{d^2 + y^2}\right) \tag{6.22}$$

This is obtained using the expression for magnetic field induced by two

infinite current carrying conductors separated by a distance $2d$. The input current waveform (Peak current $\sim$ 3 kA and pulse width $\sim$ 2 ms) from the experiments [3] is used in Eq. 6.22 and the gap between the rails is assumed to be 15 mm. Rail 1 in figure 6.3 is held at a voltage of 150 V. The magnitude of electrostatic field $\vec{E}_{app}$ is assumed to be equal to the voltage divided by the gap distance between the rails. Its direction is along the negative z axis indicated by the current lines shown in figure 6.3. The left, right and top of the computational domain are extrapolated boundaries where the conservative variables from the interior cell are extrapolated onto the face. The bottom is a viscous dielectric wall boundary. A time accurate simulation is performed with the aforementioned initial and boundary conditions for 2 milliseconds.

6.4.2 Non-equilibrium nature of the plasma

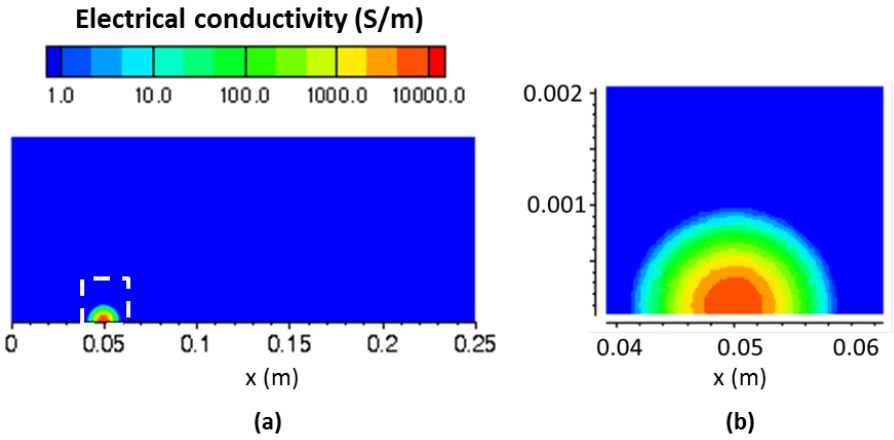

Figure 6.5: (a) Initial conductivity assumed in the domain (b) closer view of initial conductivity profile

Simulations were performed with an initial kernel region of high con-

ductivity as shown in figure 6.5 (a) and (b). A Gaussian distribution of high conductivity is assumed at $x = 5\ cm$ which simulates the breakdown event. This distribution is assumed for a duration of 0.1 ms which essentially is the time over which the voltage across the rail rises sharply in the experiments [3]. This event corresponds to the exploding aluminium wire that initiates the discharge. The peak conductivity is assumed to be 10,000 S/m which is typically seen in rail plasma armatures [131]. A temperature dependent conductivity model is used after the initial breakdown phase of 0.1 ms. The conductivity model is obtained ref. [1] for equilibrium air plasma.

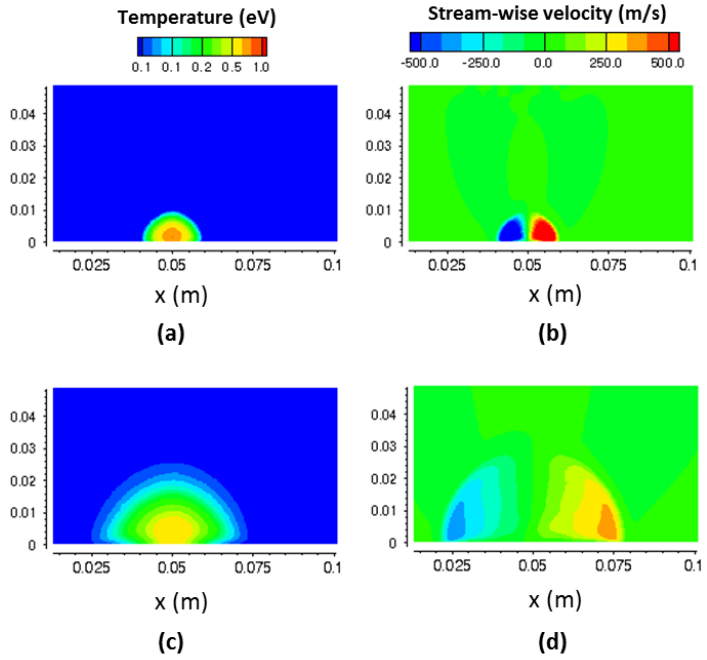

Figure 6.6: (a) Temperature and (b) stream-wise velocity distribution after $t = 0.1\ ms$ (c) Temperature and (d) stream-wise velocity distribution after $t = 0.5\ ms$

Figures 6.6 show temperature and stream-wise velocity in the domain after 0.1 and 0.5 ms respectively. Temperature snapshot shown in figure 6.6 (a) and (c) indicate peak values $\sim$ 0.9 eV is attained. The equilibrium conductivity of air at these temperatures range between 1000 and 4000 S/m which corresponds to energy source terms ($\sigma|\vec{E}_{app}|^2$) on the order of $\sim 10^{12}\ W/m^3$. This rapid energy addition creates a strong blast wave delivering isotropic actuation on the order of 500 m/s as shown in figure 6.6(b) and (d). The region of high conductivity is not seen to propagate in time as opposed to moving current sheet like behaviour seen in experiments. The single fluid MHD model with Local Thermodynamic Equilibrium (LTE) assumption is unable to capture the propagation of current sheet in a self-consistent manner. This could imply non-equilibrium behaviour where the temperature of electrons ($\sim$ 1-2 eV) are much higher than the heavy species due to greater energy coupling with the applied fields. The gas will be heated only by a fraction of the total electrical energy input which is typically about 10-15% [148]. The moving current sheet can be associated with an ionization wave phenomenon which can only be captured by a two temperature non-equilbrium model.

6.4.3 Simulation results

To account for the propagation of current sheet that cannot be captured in a self-consistent fashion with the single fluid MHD model, a propagating kernel of high conductivity is used with speed predicted by the snowplow model. The kernel is a semi-circular Gaussian distribution as shown in figure 6.7 (a) which is initially located at $x = 5\ cm$. The radius over which the conductivity

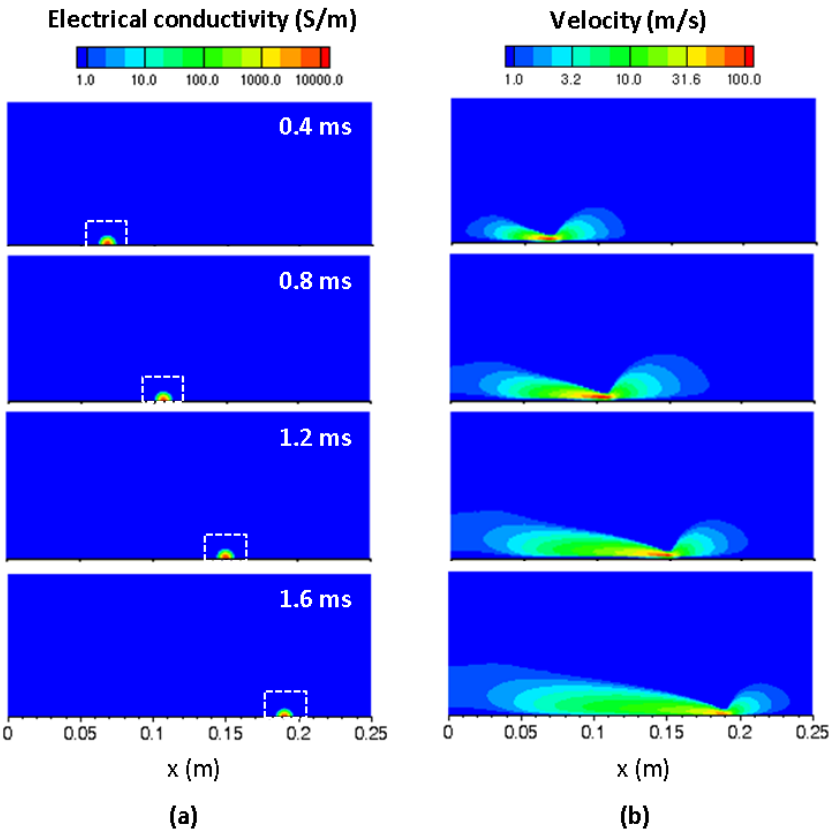

Figure 6.7: (a) Transients of assumed electrical conductivity profiles at 4 instances (b) Stream-wise velocity transients at 4 instances.

is dominant is approximately 5 mm. The peak conductivity is assumed to be 10000 S/m which is typically seen railgun plasma armatures. The heating through electrostatic fields is neglected in the base case simulations. This is done to study the effect of Lorentz forces alone on actuation of the flow. Heating effects are studied in section 6.4.4. The input current waveform from figure 6.1 (a) is used in Eq. 6.22 to evaluate the applied magnetic fields in the domain. Figure 6.7 (b) shows the stream-wise velocity transients at four

different times. Velocities $\sim$ 100 m/s are seen close to the high conductivity region where the Lorentz forces are dominant. The peak values of velocities also correlate with the ramp up and ramp down phase in the current pulse used.

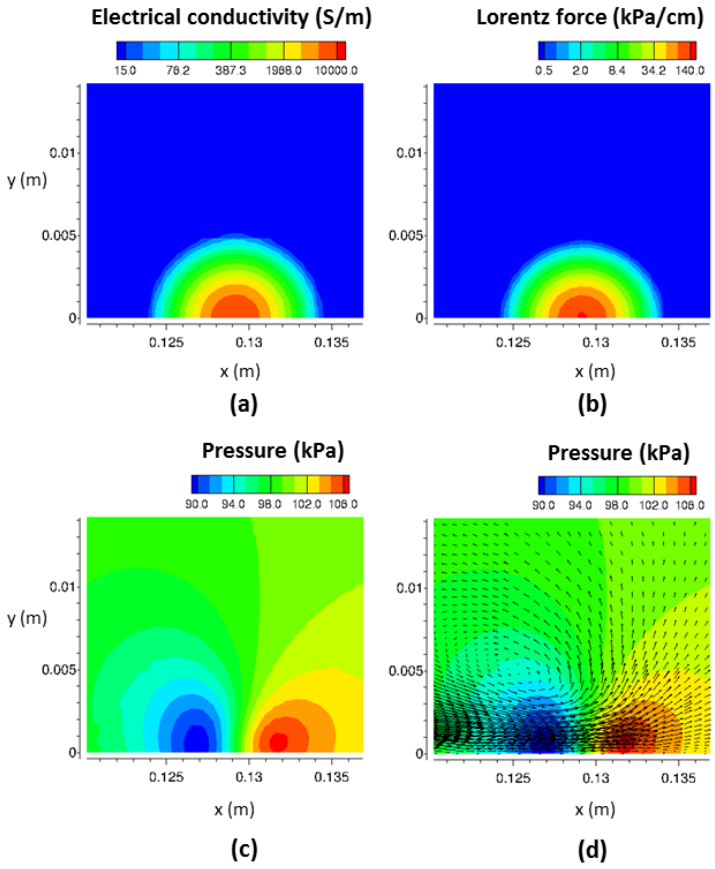

Figure 6.8: (a) electrical conductivity (b) $\vec{J}_{es} \times \vec{B}_{app}$ Lorentz force (c) pressure and (d) velocity vector plot at time t = 1 ms

The mechanism of actuation can be understood from the transients shown in figure 6.8. The Lorentz forcing source term brought about by electrostatic currents ($\vec{J}_{es}$) and applied magnetic fields is dominant in the high

conductivity region as shown in figure 6.8(b). The fluid pressure thus tends to rise in front of the current sheet and a suction region is formed behind it as shown in figure 6.8(c). The formation of the low pressure region forces fluid to accelerate in the rear of the current sheet while the Lorentz forces within actuate the flow in the stream-wise direction.

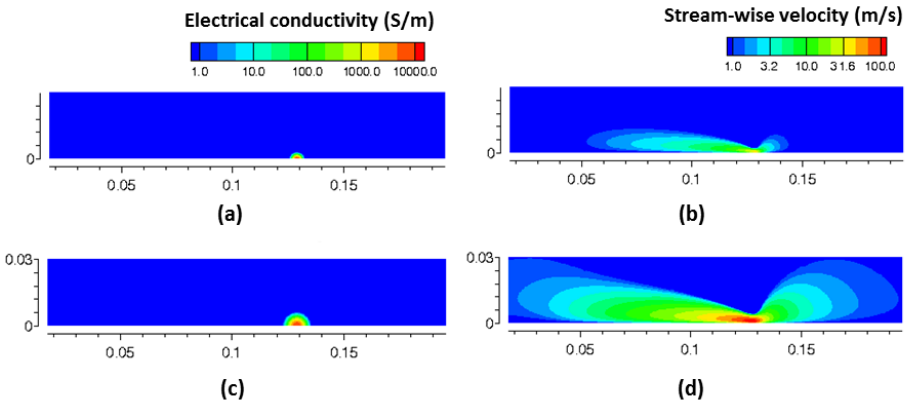

Figure 6.9: (a) Assumed conductivity profile having a radius of approximately 2 mm after 1 ms (b) stream-wise velocity profile for this case after 1 ms (c) assumed conductivity profile having a radius of 5 mm after 1 ms (d) stream-wise velocity profile for this case

Figure 6.9 shows the sensitivity to the assumed Gaussian profile for conductivity. Figure 6.9 (a) shows the assumed conductivity profile of radius 2 mm while 6.9 (c) shows the base case conductivity profile which has a radius of 5 mm. All the snapshots in this figure are at time $t = 1\ ms$. The actuation obtained is higher for the latter case as seen from the stream-wise velocity plots in 6.9 (b) and (d). Greater perturbation on the flow is attained with larger extent of the current sheet along the y direction due to larger integrated Lorentz forcing.

6.4.4 Heating effects

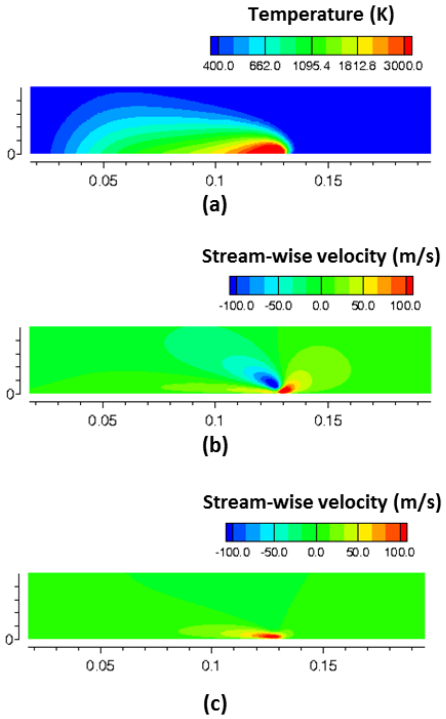

Figure 6.10: (a) Temperature and (b) velocity contours for case with heat addition (heating fraction = 0.1). (c) velocity contours for case without heat addition

The heating effects have been neglected in the results shown in figures 6.7-6.9. A heating fraction of 0.1 is assumed for the base case simulations with the assumed conductivity profile shown in 6.7 (a). This implies 10% of the Joule heating ($\sigma|\vec{E}_{app}|^2$) is assumed to go into heating the gas while the rest of the input electrical energy goes into the electron pool and ion energy losses to the wall. Figure 6.10 (a) shows the temperature profile at time $t = 1\ ms$. Temperatures $\sim$ 3000 K are attained at the location of the current sheet. The

velocity actuation for the heat addition case is shown in figure 6.10 (b). A region of negative stream-wise velocity is obtained due to the translating blast wave created by the energy addition compared to the case without heating (figure 6.10(c)).

Chapter 7

Conclusions and future work

The development of a magnetohydrodynamics numerical tool for studying high density thermal plasmas is presented in this dissertation. The numerical tool is used to study the physics of two devices - a coaxial plasma accelerator and a flow control device called the Rail Plasma Actuator.

There are three different facets to this dissertation. First and foremost, is the development of the numerical model and its verification, which is covered in chapters 2, 3 and 4. The second and third are the application of this code to study the coaxial plasma accelerator (chapter 5) and the Rail Plasma Actuator (chapter 6), respectively. The conclusions and future work with regard to each of these facets is presented in this chapter.

7.1 Development of MHD model

7.1.1 Conclusions

The resistive magneto-hydrodynamics (MHD) governing equations represent eight conservation equations for the evolution of density, momentum, energy and induced magnetic fields in an electrically conducting fluid, typically a plasma. A matrix free implicit method is developed to solve the conservation equations within the framework of an unstructured grid finite volume

formulation. The analytic form of the convective flux Jacobian is derived on a general unstructured mesh and used in a Lower-Upper Symmetric Gauss Seidel (LU-SGS) technique developed as part of the implicit scheme. A grid coloring technique is also developed to create data parallelism in the algorithm. The numerical method was verified using the MHD shock tube, oblique shock and Hartmann flow test cases for accuracy and convergence. The computational efficiency of the matrix free method is compared with two other techniques: a global matrix solve technique that uses the GMRES (Generalized minimum residual) algorithm and an explicit method. The matrix-free method is observed to be overall computationally faster than the global matrix solve method and demonstrates excellent parallel scaling on multiple cores. The computational effort and memory requirements for the matrix free approach is comparable to the explicit approach which in turn is much lower than the global matrix solve approach. Both the matrix free and global solve implicit techniques exhibit superior steady state convergence compared to the explicit method.

7.1.2 Future work

The steady state convergence rate of the both the implicit methods tend to be slow for low speed flow problems such as the Hartmann flow discussed in section 4.3. This is because of the use of a compressible flow solver for a low Mach number, near incompressible flow making the governing equations extremely stiff. The ratio of the largest to the smallest Eigen values of the convective flux Jacobian vary as the reciprocal of the fast magnetosonic Mach

number. The equations need to be pre-conditioned to reduce the stiffness of the governing equations. This technique is widespread in the compressible Navier-Stokes community [149, 150] and has been applied to the MHD equations as well [151].

The matrix free LU-SGS technique can be used as a pre-conditioner to the GMRES method. This combination methodology is observed to have superior convergence for steady state problems, compared to either of the methods, used separately [115]. The default block Jacobi pre-conditioning method as part of the PETSc libraries tend to be less efficient with larger number of processors, because of the increased use of older values, thereby slowing the convergence of the minimum residual solves [152]. On the other hand, the LU-SGS technique developed in this work, does not use older values with more processors, thereby keeping the convergence rate the same.

7.2 Coaxial plasma accelerator studies

7.2.1 Conclusions

A resistive magneto-hydrodynamics numerical model has been used to study coaxial plasma accelerators. The effect of plasma conductivity on the mode of operation has been investigated. It is seen that the plasma current densities are confined close to the inlet end for low conductivity cases while current sheet like features develop at high conductivities. The former is a characteristic of the deflagration mode of operation while the latter is seen in the detonation or snowplow mode of operation. A comparison of the piecewise integrated current densities was made with experimental measurements. The

simulated results agreed well with the experiments for the low conductivity case but not for the higher conductivity case. This is probably due to a higher value of conductivity used in the calculation resulting in lower fluid residence time compared to the experiment. A qualitative comparison can be made with regard to formation of current sheet like features in the simulation at higher conductivities. Simulations were also performed to model the exit plume of the coaxial plasma accelerator. Higher temperatures were seen at the exit end of the cathode brought about by pinching effects due to high axial currents. Directed particle energies $\sim$ 1 keV were obtained at the exit plane which is consistent with experimental measurements. The model validates the theory about the role of plasma resistivity in determining the mode of operation in a coaxial plasma accelerator.

7.2.2 Future work

A purely temperature dependent Spitzer model is used to calculate the plasma resistivity in the coaxial plasma accelerator simulations. This model tends to be valid only for fully ionized plasmas. Therefore, a temperature and number density dependent conductivity model need to be employed. The expansion of the plasma into near vacuum conditions is modelled by imposing a 10 Pa pressure at the exit. The pressure tends to be on the order of mTorrs in the experiments, where the continuum assumptions are not valid. A Lagrangian particle model along with the fluid equations need to be used to account for the high Knudsen number flows encountered at the exit. The fluid Reynold's number for the low and high conductivity cases are on the

order of 3500 and 20,000, respectively, for a length scale of 5 cm, which is the diameter of the coaxial plasma accelerator. Flow turbulence effects should be accounted, at least in the high conducitivity case, using Reynold's averaged MHD equations and turbulence models for obtaining the Reynold's stresses.

7.3 Rail plasma actuator studies

7.3.1 Conclusions

A single fluid resistive magneto-hydrodynamics model has been used to study the flow actuation effects brought about by the Rail Plasma Actuator (RailPAc). The MHD governing equations is modified with additional flux and source terms that arise from inclusion of applied electric and magnetic fields. A preliminary one dimensional analysis of the RailPAc was performed using the snowplow model, which predicted the motion of the arc. The current sheet propagation speeds compared well with experimental measurements. Two dimensional simulations were performed assuming the plasma is in a state of Local Thermodynamic Equilibrium (LTE). The single fluid MHD model was unable to capture the propagating current sheet like behaviour seen in the experiments. Simulations were performed with an assumed propagating region of high conductivity, representing the current sheet and actuation due to purely Lorentz forces was studied. A peak actuation $\sim$ 100 m/s was observed close to the high conductivity region. The inclusion of Joule heating along with the Lorentz forcing source terms showed isotropic actuation in the vicinity of the current sheet.

7.3.2 Future work

The non-equilibrium nature of the plasma has to be accounted, to capture the motion of the high conductivity plasma column, in a self-consistent manner. The single fluid MHD equations should be coupled with the non-equilibrium plasma governing equations much the same way as Navier-Stokes plasma coupling models used in the study of glow discharge based actuators and electro-thermal thrusters [153, 154]. The non-equilibrium model solves for electron densities and temperatures which can be used to evaluate plasma conductivity and energy source terms for the single fluid MHD model. Parameters such as pressure, velocity, temperature and induced magnetic fields can be fed back into the non-equilibrium solver completing the iterative coupling process. Flow Reynold's numbers are on the order of 200,000 for the cases studied, which requires the use of Reynold's averaged governing equations with turbulent stress terms.

Chapter 8

Previous work on modeling of microdischarges

A brief description of the work done by the author prior to start of the high density plasma modeling project is presented in this chapter. The author was part of a project that involved modeling of high pressure small length scale $\sim$ 10-50 μm plasmas called microdischarges. Application of these discharges were for the design of micro-propulsion devices for small satellites. The computational model used in this study was developed by the research group and is vastly different from the MHD model described earlier. Outcome of this research work was published in ref. [100–102].

8.1 Introduction

Microdischarges are finding way into several applications such as photonics and biomedical devices [155, 156]. These discharges are in a state of thermal non-equilibrium similar to glow discharges and operate over very small length scales $\sim$ 10-50 μm. They are relatively stable at nominally high pressures $\sim$ 1 atm. with low breakdown voltages $\sim$ 100-500 V governed by the Paschen curve [157]. The plasma and volumetric power densities seen in these discharges are much higher compared to larger glow discharges (electrode gaps $\sim$ mm). The high power densities also lead to significant gas heating in

microdischarges with gas temperature increase of hundreds to thousands of kelvin above the wall temperature. Microdischarges have been proposed for use in electrothermal microthrusters for small satellite propulsion [154]. These devices, known as micro plasma thrusters (MPTs), use a direct-current microdischarge to preheat a propellant stream within a cold-gas microthruster, thus resulting in improved thrust and specific impulse. One of the drawbacks of this design is the erosion of exposed electrodes due to ion bombardment and heating effects. An improvement to the MPT design can be achieved by using refractory dielectric-covered electrodes [158]. An alternating-current [e.g., radio frequency (RF)] excitation of the microdischarge is consequently needed to drive power into the device, resulting in pulsed microdischarge operation. We report the computational results of an RF-excited, dielectric-covered, microdischarge-based microthruster.

8.2 Computational model

A detailed first principles plasma model coupled to a compressible Navier-Stokes fluid flow model is used [154]. The plasma model solves for the charged and neutral species transport, the self-consistent electrostatic fields, and the electron temperature. The cycle-averaged thermal source term (owing to ion Joule heating, electron elastic and inelastic collisions) is computed by the plasma model and used as the energy source term in the compressible Navier-Stokes equations. The gas temperature, pressure and flow velocity fields computed by the Navier-Stokes solver are used as inputs for the plasma solution. A pure argon propellant is considered, and the finite rate chemistry

model for the same is discussed in [154].

8.3 Results

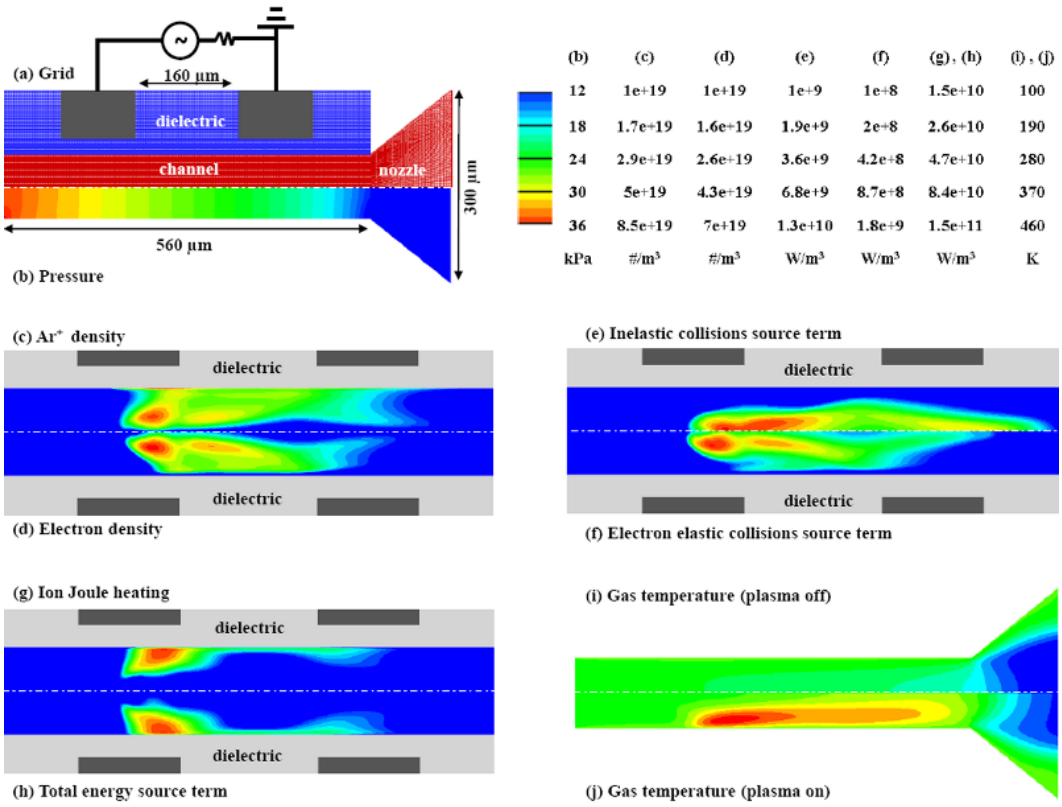

Figure 8.1: Simulation results of a micro cavity discharge thruster at an operating voltage of 600 V with 20 MHz.

Figure 8.1(a) shows the microthruster geometry and the computational mesh used in this work, comprising a total of about 16000 cells. The geometry consists of an axisymmetric constant-area channel section 560 μm long, followed by a diverging nozzle section 140 μm in axial length. The diameters of the channel and nozzle exit sections are 100 and 300 μm, respectively. The

distance between the electrodes is 160 μm. The dielectric material is assumed to have a relative permittivity of 9.0, which is similar to that of glass. Its thickness that separates the electrodes from the gas is 40 μm. The Navier Stokes equations are solved in the gas sub-domains (channel and nozzle sections) while the plasma governing equations are solved only in the channel section. Only Poisson's equation for the electrostatic potential is solved in the dielectric sub-domain. The applied voltage waveform for the case shown is at an amplitude of 600 V with 20 MHz frequency. The total pressure and total temperature at the inlet are 40 kPa and 300 K, respectively. The wall temperatures are fixed at 300 K. A very low pressure of 10 Pa is imposed at the "vacuum" exit plane. Figure 8.1(b) shows the cold-gas pressure distribution in the thruster. The pressure reduces along the downstream direction as the flow accelerates through the channel section. Figure 8.1(c) shows the cycle-averaged number density of the dominant ion Ar^+ in the channel section. Number densities on the order of $7 \times 10^{19} m^{-3}$ are seen in the bulk of the discharge. Figure 8.1(d) shows the cycle-averaged electron number density in the discharge. High electron densities are observed close to the axis. The electrons are confined between the oscillating sheaths in the RF discharge. This, in turn, promotes greater ionization in the bulk of the discharge. Power deposition in the neutral gas is a combination of ion Joule heating, energy transfer through inelastic collisions in the plasma, and energy transfer through elastic collisions of electrons with the neutral species. Figure 8.1(e) and (f) shows the cycle-averaged power deposition in the neutral gas through inelastic and elastic collisions, respectively. The integrated power deposition through inelastic

collisions is about 3 mW, while it is about 0.5 mW through elastic collisions. Figure 8.1 (g) and (h) shows the cycle-averaged ion Joule heating and the total energy source term in the plasma, respectively. It is observed that the ion Joule heating is much higher than the inelastic and elastic collision terms. The integrated power deposition through ion Joule heating is observed to be about 64 mW, which is about 75% of the total electrical power of 84 mW. The ion Joule heating is higher close to the wall in the oscillating RF sheaths, owing to the high electric fields. The integrated cycle-averaged total power deposition in the neutral gas is about 68 mW. Figure 8.1(i) and (j) shows the temperature contours in the cold-gas case (plasma off) and the hot-gas case after power deposition (plasma on),respectively, which indicate a maximum temperature rise of about 160 K.

Simulations were also performed with a driving voltage frequency of 10 MHz and also with argon-nitrogen mixture as the propellant gas. The peak electron density increases with increase in the drive frequency as shown in figure 8.2(a) and (b). This increase is attributable to the improved capacitive power deposition efficiency at higher frequencies [7]. The integrated ion Joule heating is also calculated to be higher for the 20 MHz excitation ($\sim$ 64 mW) compared with the 10 MHz case (46 mW) as shown in 8.2(c) and (d). Deliberate addition of small amount of nitrogen can improve the contribution of the inelastic collisional heating in the discharge. Nitrogen is characterized by various low energy rotational, vibrational and electronic energy states that are readily excited by the electrons. These states are also quenched rapidly by collisions with the background gas thus providing an efficient pathway for

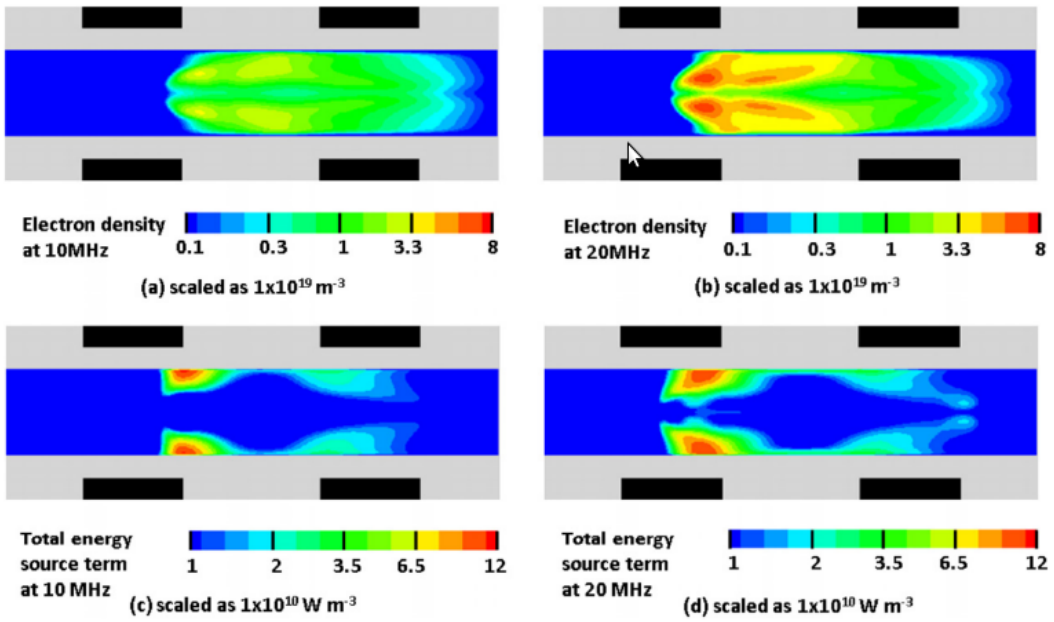

Figure 8.2: Electron densities for (a) 10 MHz and (b) 20 MHz excitation; total gas energy source term for (c) 10 MHz and (d) 20 MHz excitation

transfer of electron energy to the gas by the inelastic collision mode. Simulation studies were done on the same geometry as shown in figure 8.1(a), the only difference being the use of argon-nitrogen (80-20 %) mixture as the propellant gas. The volume and time-averaged ion Joule heating (figure 8.3(a)) contributes about 88% of the total power deposition while inelastic collision source term (figure 8.3(b)) contributes about 12%. The contribution of inelastic collisions in the pure argon case was about 6%. The use of nitrogen (and indeed other molecular gases) to noble gas propellants is therefore a viable approach for improved gas heating in electrothermal class of thrusters driven by cold plasmas.

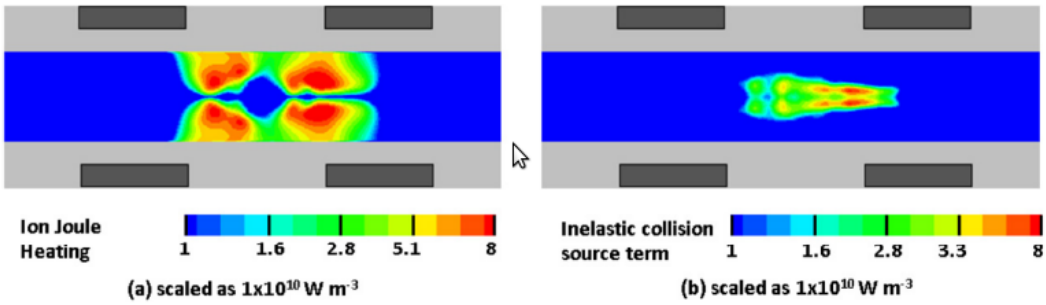

Figure 8.3: (a) Ion Joule heating and (b) inelastic collision source term for the $Ar - N_2$ case.

8.3.1 Thruster performance calculations

The time averaged total gas power deposition is used as energy source term in the bulk flow Navier-Stokes equations to realize enhancements to the thrust and specific impulse. Figures 8.4(a),(b) and (c) show the temperature distribution in the propellant gas flow for pure argon at 10 MHz and 20 MHz RF excitations and for the 80% argon 20% nitrogen case discussed earlier. The top half of both figures shows the temperature profile for the cold gas case, while the bottom half shows temperatures for the plasma-on cases. Peak gas temperature rise of $\sim$ 160 K is observed for the pure argon case at 20 MHz and a slightly lower peak temperature rise is observed for the 10 MHz case. The peak gas temperature rise is seen to be highest $\sim$ 200 K for the argon-nitrogen case. Moreover, the temperature rise is seen to be close to the axis compared with the pure argon cases. The volumetric footprint of the temperature increase is significantly larger for the argon-nitrogen case compared with the pure argon cases at 10 and 20 MHz. The larger gas heating observed in the 20 MHz excitation is obviously due to higher cycle integrated thermal source

term. The argon-nitrogen case shows the highest increase in temperature due to the presence of higher cycle-integrated thermal source terms away from the wall. This reduces the loss of energy through heat conduction at the dielectric surfaces and a larger fraction goes into heating the propellant flow. Figures 8.4 (c), (d) and (e) show the flow axial velocity distribution for the three different cases discussed above. A peak velocity $\sim 650\ m/s$ is seen at the exit plane for the argon nitrogen case at 10 MHz. compared with $\sim 500\ m/s$ in the case of the cold gas thruster.

Case	Mass flow rate (mg/s)	Total power (mW)	Thermal source term (mW)	Thrust (μN)	Specific impulse (s)
cold gas	0.55	0	0	299	55
10 MHz	0.45	62	50	269	61
20 MHz	0.44	84	68	278	65
10 MHz $Ar - N_2$	0.37	83	76	252	69

Table 8.1: Performance parameters for cold and hot gas cases.

Table 8.1 summarizes the various performance parameters for the different cases discussed above. Note that the discharge powers shown in table 8.1 are averaged over a RF cycle. It is seen that the electrical power for the argon-nitrogen case is higher than the pure argon cases at 20 and 10 MHz. The fraction of discharge power that is converted to thermal energy remains more or less the same for the pure argon cases while it is higher for the argon-

nitrogen case due to larger contribution from inelastic collision source terms. The thrust is calculated based on the pressure and axial velocity at the exit plane as shown in equation 8.1.

$$\text{Thrust}, T = \int_0^R \left(P + \rho V_{ax}^2\right) 2\pi r \mathrm{d}r \tag{8.1}$$

$$\text{Specificimpulse}, I_{sp} = \frac{T}{\dot{m}g} \tag{8.2}$$

The specific impulse is calculated as the ratio of the thrust to the mass flow rate times the acceleration due to gravity g as shown in equation 8.2. The mass flow rate tends to decrease slightly with heat addition in the channel section. This is owing to the increase in stagnation temperature while keeping the stagnation pressure a constant; effectively a blockage in the channel that causes an increase in the flow resistance. Thrust also decreases with heat addition but the specific impulse for the hot gas cases is higher than the cold gas. A specific impulse enhancement $\sim 14\ s$ is observed for the argon-nitrogen case while a rise of about 10 s is seen for the 20 MHz case. The performance enhancement trends observed with increase in frequency and addition of molecular nitrogen is consistent with the experimental work described in ref [159].

8.4 Conclusions

The discharge phenomenon in an RF excited micro-cavity discharge thruster has been simulated using a coupled plasma-flow model. The cycle-averaged thermal energy source terms are obtained by solving the plasma

governing equations which are then coupled with the Navier-Stokes model to obtain enhancement in specific impulse. The operation of the thruster using an alternating current waveform of amplitude, 600 V with varying frequency (10 MHz, 20 MHz) is studied. Results indicate a highly pulsed microdischarge with plasma densities of $\sim 10^{19}\ m^{-3}$ and gas temperature excursions of ~ 150 K occurring in the discharge during the pulse. It is also seen that the dominant heating mechanism in these discharges are through ion Joule heating. The addition of molecular gas such as nitrogen into the noble gas propellant stream increases the contribution of the inelastic collision source term significantly. Higher electron densities and spatially dominant thermal source terms are observed at 20 MHz excitation compared with the 10 MHz case. A specific impulse of 61 s was seen after power deposition for the 10 MHz case compared with cold gas specific impulse of 55 s. Higher specific impulse (65 s) is observed for the pure argon case at 20 MHz compared with the 10 MHz case. The addition of 20% nitrogen to the flow resulted in much better performance compared with the pure argon cases. The specific impulse for this case was seen to be 69 s which is the highest among the three cases studied. The results validate the RF excited micro-cavity discharge concept for electrothermal microthruster applications. For the conditions explored in this study, the overall specific impulse of the thruster operating with the microdischarge plasma is found to be about 25% higher than a corresponding cold gas case.

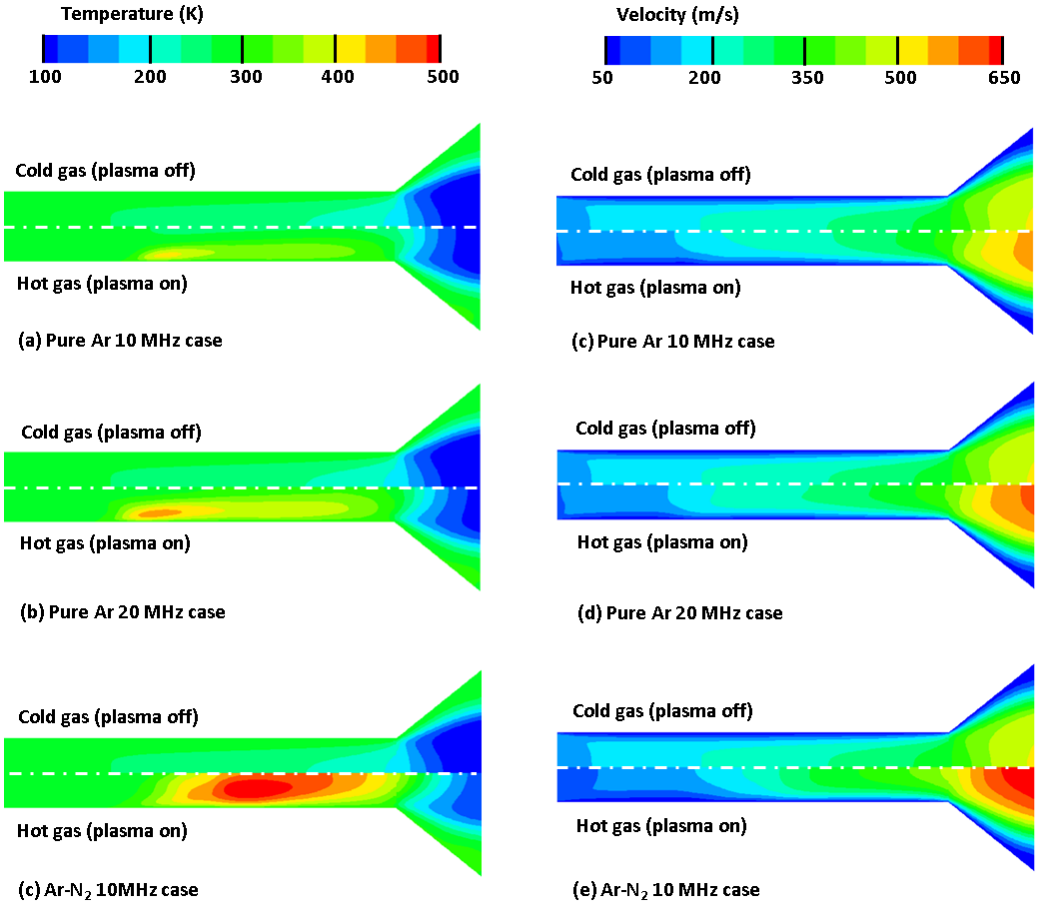

Figure 8.4: Comparison of gas temperature distribution for cold and hot gas cases for (a) pure Ar at 10 MHz, (b) pure Ar at 20 MHz, (c) $Ar - N_2$ at 10 MHz; comparison of axial velocity distribution for cold and hot gas cases for (d) pure Ar at 10 MHz (e) pure Ar at 20 MHz,(f) $Ar - N_2$ at 10 MHz

Appendices

Appendix A

Non-convex nature of MHD equations

A theoretical analysis related to the convective term in the MHD governing equations is presented in this chapter. This term is responsible for the three different wave speeds which give rise to the various features (such as the "kink") seen in the MHD shock tube problem in chapter 4. The treatment of the governing equations using the method of characteristics is presented here along with the notion of convexity of general hyperbolic systems. Such a treatment of general hyperbolic systems, particularly the compressible Euler equations are given in famous textbooks by Toro [72], Leveque [160] and Jeffrey et al. [161]. Specific treatment of the ideal MHD equation system along with the Eigen structure of the convective flux Jacobian have been studied by Roe et al. [162] and Godunov [163].

This chapter is organized as follows. The concept of convexity for a one dimensional hyperbolic equation is first introduced and then extended to hyperbolic systems in sections A.1 and A.4. The Eigen structure of the one dimensional MHD equations are closely studied in section A.6 and the non-convexity of these equations are proved. This leads to the discussion of the MHD shock tube in section A.7 and the various shock and expansion waves in the solution are analysed using method of characteristics. The slow compound

wave is then closely analysed using the idea of convexity in this section.

A.1 One dimensional hyperbolic equation

A one dimensional single variable hyperbolic equation of the form shown in equation A.1 will be studied here to understand convexity. Let us assume here that f is a function of u.

$$\frac{\partial u}{\partial t} + \frac{\partial f}{\partial x} = 0 \quad u(x,0) = u_0(x) \tag{A.1}$$

Equation A.1 can also expressed as shown below.

$$\frac{\partial u}{\partial t} + \lambda(u)\frac{\partial u}{\partial x} = 0 \quad \lambda(u) = \frac{\partial f}{\partial u} \tag{A.2}$$

From equation A.2 it is evident that there is no change in u along curves in x-t plane whose slope is equal to $\lambda(u)$ as shown in equation below.

$$if \quad \frac{dx}{dt} = \lambda(u) \quad then \quad \frac{du}{dt} = \frac{\partial u}{\partial t} + \frac{dx}{dt}\frac{\partial u}{\partial x} = 0 \tag{A.3}$$

We can also conclude that these curves in x-t plane are straight lines since the value of the slope depends on u and it is a constant along that line with the value that is known at t=0. That is the slope of the line through a point x_p will be $\frac{dx}{dt} = \lambda(u_0(x_p))$.

A.2 Regarding convexity

The *convexity* of a hyperbolic equation can be defined based on the nature of $\lambda(u)$. If $\lambda(u)$ is *monotonically increasing* for all values of u, then the hyperbolic equation is convex. The equation is *concave* if $\lambda(u)$ is *monotonically decreasing*.

The physical meaning behind the idea of convexity can be seen in the way the characteristics change their slopes to create shock and expansion waves with a given initial data. For example, the slopes of characteristics tend to increase in regions where $u_0(x)$ is increasing if $\lambda'(u) > 0$ and decrease where $u_0(x)$ decreases.

This brings up an important point about convex/concave hyperbolic equations. For arbitrary initial data $u_0(x)$, the characteristics can either produce shocks or expansions and never both of them together. This fact will be illustrated with the example of the inviscid Burger's equation in section A.3.

A.3 Example: Inviscid Burger's equation

Equation A.4 is known as the inviscid Burger's equation which is a single variable non-linear hyperbolic equation. The characteristic wave speed $\lambda(u)$ is equal to u here. Since it is monotonically increasing with respect to u, this equation is convex.

$$\frac{\partial u}{\partial t} + u\frac{\partial u}{\partial x} = 0 \qquad u(x,0) = u_0(x) \tag{A.4}$$

Figure A.1 shows two cases corresponding to two different initial con-

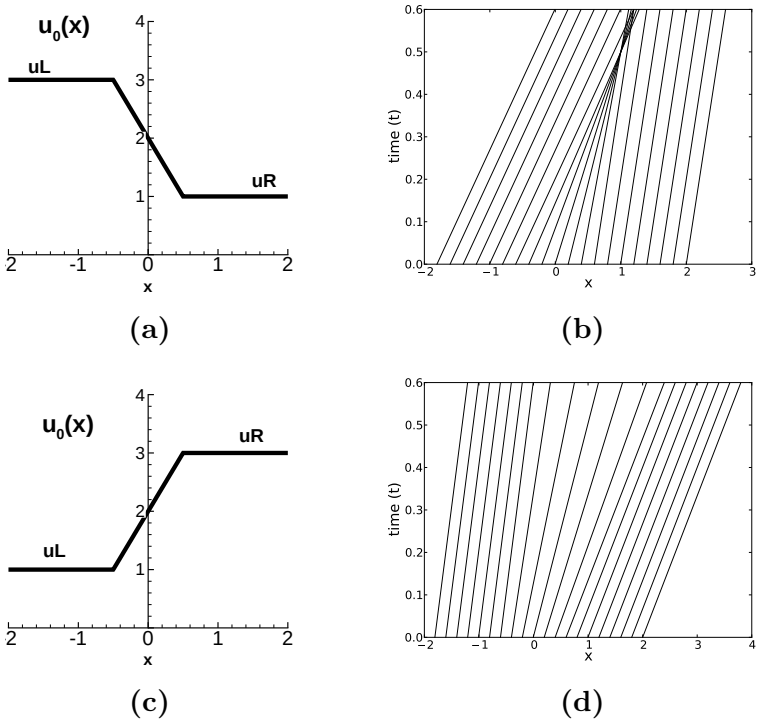

Figure A.1: (a) Initial data for u at t=0 where left state is greater than right. (b) characteristics corresponding to case (a). (c) Initial data for u at t=0 where left state is less than right state. (d) characteristics corresponding to case (c).

ditions for u. For the case shown in Fig. A.1(a), the values on the left hand side are greater than the values on the right which are connected through a smooth linear transition region. The Riemann problem [72] is a limiting case of this scenario where the transition region width reduces to zero. The characteristics corresponding to this case is shown in Fig. A.1 (b). They converge at a single point due to reduction in slope in the transition region which leads to the formation of a shock. The contrasting picture arises for the initial condition shown in Fig. A.1 (c) where the characteristics tend to diverge in the

transition region leading to formation of an expansion fan as shown in Fig. A.1 (d).

A.4 Convexity in hyperbolic systems

A general time dependent hyperbolic system in one dimensional space coordinates can be written as shown in equation A.5.

$$\frac{\partial[U]}{\partial t} + \frac{\partial[F]}{\partial x} = 0 \tag{A.5}$$

Eq. A.5 is a set of n hyperbolic equations. Here $[U]$ is an n tuple of conserved variables and $[F]$ is referred to as the flux term which can be in general a function $[U]$, x and t. Let us assume that $[F]$ is a function of $[U]$ alone. Equation A.5 can also be written in the form shown in Eq. A.6 where $\mathbf{J}$ is the flux Jacobian matrix.

$$\frac{\partial[U]}{\partial t} + \mathbf{J}\frac{\partial[U]}{\partial x} = 0 \quad \mathbf{J} = \frac{\partial[F]}{\partial[U]} \tag{A.6}$$

The set of n non-linear equations will then give rise to n different characteristic wave speeds as opposed to just one wave speed seen in section A.1. These different characteristic wave speeds are the eigenvalues of the flux Jacobian matrix. The idea of convexity here will be then related to how these wave speeds behave. The terminology that is used in hyperbolic systems to extend the idea of convexity is to classify them as *genuinely non-linear* and *linearly degenerate* characteristic fields [72].

Let us denote the eigen values of the flux Jacobian **J** as $\lambda_k([U])$ and its corresponding right eigen vector as $r_k([U])$.

Definition 1. *Characteristic field associated with eigen value λ_k is genuinely non-linear if the variation of the wave speed along the eigen vector is* ***never*** *zero for all values of $[U]$.*

$$\vec{\nabla}\lambda_k.r_k \neq 0 \quad \forall\, [U] \in R^n \tag{A.7}$$

An important property of genuinely non-linear fields which is similar to the idea of convexity is that they produce either shocks or expansion waves but not both of them together.

Definition 2. *Characteristic field associated with eigen value λ_k is linearly degenerate if the variation of the wave speed along the eigen vector is* ***always*** *zero for all values of $[U]$.*

$$\vec{\nabla}\lambda_k.r_k = 0 \quad \forall\, [U] \in R^n \tag{A.8}$$

These kind of characteristic fields end up as contact discontinuities in the solution. They have an important property where in the speed of the discontinuity is the same as the characteristic speeds on its upstream and downstream sides. This also implies that the discontinuity propagates at the characteristic wave speed itself.

A.5 One dimensional MHD equations

The analysis of these equations are again done in single dimensional space. Therefore the variation of quantities are only along the x direction. Divergence free criterion for magnetic field makes the x component of magnetic field (B_x) a constant. The set of primitive variables will then be a 7 tuple of the form $[\rho, u, v, w, B_y, B_z, P]$ as opposed to just 3 variables in the case of one dimensional Euler equations. The modified set of hyperbolic equations can be written out as shown in equation A.9 after using the scaling parameters shown in table 3.1 from chapter 3. The total pressure P_t is the sum of the thermodynamic and magnetic pressure given by $P_t = P + \frac{|B|^2}{2}$.

$$\frac{\partial}{\partial t}\begin{bmatrix} \rho \\ \rho u \\ \rho v \\ \rho w \\ B_y \\ B_z \\ \rho Z \end{bmatrix} + \frac{\partial}{\partial x}\begin{bmatrix} \rho u \\ (\rho u^2 + P_t - B_x^2) \\ (\rho v u - B_y B_x) \\ (\rho w u - B_z B_x) \\ (B_y u - v B_x) \\ (B_z u - w B_x) \\ (\rho Z + P_t)u - (uB_x + vB_y + wB_z)B_x \end{bmatrix} = 0 \qquad \text{(A.9)}$$

A.6 Eigen decomposition of MHD flux Jacobian

The eigen structure of the MHD flux term in equation A.9 is evidently not easy to derive compared to the Euler equations from gas dynamics. Roe et al. [162] derived the flux Jacobian for the MHD equations using primitive variable $[W] = [\rho, u, v, w, B_y, B_z, P]$ governing equations. The equations in terms

of conservative variables (equation A.9) can be recast in terms of primitive variables as shown below.

$$\frac{\partial [W]}{\partial t} + \mathbf{A}([W])\frac{\partial [W]}{\partial x} = 0$$

$$\mathbf{A} = \begin{bmatrix} u & \rho & 0 & 0 & 0 & 0 & 0 \\ 0 & u & 0 & 0 & \frac{B_y}{\rho} & \frac{B_z}{\rho} & \frac{1}{\rho} \\ 0 & 0 & u & 0 & -\frac{B_x}{\rho} & 0 & 0 \\ 0 & 0 & 0 & u & 0 & -\frac{B_x}{\rho} & 0 \\ 0 & B_y & -B_x & 0 & u & 0 & 0 \\ 0 & B_z & 0 & -Bx & 0 & u & 0 \\ 0 & \rho a^2 & 0 & 0 & 0 & 0 & u \end{bmatrix}$$

$$speed\, of\, sound\, a = \sqrt{\left(\frac{\gamma P}{\rho}\right)} \tag{A.10}$$

The eigen values of the **A** matrix can be evaluated in terms of the sound, Alfven, slow and fast plasma wave speeds to give a set as shown below.

$$\lambda_i = [u - c_f, u - \alpha, u - c_s, u, u + c_s, u + \alpha, u + c_f]$$

$$Alfven\,wave\,speed \quad \alpha = \frac{B_x}{\sqrt{\rho}}$$

$$slow\,wave\,speed \quad c_s^2 = \frac{1}{2}\left(a^2 + \frac{|B|^2}{\rho} - \sqrt{\left(a^2 + \frac{|B|^2}{\rho}\right)^2 - 4\alpha^2 a^2}\right)$$

$$fast\,wave\,speed \quad c_f^2 = \frac{1}{2}\left(a^2 + \frac{|B|^2}{\rho} + \sqrt{\left(a^2 + \frac{|B|^2}{\rho}\right)^2 - 4\alpha^2 a^2}\right) \quad \text{(A.11)}$$

The right eigen vectors corresponding to each of the eigen values also have been derived by Roe et al. [162] which will not be completely dealt with. The direction now will be to examine the nature of the characteristics themselves and see if non convexity exist in MHD equations. This will be demonstrated by looking closely at just one of the characteristic fields alone, which is the $u - c_s$ eigen value.

Theorem 1. *The Characteristic fields corresponding to eigen value $u - c_s$ is non convex.*

Proof. Instead of an algebraic treatment, the variation of the eigen value is plotted against a parameter which will be B_y here. The right eigen vector corresponding to the eigen value $u - c_s$ is as shown below. This has been derived by Roe et al. [162].

$$r_s = \begin{bmatrix} \rho\alpha_s \\ -\alpha_s c_s \\ -\alpha_f c_f \beta_y \\ -\alpha_f c_f \beta_z \\ -\alpha_f \sqrt{\rho} a \beta_y \\ -\alpha_f \sqrt{\rho} a \beta_z \\ \alpha_s \gamma P \end{bmatrix}$$

$$\alpha_f^2 = \frac{a^2 - c_s^2}{c_f^2 - c_s^2} \quad \alpha_s^2 = \frac{c_f^2 - a^2}{c_f^2 - c_s^2}$$

$$\beta_y = \begin{cases} \frac{B_y}{\sqrt{B_y^2 + B_z^2}} & if\ B_y^2 + B_z^2 \neq 0 \\ \frac{1}{\sqrt{2}} & if\ B_y^2 + B_z^2 = 0 \end{cases}$$

$$\beta_z = \begin{cases} \frac{B_z}{\sqrt{B_y^2 + B_z^2}} & if\ B_y^2 + B_z^2 \neq 0 \\ \frac{1}{\sqrt{2}} & if\ B_y^2 + B_z^2 = 0 \end{cases}$$

(A.12)

To show the non convexity here, we just need to prove that the characteristic field is neither genuinely non-linear nor linearly degenerate. For a special case which will be relevant in the discussion of the MHD shock tube, the variation of the eigen value along the right eigen vector is plotted against B_y (transverse magnetic field) as a parameter in figure A.2. The calculation is done for a case of primitive variables as shown below. B_y is assumed to vary between -1 and 1.

$$[W] = \begin{bmatrix} 1.0 \\ 0.0 \\ 0.0 \\ 0.0 \\ 0.75 \\ B_y \\ 0.0 \\ 1.0 \end{bmatrix} \tag{A.13}$$

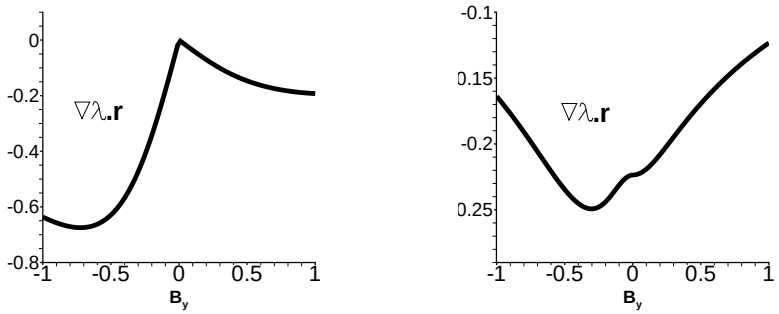

(a) **(b)**

Figure A.2: variation of $\vec{\nabla}\lambda.[r]$ against B_y for the eigen value $u - c_s$ where (a) speed of sound is greater than Alfven speed (b) speed of sound is less than Alfven speed

Figure A.2(a) shows that for the assumed values for primitive variables from equation A.13, $\vec{\nabla}\lambda.[r]$ goes to zero at $B_y = 0$ and is negative on either side of it. This shows that the characteristic field associated with $u - c_s$ is neither linearly degenerate nor genuinely non linear. Therefore the characteristic field is non convex.

Figure A.2(b) plots a case where the speed of sound is less than the

Alfven speed. This case is where the pressure value in equation A.13 is changed from 1.0 to 0.1. $\vec{\nabla}\lambda.[r]$ does not go to zero here for $B_y = 0$. Nonetheless, the statements for genuinely non-linear and linearly degenerate refer to all possible values of [W]. Therefore proving a single case is sufficient for non convexity.

□

A.7 MHD shock tube

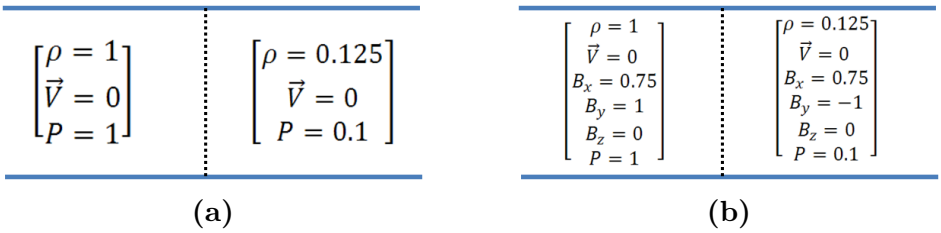

Figure A.3: primitive variables at time t=0 for (a) gas dynamic shock tube and (b) MHD shock tube

The classic gas dynamic shock tube, also referred to as the sod shock tube [164] in the Computational Fluid Dynamics community is as shown in figure A.3(a). It consists of a one dimensional domain from 0 to 1 with a sharp discontinuity in the middle that separates the driver region (higher pressure,density region) and the driven region (lower pressure,density region). The initial values of the primitive variables are also shown here. Figure A.3(b) shows a variant of the Sod shock tube for the magneto-hydrodynamics equations first studied Brio et al. [4] in 1988.

The pressure and density solution for both the Sod and MHD shock tube problems are shown side by side after time t=0.1 in figure A.4. The

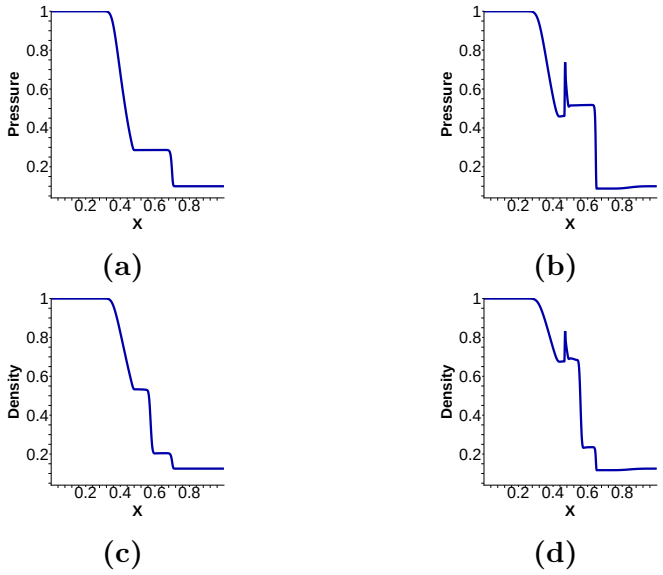

Figure A.4: pressure solution at time t=0.1 for (a) gas dynamic shock tube (b) MHD shock tube; density solution at t=0.1 for (c) gas dynamic shock tube (d) MHD shock tube.

hydrodynamics case shows the propagation of a shock to the right side and expansion waves to the left. The shock is brought about by the $u+a$ characteristics while the expansion waves are brought about by the $u-a$ characteristics. The contact discontinuity seen in the density plot (Figure A.4(c)) is brought about by the u characteristics. The MHD shock tube shows a rich variety of features which will be analysed closely. One of the easily discernable features is the contact discontinuity seen in A.4(d) which is brought about by the u characteristics in the MHD equations. There are infact 5 different features that are shown in Figure A.5 (a). The expansion wave on the extreme right and left sides are due to the fast plasma waves. The shock on the right hand side is due to the slow plasma wave. Feature 3 is the contact discontinuity.

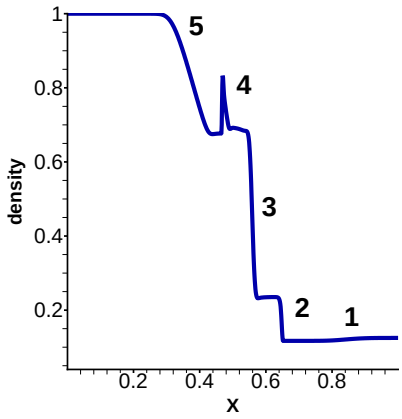

(a)

Number	Feature
1	Fast rarefaction
2	Slow shock
3	Contact
4	Slow compound
5	Fast rarefaction

(b)

Figure A.5: (a) density solution for the MHD shock tube with numbered features (b) table with the description of features seen in (a)

The kink like feature at 4 is referred to as the slow compound wave. This is where the significance of non convexity of MHD equations comes into picture.

The x component of velocity is plotted in figure A.6 (a). The marked region which is the same as Region 4 in figure A.5 is shown in figure A.6 (b). This figure is taken from the paper by Brio et al. [4] and shows the exact solution using Riemann invariants and the approximate solution computed using a Riemann solver. This feature is essentially a slow shock wave followed by an attached expansion wave. This shock wave is formed from the $u - c_s$ characteristics. In section A.6 we proved that these characteristics are non convex. This implies they can create both expansion and shock waves which is seen here.

To show that the shocks and the expansion waves are indeed brought

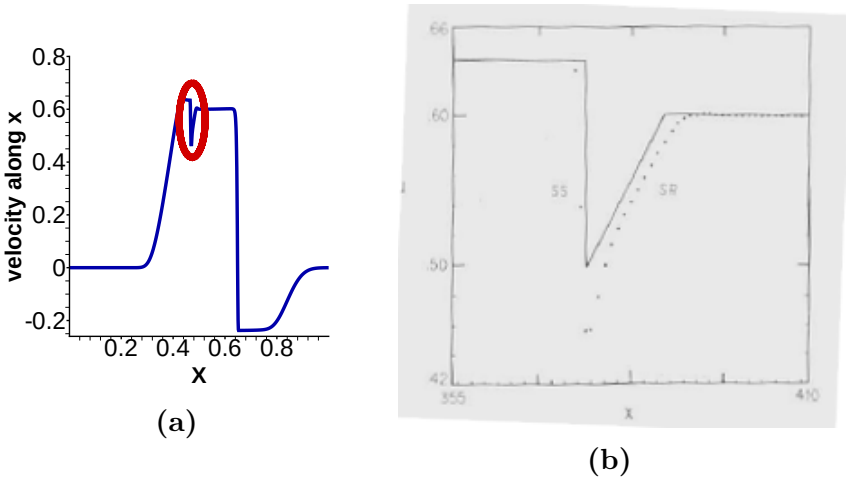

Figure A.6: (a) x component of velocity (u) solution at time t=0.1 (b) region marked red from (a) zoomed in showing the slow shock and attached expansion wave obtained from Brio et al. [4]

about by slow plasma waves and fast plasma waves respectively the characteristics are plotted for a case where we have a smooth linear variation in all the primitive quantites (similar to inviscid Burger's equation analysis) as opposed to the sharp initial condition in the MHD shock tube. The assumed variation of B_y and the wave speeds are shown in figure A.7. Note that as B_y goes to zero, the fast wave approaches the sound speed while the slow wave approaches the Alfven speed.

The initial condition for velocity is assumed to be zero. This implies, the $[c_s, c_f]$ characteristics propagate to the right while $[-c_s, -c_f]$ characteristics propagate to the left. These are shown in figure A.8. The slow plasma waves indeed form a shock when propagating to the right as shown in figure A.8(a) while the fast plasma waves form expansion waves towards either sides (figure

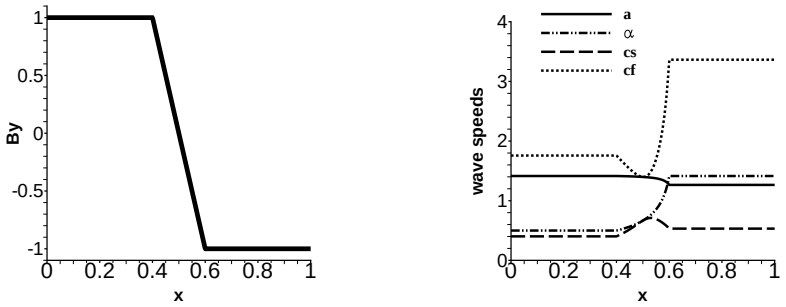

(a) **(b)**

Figure A.7: (a) assumed smooth variation of B_y in the MHD shock tube (b) wave speeds for the assumed smooth linear variation for all the quantites

A.8(b) and (d)). Note that the right propagating slow plasma waves also form a shock which is responsible for the shock wave part of the kink. This analysis will not lead us to the compound nature because once the shock is formed the characteristic analysis breaks down. Further calculations have to be done using Rankine Hugoniot jump conditions. A detailed treatment is given in the paper by Brio et al. [4].

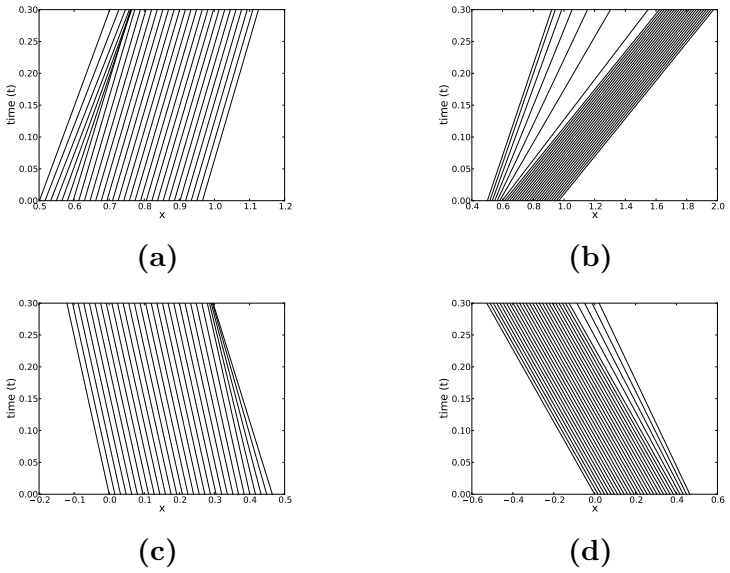

Figure A.8: (a) right propagating slow wave characteristics (b) right propagating fast wave characteristics (c)left propagating slow wave characteristics (d) left propagating fast wave characteristics

Bibliography

[1] M I Boulos, P Fauchais, and E Pfender. *Thermal Plasmas Fundamentals and Applications*. Plenum Press, 1994.

[2] F R Poehlmann, M A Cappelli, and G B Rieker. Current distribution measurements inside an electromagnetic plasma gun operated in a gas-puff mode. *Physics of Plasmas*, 17(12):123508, December 2010.

[3] B Pafford, J Sirohi, and L L Raja. Propagating-arc magnetohydrodynamic plasma actuator for directional high-authority flow control in atmospheric air. *J. Phys D: Appl. Phys.*, 2013.

[4] M Brio and C C Wu. An upwind differencing scheme for the equations of ideal magnetohydrodynamics. *Journal of Computational Physics*, 75(2):400 – 422, 1988.

[5] T Urakabe, S Harada, T Saikatsu, and M Karino. A flat fluorescent lamp with xe dielectric barrier discharges. *J. Light Vis. Environ.*, 20(2):20–25, 1996.

[6] B Eliasson, M Hirth, and U Kogelschatz. Ozone synthesis from oxygen in dielectric barrier discharges. *J Phys D:Appl. Phys.*, 20:1421–1437, 1987.

[7] M A Lieberman and A J Lichtenberg. *Principles of Plasma Discharges and Materials Processing.* Wiley-Interscience, 2nd edition, 2005.

[8] A Bernard, P Cloth, H Conrads, A Coudeville, G Gourlan, A Jolas, Ch Maisonnier, and P J Rager. The dense plasma focus - A high intensity neutron source. *Nucl. Inst. and Methods*, 145:191–218, 1977.

[9] Y C Thio, C E Knapp, R C Kirkpatrick, R E Siemon, and P J Turchi. A physics exploratory experiment on plasma liner formation. *J. Fusion. Energy*, 20, 2001.

[10] J Sovey and M Mantenieks. Performance and lifetime assessment of MPD arc thruster technology. *J. of Propulsion and Power*, 7, 1991.

[11] Y Raitses and N J Fisch. Parametric Investigations of a Nonconventional Hall Thruster. *Physics of Plasmas*, 8, 2001.

[12] A C Ducati, G M Giannini, and E Muehlberger. Experimental Results in High-Specific-Impulse Thermo-Ionic Acceleration. *AIAA Journal*, 2:1452–454, 1964.

[13] A H Glasser, C R Sovinec, R A Nebel, T A Gianakon, S J Plimpton, M S Chu, D D Schnack, and the NIMROD Team. The nimrod code: a new approach to numerical plasma physics. *Plasma Physics and Controlled Fusion*, 41(3A):A747, 1999.

[14] D S Balsara, R A Benjamin, and D P Cox. The evolution of adiabatic supernova remnants in a turbulent, magnetized medium. *The Astrophysical Journal*, 563(2):800, 2001.

[15] K Sankaran, L Martinelli, S C Jardin, and E Y Choueiri. A flux-limited numerical method for solving the mhd equations to simulate propulsive plasma flows. *International Journal for Numerical Methods in Engineering*, 53(6):1415–1432, 2002.

[16] E L Resler and W R Sears. The prospects for magneto-aerodynamicscorrection and addition. *Journal of the Aerospace Sciences*, 26(5):318, 1959.

[17] J Shang. Recent research in magneto-aerodynamics. *Progress in Aerospace Sciences*, 37:1–20, 2001.

[18] J S Shang. Shared knowledge in computational fluid dynamics, electromagnetics, and magneto-aerodynamics. *Progress in Aerospace Sciences*, 38(67):449 – 467, 2002.

[19] J Shang, B Ganguly, R Umstattd, J Hayes, M Arman, and P Bletzinger. Developing a facility for magnetoaerodynamic experiments. *Journal of Aircraft*, 37, 2000.

[20] M Nishihara, N Jiang, J W Rich, W R Lempert, I V Adamovich, and S Gogineni. Low-temperature supersonic boundary layer control using repetitively pulsed mhd forcing. *Physics of Fluids*, 17(10):106102, 2005.

[21] R Meyer, M Nishihara, A Hicks, N Chintala, M Cundy, W R Lempert, I V Adamovich, and S Gogineni. Measurement of flow conductivity and density fluctuations in supersonic nonequilibrium magnetohydrodynamic flows. *AIAA journal*, 43(9):1923–1930, 2005.

[22] S H Zaidi, T Smith, S O Macheret, and R B Miles. Snowplow surface discharge in magnetic field for high speed boundary layer control. *AIAA paper*, 1006:9–12, 2006.

[23] S O Macheret. Physics of magnetically accelerated nonequilibrium surface discharges in high-speed flow. In *AIAA, Aerospace Sciences Meeting, 44 th, Reno, NV*, 2006.

[24] C S Kalra, M N Shneider, and R B Miles. Numerical study of boundary layer separation control using magnetogasdynamic plasma actuators. *Physics of Fluids*, 21:106101, 2009.

[25] C S Kalra, S H Zaidi, R B Miles, and S O Macheret. Shockwave-turbulent boundary layer interaction control using magnetically driven surface discharges. *Experiments in fluids*, 50(3):547–559, 2011.

[26] R L Burton. *Pulsed Plasma Thrusters*. John Wiley and Sons, Ltd, 2010.

[27] R G Jahn. Physics of electric propulsion. 1968.

[28] M H Frese. Mach2: A two-dimensional magnetohydrodynamic simulation code for complex experimental configurations. *Interim Report Mission Research Corp., Albuquerque, NM.*, 1, 1987.

[29] R E Peterkin Jr and M H Frese. Mach: A reference manual. *Air Force Research Laboratory, Phillips Research Site*, 10, 1998.

[30] P G Mikellides. An overview of the mhd code, mach. *AIAA Paper*, 5614:2007, 2007.

[31] P G Mikellides, P J Turchi, and N F Roderick. Applied-field magnetoplasmadynamic thrusters, part 1: Numerical simulations using the mach2 code. *Journal of Propulsion and Power*, 16(5):887–893, 2000.

[32] I G Mikellides, P G Mikellides, P J Turchi, and T M York. Design of a fusion propulsion system-part 2: Numerical simulation of magnetic-nozzle flows. *Journal of propulsion and power*, 18(1):152–158, 2002.

[33] J Cassibry, F Thio, T E Markusic, and S Wu. Numerical modeling of a pulsed electromagnetic plasma thruster experiment. *Journal of propulsion and power*, 22(3):628–636, 2006.

[34] J T Cassibry, Y Thio, and S Wu. Two-dimensional axisymmetric magnetohydrodynamic analysis of blow-by in a coaxial plasma accelerator. *Physics of plasmas*, 13:053101, 2006.

[35] J P Trelles, C Chazelas, A Vardelle, and J R Heberlein. Arc plasma torch modeling. *Journal of thermal spray technology*, 18(5-6):728–752, 2009.

[36] D Bernardi, V Colombo, G Coppa, and A D'angola. Simulation of the ignition transient in rf inductively-coupled plasma torches. *The European Physical Journal D-Atomic, Molecular, Optical and Plasma Physics*, 14(3):337–348, 2001.

[37] S Paik, P Huang, J Heberleinand, and E Pfender. Determination of the arc-root position in a dc plasma torch. *Plasma chemistry and plasma processing*, 13(3):379–397, 1993.

[38] J Trelles, E Pfender, and J Heberlein. Multiscale Finite Element Modeling of Arc Dynamics in a DC Plasma Torch. *Plasma Chem Plasma Process*, 26:557–575, 2006.

[39] A Lebouvier, C Delalondre, F Fresnet, V Boch, V Rohani, F Cauneau, and L Fulcheri. Three-dimensional unsteady mhd modeling of a low-current high-voltage nontransferred dc plasma torch operating with air. *Plasma Science, IEEE Transactions on*, 39(9):1889 –1899, sept. 2011.

[40] V E Lynch, B A Carreras, H R Hicks, J A Holmes, and L Garcia. Resistive mhd studies of high beta tokamak plasmas. *Computer Physics Communications*, 24(34):465 – 476, 1981.

[41] P Gautier, R Gruber, and F Troyon. Numerical study of the ideal-mhd stability limits in oblate spheromaks. *Nuclear Fusion*, 21(11):1399, 1981.

[42] S C Jardin, J L Johnson, J M Greene, and R C Grimm. Dynamical grid method for time-dependent simulations of axisymmetric instabilities in tokamaks. *Journal of Computational Physics*, 29(1):101–126, 1978.

[43] W Stepniewski. Mhd numerical modelling of the plasma focus phenomena. *Vacuum*, 76(1):51 – 55, 2004.

[44] M Zambra, D Kalise, J Fernandez, E Hernandez, D Pasten, and V Munoz. Current sheet thickness in the plasma focus snowplow model. *J. Plasma Fusion Res. SERIES*, 8, 2009.

[45] K Watanabe and T Sato. Global simulation of the solar wind-magnetosphere interaction:the importance of its numerical validity. *Journal of Geophysical Research*, 95(A1):75 – 88, 1990.

[46] J F Hawley and J H Krolik. Global mhd simulation of the inner accretion disk in a pseudo-newtonian potential. *The Astrophysical Journal*, 548(1):348, 2001.

[47] R Ouyed and R E Pudritz. Numerical simulations of astrophysical jets from keplerian disks. i. stationary models. *The Astrophysical Journal*, 482(2):712, 1997.

[48] G Toth, I V Sokolov, T I Gombosi, D R Chesney, C R Clauer, D L De Zeeuw, K C Hansen, K J Kane, W B Manchester, R C Oehmke, et al. Space weather modeling framework: A new tool for the space science community. *Journal of Geophysical Research: Space Physics (1978–2012)*, 110(A12), 2005.

[49] J V Shebalin, W H Matthaeus, and D Montgomery. *Anisotropy in MHD turbulence due to a mean magnetic field.* PhD thesis, Cambridge Univ Press, 1982.

[50] O Agullo, W Müller, B Knaepen, and D Carati. Large eddy simulation

of decaying magnetohydrodynamic turbulence with dynamic subgrid-modeling. *Physics of Plasmas*, 8:3502, 2001.

[51] W Müller and D Biskamp. Scaling properties of three-dimensional magnetohydrodynamic turbulence. *Physical Review Letters*, 84(3):475–478, 2000.

[52] S B Pope. *Turbulent flows*. Cambridge university press, 2000.

[53] D S Balsara. Total variation diminishing scheme for relativistic magnetohydrodynamics. *The Astrophysical Journal Supplement Series*, 132(1):83, 2001.

[54] J M Martí and E Müller. Numerical hydrodynamics in special relativity. *Living Rev. Relativity*, 6, 2003.

[55] M Anderson, E W Hirschmann, S L Liebling, and D Neilsen. Relativistic mhd with adaptive mesh refinement. *Classical and Quantum Gravity*, 23(22):6503, 2006.

[56] J M Stone, T A Gardiner, P Teuben, J F Hawley, and J B Simon. Athena: a new code for astrophysical mhd. *The Astrophysical Journal Supplement Series*, 178(1):137, 2008.

[57] Ian J P and James M S. Nonlinear evolution of the magnetothermal instability in two dimensions. *The Astrophysical Journal*, 633(1):334, 2005.

[58] H-M Damevin and K A Hoffmann. Numerical simulations of magnetic flow control in hypersonic chemically reacting flows. *Journal of Thermophysics and Heat Transfer*, 16(4):498 – 506, 2002.

[59] D V Gaitonde. Development of a solver for 3-d non-ideal magnetogasdynamics. *30th AIAA Plasmadynamics and Lasers Conference*, AIAA-99-3610, 1999.

[60] S S Komissarov. Multidimensional numerical scheme for resistive relativistic magnetohydrodynamics. *Monthly Notices of the Royal Astronomical Society*, 382(3):995–1004, 2007.

[61] M Dumbser and DS Balsara. High-order unstructured one-step pnpm schemes for the viscous and resistive mhd equations. *Computer Modeling in Engineering and Sciences (CMES)*, 54(3):301, 2009.

[62] C Palenzuela, L Lehner, O Reula, and L Rezzolla. Beyond ideal mhd: towards a more realistic modelling of relativistic astrophysical plasmas. *Monthly Notices of the Royal Astronomical Society*, 394(4):1727–1740, 2009.

[63] M Dumbser and O Zanotti. Very high order $p_n p_m$ schemes on unstructured meshes for the resistive relativistic mhd equations. *Journal of Computational Physics*, 228(18):6991–7006, 2009.

[64] O Khan, K Hoffmann, and J Dietiker. Computational aspects of high-speed flows with applied magnetic field. *Magnetics, IEEE Transactions on*, 42(3):389 – 397, march 2006.

[65] J Blazek. *Computational Fluid Dynamics: Principles and Applications*. Referex Engineering. Elsevier, 2001.

[66] O S Jones, U Shumlak, and D S Eberhardt. An implicit scheme for nonideal magnetohydrodynamics. *Journal of Computational Physics*, 130(2):231 – 242, 1997.

[67] D R Reynolds, R Samtaney, and C S Woodward. A fully implicit numerical method for single-fluid resistive magnetohydrodynamics. *Journal of Computational Physics*, 219(1):144 – 162, 2006.

[68] L Chacon, D A Knoll, and J M Finn. An implicit, nonlinear reduced resistive mhd solver. *Journal of Computational Physics*, 178(1):15 – 36, 2002.

[69] H Lutjens and J Luciani. Xtor-2f: A fully implicit newtonkrylov solver applied to nonlinear 3d extended mhd in tokamaks. *Journal of Computational Physics*, 229(21):8130 – 8143, 2010.

[70] M-S Liou and C J Steffen. A new flux splitting scheme. *Journal of computational physics*, 107(1):23–39, 1993.

[71] B Van Leer. *Flux-vector splitting for the Euler equation*. Springer, 1997.

[72] E F Toro. *Riemann solvers and numerical methods for fluid dynamics: a practical introduction*. Springer, 2009.

[73] R Keppens, M Nool, G Tóth, and J P Goedbloed. Adaptive mesh refinement for conservative systems: multi-dimensional efficiency evaluation. *Computer physics communications*, 153(3):317–339, 2003.

[74] P Janhunen. A positive conservative method for magnetohydrodynamics based on hll and roe methods. *Journal of Computational Physics*, 160(2):649–661, 2000.

[75] K F Gurski. An hllc-type approximate riemann solver for ideal magnetohydrodynamics. *SIAM Journal on Scientific Computing*, 25(6):2165–2187, 2004.

[76] T Miyoshi and K Kusano. A multi-state hll approximate riemann solver for ideal magnetohydrodynamics. *Journal of Computational Physics*, 208(1):315–344, 2005.

[77] D S Balsara. Total variation diminishing scheme for relativistic magnetohydrodynamics. *The Astrophysical Journal Supplement Series*, 132(1):83, 2001.

[78] D S Balsara and D Spicer. Maintaining pressure positivity in magnetohydrodynamic simulations. *Journal of Computational Physics*, 148(1):133–148, 1999.

[79] W Dai and P R Woodward. A simple finite difference scheme for multidimensional magnetohydrodynamical equations. *Journal of Computational Physics*, 142(2):331–369, 1998.

[80] K G Powell, P L Roe, T J Linde, T I Gombosi, and D L De Zeeuw. A solution-adaptive upwind scheme for ideal magnetohydrodynamics. *Journal of Computational Physics*, 154(2):284 – 309, 1999.

[81] A Dedner, F Kemm, D Kröner, C-D Munz, T Schnitzer, and M Wesenberg. Hyperbolic divergence cleaning for the mhd equations. *Journal of Computational Physics*, 175(2):645–673, 2002.

[82] D S Balsara. Second-order-accurate schemes for magnetohydrodynamics with divergence-free reconstruction. *The Astrophysical Journal Supplement Series*, 151(1):149, 2004.

[83] J U Brackbill and D C Barnes. The effect of nonzero del.b on the numerical solution of the magnetohydrodynamic equations. *Journal of Computational Physics*, 35(3):426 – 430, 1980.

[84] J B Bell, P Colella, and H M Glaz. A second-order projection method for the incompressible navier-stokes equations. *Journal of Computational Physics*, 85(2):257–283, 1989.

[85] D L Brown, R Cortez, and M L Minion. Accurate projection methods for the incompressible navier–stokes equations. *Journal of Computational Physics*, 168(2):464–499, 2001.

[86] G Jiang and C Wu. A high-order weno finite difference scheme for the equations of ideal magnetohydrodynamics. *Journal of Computational Physics*, 150(2):561–594, 1999.

[87] P Ganesan and G Palani. Finite difference analysis of unsteady natural convection mhd flow past an inclined plate with variable surface heat and mass flux. *International journal of heat and mass transfer*, 47(19):4449–4457, 2004.

[88] J I Ramos and N S Winowich. Finite difference and finite element methods for mhd channel flows. *International Journal for Numerical Methods in Fluids*, 11(6):907–934, 1990.

[89] S Satake, T Kunugi, K Takase, and Y Ose. Direct numerical simulation of turbulent channel flow under a uniform magnetic field for large-scale structures at high reynolds number. *Physics of Fluids*, 18:125106, 2006.

[90] H Kobayashi. Large eddy simulation of magnetohydrodynamic turbulent duct flows. *Physics of Fluids*, 20:015102, 2008.

[91] K Miki and S Menon. Localized dynamic subgrid closure for simulation of magnetohydrodynamic turbulence. *Physics of plasmas*, 15:072306, 2008.

[92] D Krasnov, O Zikanov, and T Boeck. Comparative study of finite difference approaches in simulation of magnetohydrodynamic turbulence at low magnetic reynolds number. *Computers & Fluids*, 50(1):46–59, 2011.

[93] C R Sovinec, A H Glasser, T A Gianakon, D C Barnes, R A Nebel, S E Kruger, D D Schnack, S J Plimpton, A Tarditi, and M S Chu. Nonlin-

ear magnetohydrodynamics simulation using high-order finite elements. *Journal of Computational Physics*, 195(1):355 – 386, 2004.

[94] N B Salah, A Soulaimani, and W G Habashi. A finite element method for magnetohydrodynamics. *Computer Methods in Applied Mechanics and Engineering*, 190(4344):5867 – 5892, 2001.

[95] T C Warburton and G E Karniadakis. A discontinuous galerkin method for the viscous mhd equations. *Journal of Computational Physics*, 152(2):608 – 641, 1999.

[96] P Yan, P Hui, W Zhu, and H Tan. An investigation of the pulsed plasma for deposition of thin film materials. *Surface and Coatings Technology*, 102(12):175 – 181, 1998.

[97] B Jayaraman and W Shyy. Modeling of dielectric barrier discharge-induced fluid dynamics and heat transfer. *Progress in Aerospace Sciences*, 44(3):139 – 191, 2008.

[98] D V Roupassov, A A Nikipelov, M M Nudnova, and A Y Starikovskii. Flow Separation Control by Plasma Actuator with Nanosecond Pulsed-Periodic Discharge. *AIAA Journal*, 47:168–185, January 2009.

[99] J Shin, V Narayanaswamy, L L Raja, and N T Clemens. Characterization of a Direct-Current Glow Discharge Plasma Actuator in Low-Pressure Supersonic Flow. *AIAA Journal*, 45:1596–1605, July 2007.

[100] H Sitaraman and L L Raja. Gas temperature effects in micrometre-scale dielectric barrier discharges. *Journal of Physics D: Applied Physics*, 44(26):265201, 2011.

[101] H Sitaraman and L L Raja. "simulation studies of rf excited micro-cavity discharges for micro-propulsion applications". *Journal of Physics D: Applied Physics*, 45(18):185201, 2012.

[102] H Sitaraman and L L Raja. "simulation of rf microdischarges for microthruster applications". *IEEE Transactions on Plasma Science*, 39(11):2930 –2931, 2011.

[103] K Etemadi and E Pfender. Impact of anode evaporation on the anode region of a high-intensity argon arc. *Plasma chemistry and plasma processing*, 5(2):175–182, 1985.

[104] J A Bittencourt. *Fundamentals of plasma physics*. Springer, 2004.

[105] E F Toro. *Riemann solvers and numerical methods for fluid dynamics: a practical introduction*. Springer, 1999.

[106] T J Barth. Analysis of implicit local linearization techniques for upwind and tvd algorithms. In *25th AIAA Aerospace Sciences Meeting*, volume 1, 1987.

[107] S Osher. Numerical solution of singular perturbation problems and hyperbolic systems of conservation laws. *North-Holland Mathematics Studies*, 47:179–204, 1981.

[108] C Bischof, P Khademi, A Mauer, and A Carle. Adifor 2.0: Automatic differentiation of fortran 77 programs. *Computational Science & Engineering, IEEE*, 3(3):18–32, 1996.

[109] Wolfram Research, Inc. Mathematica Edition: Version 7.0. 2010.

[110] D J Mavriplis. Unstructured grid techniques. *Annual Review of Fluid Mechanics*, 29(1):473–514, 1997.

[111] A Haselbacher and J Blazek. Accurate and efficient discretization of navier-stokes equations on mixed grids. *AIAA journal*, 38(11):2094–2102, 2000.

[112] Y Saad and M H Schultz. Gmres: A generalized minimal residual algorithm for solving nonsymmetric linear systems. *SIAM Journal on scientific and statistical computing*, 7(3):856–869, 1986.

[113] S Balay, W D Gropp, L C McInnes, and B F Smith. Efficient management of parallelism in object oriented numerical software libraries. In E. Arge, A. M. Bruaset, and H. P. Langtangen, editors, *Modern Software Tools in Scientific Computing*, pages 163–202. Birkhäuser Press, 1997.

[114] H Luo, J Baum, and R Lohner. A fast, matrix-free implicit method for compressible flows on unstructured grids. In Charles-Henri Bruneau, editor, *Sixteenth International Conference on Numerical Methods in Fluid Dynamics*, volume 515 of *Lecture Notes in Physics*, pages 73–78. Springer Berlin / Heidelberg, 1998. 10.1007/BFb0106564.

[115] H Luo, D Sharov, J D Baum, and R Lohner. Parallel unstructured grid GMRES+LU-SGS method for turbulent flows. *41st Aerospace Sciences Meeting and Exhibit, Reno, Nevada*, AIAA-2003-273, 2003.

[116] H Courtecuisse and J Allard. Parallel Dense Gauss-Seidel Algorithm on Many-Core Processors. *High Performace Computation Conference, IEEE*, 2009.

[117] W K Anderson. A grid generation and flow solution method for the euler equations on unstructured grids. *Journal of computational Physics*, 110(1):23–38, 1994.

[118] P C Jorgenson and R H Pletcher. An implicit numerical scheme for the simulation of internal viscous flow on unstructured grids. *Computers & fluids*, 25(5):447–466, 1996.

[119] T F Coleman and J J Moré. Estimation of sparse jacobian matrices and graph coloring blems. *SIAM Journal on Numerical Analysis*, 20(1):187–209, 1983.

[120] T Barth and D Jesperson. The design and application of upwind schemes on unstructured meshes. In *AIAA, Aerospace Sciences Meeting, 27 th, Reno, NV*, page 1989, 1989.

[121] Y Shen, G Zha, and M A Huerta. E-CUSP scheme for the equations of ideal magnetothydrodynamics with high order weno scheme. *Journal of Computational Physics*, 231(19):6233–6247, 2012.

[122] K Burm, WJ Goedheer, and DC Schram. The isentropic exponent in plasmas. *Physics of Plasmas*, 6:2622, 1999.

[123] G Karypis and Vipin Kumar. A Parallel Algorithm for Multilevel Graph Partitioning and Sparse Matrix Ordering. *10th Intl. Parallel Processing Symposium*, pages 314–319, 1996.

[124] G W Sutton and A Sherman. *Engineering magnetohydrodynamics*. McGraw-Hill Book Company,New York, 1965.

[125] J Marshall. Performance of a hydromagnetic plasma gun. *Physics of Fluids (US)*, 3, 1960.

[126] J W Mather. Investigation of the high-energy acceleration mode in the coaxial gun. *Physics of Fluids*, 7(11):S28–S34, 1964.

[127] D Y Cheng. Application of a deflagration plasma gun as a space propulsion thruster. *AIAA Journal*, 9(9), 1971.

[128] D Y Cheng. Plasma deflagration and properties of a coaxial plasma deflagration gun. *Nuclear Fusion*, 10, 1970.

[129] D M Woodall and L K Len. Observation of current sheath transition from snowplow to deflagration. *J. Applied Physics*, 57(3), 1985.

[130] F Poehlmann, N Gascon, and M A Cappelli. The deflagration-detonation transition in gas-fed pulsed plasma accelerators. *AIAA Joint Propulsion Conference*, AIAA-2007-5263, 2007.

[131] J D Powell and J H Batteh. Plasma dynamics of an arcdriven, electromagnetic, projectile accelerator. *Journal of Applied Physics*, 52(4):2717–2730, 1981.

[132] L Spitzer Jr and R Härm. Transport phenomena in a completely ionized gas. *Physical Review*, 89(5):977, 1953.

[133] F Poehlmann-Martins. *Investigation of a Plasma Deflagration Gun and Magnetohydrodynamic Rankine-hugoniot Model to Support a Unifying Theory for Electromagnetic Plasma Guns*. PhD thesis, Stanford University, 2010.

[134] C L Enloe, T E McLaughlin, R D Van Dyken, K D Kachner, E J Jumper, and T C Corke. Mechanisms and responses of a single dielectric barrier plasma actuator: plasma morphology. *AIAA journal*, 42(3):589–594, 2004.

[135] D F Opaits, G Neretti, A V Likhanskii, S Zaidi, M N Shneider, R B Miles, and S O Macheret. Experimental investigation of dbd plasma actuators driven by repetitive high voltage nanosecond pulses with dc or low-frequency sinusoidal bias. *AIAA paper*, 4532:2007, 2007.

[136] B Jayaraman, S Thakur, and W Shyy. Modeling of fluid dynamics and heat transfer induced by dielectric barrier plasma actuator. *Journal of heat transfer*, 129(4):517–525, 2007.

[137] G I Font and W L Morgan. Recent progress in dielectric barrier discharges for aerodynamic flow control. *Contributions to Plasma Physics*,

47(1-2):103–110, 2007.

[138] A R Hoskinson, N Hershkowitz, and D E Ashpis. Force measurements of single and double barrier dbd plasma actuators in quiescent air. *Journal of Physics D: Applied Physics*, 41(24):245209, 2008.

[139] M Nishihara, K Takashima, J W Rich, and I V Adamovich. Mach 5 bow shock control by a nanosecond pulse surface dielectric barrier discharge. *Physics of Fluids*, 23:066101, 2011.

[140] S Im, H Do, and M A Cappelli. Dielectric barrier discharge control of a turbulent boundary layer in a supersonic flow. *Applied Physics Letters*, 97(4):041503–041503, 2010.

[141] N J Bisek and J Poggie. Exploration of mhd flow control for a hypersonic blunt elliptic cone with an impregnated ablator. In *49th AIAA Aerospace Sciences Meeting including the New Horizons Forum and Aerospace Exposition*, 2011.

[142] M Samimy, I Adamovich, B Webb, J Kastner, J Hileman, S Keshav, and P Palm. Development and characterization of plasma actuators for high-speed jet control. *Experiments in Fluids*, 37(4):577–588, 2004.

[143] M Samimy, J H Kim, J Kastner, I Adamovich, and Y Utkin. Active control of high-speed and high-reynolds-number jets using plasma actuators. *Journal of Fluid Mechanics*, 578(1):305–30, 2007.

[144] J Kim, A Afshari, D J Bodony, and J B Freund. Les investigation of a mach 1.3 jet with and without plasma actuators. *AIAA Paper*, 290:2009, 2009.

[145] D Roupassov, A Nikipelov, M Nudnova, and A Starikovskii. Flow separation control by plasma actuator with nanosecond pulsed-periodic discharge. *AIAA journal*, 47(1):168–185, 2009.

[146] A Fridman, S Nester, L A Kennedy, A Saveliev, and O Mutaf-Yardimci. Gliding arc gas discharge. *Progress in Energy and Combustion Science*, 25(2):211–231, 1998.

[147] C S Kalra, A Gutsol, and A Fridman. Gliding arc discharges as a source of intermediate plasma for methane partial oxidation. *Plasma Science, IEEE Transactions on*, 33(1):32–41, 2005.

[148] T Deconinck. *Simulation studies of direct-current microdischarges for electric propulsion*. University of Texas, 2008.

[149] B Van Leer, W Lee, and P L Roe. Characteristic time-stepping or local preconditioning of the euler equations. In *10th Computational Fluid Dynamics Conference*, volume 1, pages 260–282, 1991.

[150] C Liu, X Zheng, and C H Sung. Preconditioned multigrid methods for unsteady incompressible flows. *Journal of Computational Physics*, 139(1):35–57, 1998.

[151] H Nishikawa, P L Roe, Y Suzuki, and B van Leer. A general theory of local preconditioning and its application to the 2d ideal mhd equations. In *16th AIAA Computational Fluid Dynamics Conference*, 2003.

[152] Petsc frequently asked questions. `http://www.mcs.anl.gov/petsc/documentation/faq.html`.

[153] S Mahadevan and L L Raja. Simulations of direct-current air surface plasma discharges in supersonic flow. *AIAA Paper 2009*, 1192, 2009.

[154] T Deconinck, S Mahadevan, and L L Raja. Computational simulation of coupled nonequilibrium discharge and compressible flow phenomena in a microplasma thruster. *Journal of Applied Physics*, 106(6), 2009.

[155] F Iza, G Kim, S Lee, J Lee, J Walsh, Y Zhang, and M Kong. Microplasmas: Sources, particle kinetics, and biomedical applications. *Plasma Processes and Polymers*, 5(4):322–344, 2008.

[156] J G Eden and S-J Park. "microcavity plasma devices and arrays: a new realm of plasma physics and photonic applications". *Plasma Physics and Controlled Fusion*, 47(12B):B83, 2005.

[157] Y P Raizer. *Gas Discharge Physics*. Springer, Berlin, 1991.

[158] R L Burton, J G Eden, S-J Park, J K Yoon, M de Chadenedes, and S Garrett et al. Initial development of the microcavity discharge thruster. In *Proceedings of 31st Int. Electric Propulsion Conf*, 2009.

[159] M De Chadenedes. Propulsion performance of a microcavity discharge device. Master's thesis, Dept. of Aerospace Engg.,University of Illinois Urbana-Champaign, Urbana, IL, 2011.

[160] R J LeVeque. *Numerical methods for conservation laws*. Birkhauser, 1992.

[161] A Jeffrey and T Taniuti. Non-linear wave propagation. *Mathematics in Science and Engineering, New York: Academic Press, 1964*, 1, 1964.

[162] P L Roe and D S Balsara. Notes on the eigensystem of magnetohydrodynamics. *SIAM Journal on Applied Mathematics*, 56(1):f57–67, 1996.

[163] S K Godunov. Symmetric form of the equations of magnetohydrodynamics. *Numerical Methods for Mechanics of Continuum Medium*, 1:26–34, 1972.

[164] G A Sod. A survey of several finite difference methods for systems of nonlinear hyperbolic conservation laws. *Journal of Computational Physics*, 27(1):1–31, 1978.